2012-06-17

Performance Characteristics of Lithium Coin Cells for Use in Wireless Sensing Systems

Yin Zhang
Brigham Young University - Provo

Performance Characteristics of Lithium Coin Cells for Use in Wireless Sensing Systems

Yin Zhang

A dissertation submitted to the faculty of
Brigham Young University
in partial fulfillment of the requirements for the degree of

Doctor of Philosophy

John N. Harb, Chair
Dean R. Wheeler
William G. Pitt
Randy S. Lewis
John Hedengren

Department of Chemical Engineering

Brigham Young University

June 2012

ABSTRACT

Performance Characteristics of Lithium Coin Cells for Use in Wireless Sensing Systems

Yin Zhang
Department of Chemical Engineering, BYU
Doctor of Philosophy

Understanding the pulsed discharge behavior of low-rate lithium coin cells in wireless sensing systems is critical to prolong the operating life and/or reduce the size of battery-powered WSs. This dissertation presents the battery transient analysis for a sensor duty cycle, experimental studies for sustained pulse discharge cycling, and investigation on recharge strategies for a battery/power harvesting hybrid system for WSs.

The transient behavior of the lithium coin cells during pulse discharge and subsequent relaxation was investigated with single-pulse experiments and theoretical analysis. The voltage response for a pulsed discharge had two parts: a region of rapid voltage change and a region of slower change. The magnitude of the rapid voltage losses was associated with ohmic and interfacial resistances. Solid phase diffusion in the cathode was found to be the major contributor to the "slow" transient voltage change that occurred during and after a pulse. An analytical model was developed to describe the time-dependent voltage and the corresponding non-uniform concentration distribution for the thick porous electrode. A fit of the analytical model to experimental data permitted an estimate of the solid phase diffusivity. Independent fitting of the pulse data and relaxation data both yielded a diffusivity of $D \sim 4\times10^{-11}$ cm^2/s, which agreed well with measured values reported in literature.

The interactive effect of battery characteristics and WS operating conditions was investigated during sustained pulsed-discharge cycling. At low standby currents ($\leq$50 μA), the influence of the standby current on the operating voltage and battery capacity was negligible. The pulse current had a significant impact on the lower voltage and determined the maximum capacity that could be extracted from a battery regardless of the duty cycle factor. For each pulse length studied, the battery capacity increased as the standby time increased, until a maximum capacity was reached, which could not be increased by further increase in the standby time. The minimum standby time for full (or near full) relaxation for duty cycles with different pulse length was found to correlate well with ratio t_s/t_p^2.

Battery pulse discharge-recharge cycling as would occur in a hybrid power system was investigated, and the recharge strategies were evaluated in terms of capacity loss over cycling and energy efficiency. Results from the cycling tests suggested the importance of a rest period between the discharge and charge step of a cycle. PRCR cycling with a 2 s rest period could lower the capacity loss to 25% or less of that of PC cycling with no rest period over 10,000 cycles. Cycling the battery at 80% SOC rather than at 100% SOC (3.1 V) significantly reduced the capacity loss during cycling.

Key words: lithium coin cell, pulsed discharge, wireless sensor, duty cycle, power supply

ACKNOWLEDGMENTS

I wish to express my gratitude to all those who gave me the possibility to complete this dissertation and supported me during my studies at Brigham Young University. I am deeply grateful to my PhD advisor, Dr. John N. Harb for giving me the opportunity to work with him in the field of batteries. I appreciate the freedom and the time he gave me to work on microbattery development, battery electrochemical analysis and nanostructured silicon electrode development. Without his support, completion of this work would not be possible. I am thankful to each of the professors serving on my dissertation committee for their time and suggestions. I would like to thank Dr. Dean R. Wheeler for the stimulating discussions, kind advice and encouragement. I would also like to thank Dr. William G. Pitt for his concern, encouragement and continuously checking on my progress during my dissertation writing. Dr. Richard L. Rowley, who served on my committee before his recent retirement, is sincerely acknowledged. Thanks are also due to Dr. Robert C. Davis and Dr. Richard R. Vanfleet for their support and guidance on the silicon anode research work.

I would like to thank my fellow students Jianfei Liu, Jun Song, Indrajeet Thorat, Vipul Mathur, David Stephenson, David Brough, Bryce Walker, Amy Balls for their company and support over the years. Special mention should go to Jianfei Liu for his help in taking SEM images. Thanks also to Kartikeya Murari and many others in the Neuroengineering group at Johns Hopkins University for their friendship and support on my microbattery work.

I would like to give my special thanks to my husband Jingang Li and my daughter Emma Li for their love, patience and undying confidence in me. My husband’s hard work, love and guidance have always taken me through hard times and enabled me to complete this dissertation

successfully. I thank my parents Dezhong Zhang and Yali Sun and my sister Hong Zhang for their unconditional support and encouragement to pursue my interests.

I would like to acknowledge support from NIH (MH062444 065296) and National Science Foundation (1027750).

TABLE OF CONTENTS

LIST OF TABLES

LIST OF FIGURES

LIST OF SYMBOLS

a	interfacial area per unit volume, cm^{-1}
A	cross-sectional area, cm^2
c	lithium concentration, mol cm^{-3}
C_{pul}, C_{tot}	capacity by pulses and total capacity, mAh
dV	voltage change, V
D	diffusion coefficient of lithium ion, cm^2 s^{-1}
$\mathcal{D}$	duty cycle factor
E	cell voltage
F	Faraday's constant, 96485 C mol^{-1}
i	current density, mA cm^{-2}
i_0	exchange current density, mA cm^{-2}
I	applied current, mA
I_p, I_s	pulse current and standby current, mA
I_{ave}	average current, mA
L	electrode thickness, mm
n	number of electrons transferred in electrode reaction
N	number of pulse discharge cycles
R	universal gas constant, 8.314 J mol^{-1} K^{-1}
R_p	particle radius, μm
R_{ct}	charge transfer resistance, Ω
S	cross-sectional area of cathode, cm^2
t	time, s
t_p, t_s	pulse length and standby time, s
T	temperature, K
V	voltage, V
V_m	molar volume, cm^3 mol^{-1}
U	open-circuit potential, V
y	lithium composition

Greek

α_a, α_c	transfer coefficients
ε	porosity
η_c, η_s	concentration and surface overpotential, V
θ_p	percentage of capacity delivered at peak current
κ	conductivity of electrolyte, S cm^{-1}
σ	electronic conductivity of solid, S cm^{-1}
τ	pulse length, s

1 INTRODUCTION

As portable electronic devices are becoming smaller, lighter and more sophisticated, the demand for superior portable energy continues to rise. The advances in battery technology, however, have not kept pace with innovations in microelectronics and wireless communication technologies. In order to bridge this gap, improvements in the energy efficiency of the devices themselves are required. For battery powered electronic systems, the battery life directly impacts the system's duration, functionality and mobility. Improving energy efficiency and prolonging battery life has become a primary consideration for system design.

Battery life is a function of not only the total power consumption, but also of the manner in which the system discharges the battery and the specific characteristics of the battery itself. Battery-driven or battery-aware system design, which aims at exploiting the interactive effect of battery characteristics and discharge conditions of the system, promises to provide further improvements in battery life beyond that achievable through low-power energy-efficient design alone.

Of particular interest to this study is wireless sensing systems, which rely on on-board power supplies throughout their lifetime. Individual sensor capabilities are constrained by the energy available to perform tasks. Because the desired small form factor for the system prohibits the use of large capacity batteries, battery life often limits the operating time of a wireless sensor (WS). In the case of wireless sensor networks (WSN), battery life directly affects the

configuration and function of the WSNs. Energy optimization needs to be considered at both the node level and the network level in order to maximize the lifetime of a wireless sensor network. Energy efficiency is of utmost priority in WS and WSN design.

Optimizing battery life through battery-aware design requires an understanding of both the energy source and the way the system uses it. Presently there is very little work that has investigated the battery behavior in the context of WSNs and, specifically, the interactive effect of battery characteristics and WS operation conditions. A more complete understanding of the influence of WS operating conditions on battery performance and lifetime is critical to our ability to maximize the energy that can be extracted from a given battery in order to prolong the operating life and/or reduce the size of battery-powered WSs.

1.1 Choice of power options

As advances in integrated circuit design are continually shrinking the size, power consumption and cost of the WS devices over the last decade, the ability to provide power to distributed WSs remains a challenge. Two power options that have been considered are batteries and energy harvesting (e.g. solar cells, piezoelectric and thermoelectric transducers). Battery power is a simple and convenient choice, and currently most wireless sensors require an on-board battery as the power supply. For some applications that need longer operating life, a hybrid power source that combines an energy harvesting device with a rechargeable battery are of great interest. In either situation, the power supplies of WSs need batteries that have a small size, long life, and sufficient pulse power capability.

The battery of choice must meet the power requirements of the WS system. The average power required for WSs is normally low, since many of them operate on an intermittent duty cycle in order to minimize the power consumption. Duty cycles commonly seen with WSNs

consist of very short (tens to hundreds of milliseconds) pulses of mA magnitude separated by much longer "standby" periods where little or no power is required. Figure 1.1 illustrates the current pulse profile and duty cycle characteristic of WSs. The parameters used to define a pulse discharge include peak current I_p, standby current I_s, pulse length t_p, standby period t_s. In a periodic event, duty cycle factor (or duty cycle) is the ratio of the duration of the pulse to the total period of a cycle, i.e. $\mathcal{D} = t_p/(t_s+t_p)$. For the battery/power harvesting hybrid power supplies, battery recharge may take place during the standby period between the discharge pulses.

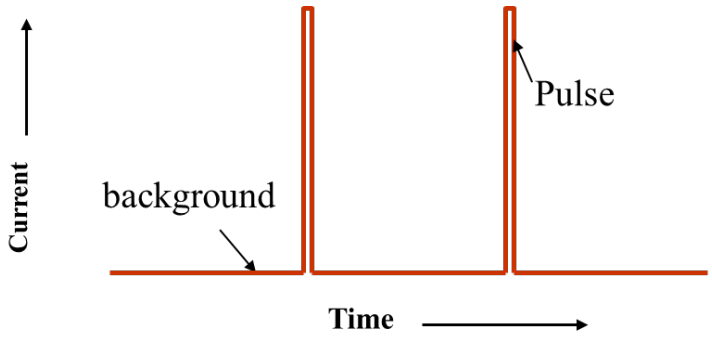

Figure 1.1 Illustration of current profile and duty cycle characteristic of WSs.

Lithium coin cells represent an attractive option for use in wireless sensors, due to their small size, high voltage and high energy density. The coin type cells, with a cathode layer thickness of a few hundred microns or higher, are designed to maximize energy density, and are most suitable for low-rate current drain applications such as memory backup. The average power of WSs (on the order of a few to hundreds of μW), resulting from the low duty cycles, can be easily met by lithium coin cells. However, the high power pulses must also be supplied in order to enable functions such as RF transmission and reception. The pulse power capability of the

lithium coin cells needs to be evaluated before they can be used effectively in power systems for WSs.

1.2 Experimental and theoretical analysis of pulsed discharge

As shown in Figure 1.1, the two key features of a WS power profile are 1) the large difference between the magnitude of the peak and standby currents, and 2) the large difference between the duration of the short bursts of current relative to the long standby period. In wireless sensors, the maximum or peak current (10-20 mA) is hundreds or even a thousand times greater than the standby current, unlike many other pulsed discharge modes for wireless communication, where the current ratio may only be 10:1. For coin cells that are designed for low standard current drain, the peak current of a WS operation is well beyond the limiting current of the battery (i.e., the sustainable current at which a substantial fraction of the battery capacity can be utilized). Under these conditions, the battery voltage varies with time and is highly sensitive to the magnitude and duration of the current pulse. The discharge capacity for the battery under a given duty cycle is defined as the value of the capacity at the point when the battery voltage drops below a specified lower limit (i.e. cutoff voltage). For a WS system, this limit will be reached during a discharge pulse, which is the portion of the duty cycle where the voltage is lowest. Thus, an understanding of the transient response of the battery during a discharge pulse is critical to accurate prediction of battery behavior and improvement of battery life for WSs.

During WS operation, the high current pulse length is often very short (e.g., a fraction of a second). Following the pulse discharge is a much longer low power standby period. When a battery is switched to a low current drain or stands idle after a high current pulse, certain electrochemical processes take place which cause a recovery of the battery voltage. Thus, the voltage of a battery, which dropped during high rate discharge, will rise (recover) during the

subsequent standby period. This “recovery effect” can result in a significant increase in battery life, especially when the peak current and the standby current differ significantly in magnitude, as in the case of WSs. The standby current and time have a great impact on the voltage recovery or relaxation process and the resulting capacity of the battery. Understanding the battery relaxation behavior and how the pulse/standby operation affects the battery life will allow us to determine the optimum operating conditions to effectively use small-sized low-rate cells in WSs.

Battery pulse discharge behavior depends on the physical characteristics of the battery itself such as battery chemistry, cell configuration and electrode design. The transient voltage during pulse discharge is associated with the various electrochemical processes taking place in the cell. Theoretical analysis combined with systematic experimental work is needed in order to understand the dominant physical processes and the limiting mechanisms that control the behavior of the battery. Specifically, electrochemical models and analysis that capture the battery characteristics most relevant to WS duty cycles, and which are more readily accessible to system engineers, are greatly needed in order to truly enable battery-aware system designs.

In this study, we focus on small-sized lithium coin cells that are of interest for use in both existing and future WS systems. This dissertation couples theoretical analysis with experimental investigation of the behavior of these cells during sensor duty cycles. In particular, we seek to evaluate, understand and describe how the pulse operation parameters affect: 1) the cell voltage during the discharge pulse and subsequent relaxation, and 2) the overall battery capacity and lifetime. As part of this effort we will investigate how battery behavior during pulse discharge is influenced by the physical properties of the battery (including thermodynamic and kinetic parameters, material properties such as conductivity and transport properties such as diffusivity), and by battery design parameters (such as electrode thickness, porosity and particle size). A key

objective of the work is to provide a quantitative basis for the selection of WS design parameters to maximize battery efficiency, and important guidelines for battery selection, optimization and/or design for use in WSs.

1.3 Outline

This dissertation is organized as follows.

Background. Chapter 2 summarizes possible power solutions for wireless sensors and provides a review of electrochemical principles relevant to batteries, with particular focus on lithium batteries. In particular, we emphasize performance limitations and tradeoffs related to the use of batteries in WSs that are brought about by energy constraints unique to wireless sensor networks.

Experimental apparatus and procedure. Chapter 3 describes the electrochemical and other characterization testing equipment and testing procedures used in this study.

Transient behavior during pulse discharge. Chapter 4 is focused on electrochemical analysis of the transient pulse discharge and the subsequent relaxation processes that take place in the battery in order to provide a basis for understanding and optimizing battery performance for sensing duty cycles. A quantitative mathematical description of the observed battery behavior is provided as part of this analysis.

Experimental study of pulse cycling. Chapter 5 shows experimental results of pulse cycling of lithium coin cells. The influence of pulse discharge conditions (I_p, I_s, t_p, t_s) and the average current on battery voltage and resulted capacity is evaluated. An analysis of voltage losses associated with the various pulse discharge conditions is also provided.

Experimental study on recharge strategies. Chapter 6 presents studies on battery pulse discharge-recharge cycling as would be used in a battery/power harvesting hybrid power system.

Different recharge strategies were evaluated in terms of capacity loss over cycling and the overall energy efficiency.

Conclusion. Chapter 7 provides the summary, conclusion and recommendations for future work.

2 BACKGROUND

Wireless sensing devices can be used to probe the environment, make computations, store data and communicate data, but all on a limited basis. Individual sensor capabilities are constrained by the energy available to perform tasks. The last decade has seen exponential technological improvements in sensing, computation and communication capabilities. However, advances in battery technology still lag behind, making the energy source the current bottleneck in wireless sensor networking. This chapter summarizes possible power solutions for wireless sensors (WS) and, in particular, performance limitations and tradeoffs related to the use of batteries in WSs that are brought about by energy constraints unique to wireless sensor networks (WSN). Section 2.1 provides a brief review of WS and WSN. Section 2.2 introduces the concept of battery-aware system design. In Section 2.3, a summary of currently available coin cells is presented. Section 2.4 provides a review of electrochemical principles of batteries, with particular focus on lithium batteries. Section 2.5 introduces the battery/power-harvesting hybrid strategies, battery recharge and battery self-discharge. Finally a summary of the chapter is presented in Section 2.6.

2.1 Wireless sensors and wireless sensor networks

Wireless sensors are small, autonomous devices that can sense and/or interact with the physical world with no physical connections for either power or communication [1, 2]. The

system architecture of a wireless sensor is shown in Figure 2.1. The wireless sensor is comprised of four subsystems: (1) a sensing unit that measures the physical parameters (e.g. temperature, pressure, light intensity, sound, magnetic field, concentration or pH, etc.) and translates the measurements to electrical signals, (2) a processing unit that manipulates and stores the data collected, with limited amount of computation, (3) a communication unit consisting of a short range radio for wireless communication, and (4) a power supply unit that houses the batteries (or other energy source) and power conditioning circuitry, and provides power for the entire wireless sensor.

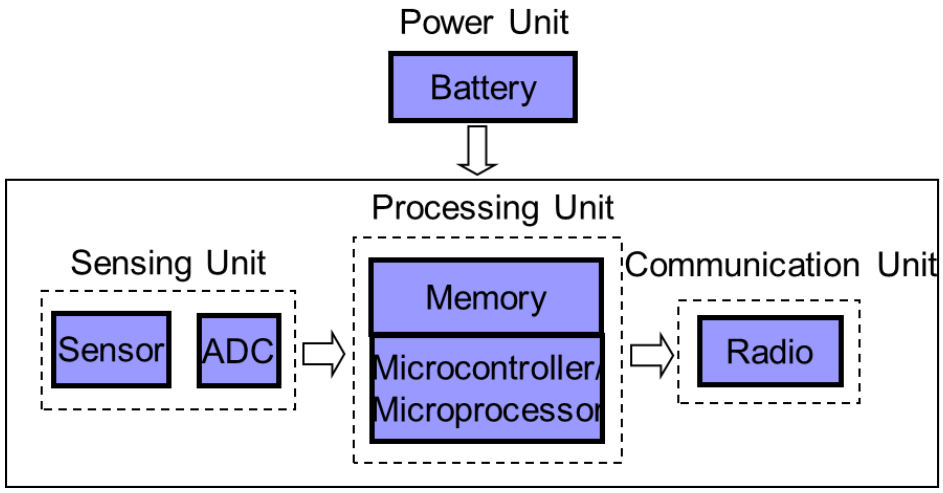

Figure 2.1 System architecture of a wireless sensor

Modern wireless networking technologies enable the coordination and networking of a large number of such sensor devices. A wireless sensor network consists of large number of spatially distributed autonomous sensor nodes working cooperatively, and passing data through the network to main base stations [3]. The base stations (or sinks) are the interface through which the WSN interacts with the digital world and internet. The more modern networks are bi-

directional, also enabling control of sensor activity. The potential applications of wireless sensor networks include military surveillance, environmental monitoring, and event detection (e.g. fire, earthquake) [4]. Some examples for civilian applications are smart sensors for manufacturing facilities and home electronics, and wearable sensors for medical or health applications [5, 6]. In this decade, Hewlett-Packard has embarked on a ten-year project (2010-2020), a "Central Nervous System for the Earth," to embed up to a trillion pushpin-size sensors around the globe, which could monitor weather, environment, traffic, road conditions and could "revolutionize human interaction with the earth"[7].

The sensor notes within a WSN are commonly referred to as "motes". The most widely used motes in recent years have included the Mica family (Mica2, MicaZ, etc.) [8] and its latest ultra-low power Telos [9], developed by the UC-Berkeley group, the uParts and Particles by Teco based in Germany [10], and the commercialized product Tmote Sky [11]. Figure 2.2 shows a Teco uPart [10], and a wearable medical sensor integrated with the Telos mote developed at Harvard University [5, 6]. The batteries used for both systems are also shown in the pictures. The size of a WS mote is determined to a great degree by the size of the system that powers it.

Understanding power consumption is especially critical for WSs based on limited energy reserves. Wireless sensors generally operate on an intermittent duty cycle in order to minimize power consumption. Under conditions where a continuous stream of information is not needed, the system is designed with a standby mode where components that are not in use are powered down, and a working mode where data collection, processing and transmission take place [3]. Duty cycles characteristic of WSNs consist of short pulses (tens to hundreds of milliseconds) of mA magnitude separated by much longer standby periods where little or no power is required. Figure 2.3 shows the measured current consumption for a Mica2 node [12]. It can be seen that

the current consumption varies significantly during standby and operation. While the low power standby mode consumes only tens of µA, the current consumption for the radio to receive and transmit messages is 10-25 mA.

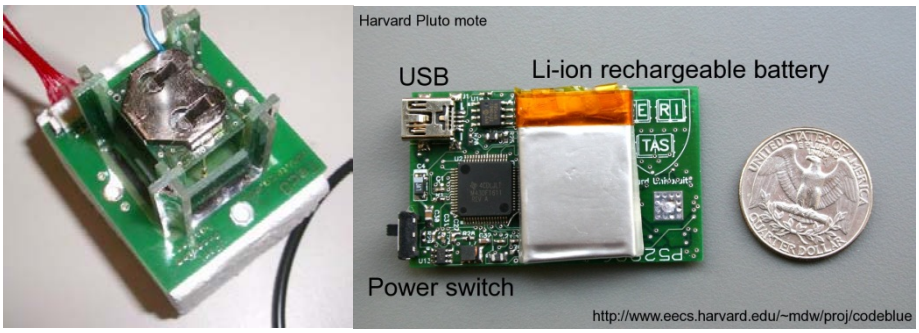

Figure 2.2 Examples of wireless sensors. Teco µPart powered by a primary lithium coin cell CR1620 (left); Harvard wearable Pluto mote powered by a pouch type rechargeable lithium ion battery (right).

Wireless communication is a major power consumer during system operation. The peak current of a WS depends largely on the radio transmission power level, which in turn affects the transmission distance [13]. The transmission time is directly dependent on the volume of data transmitted. For WS nodes that build from commercial-off-the-shelf (COTS) components, the power profile of the hardware selected has a great impact on the power consumption characteristic of the WS. For example, the Mica2 node uses a ChipCon CC1000 radio capable of transmitting at 38.4 Kbps with an outdoor transmission range of approximately 300 m, which supports transmission power levels ranging from -20 dBm to +10 dBm (corresponding to 4 mA to 22 mA) [8, 12]. The new record low power transceiver for wireless sensor released this year by Imec runs on a 4.5 mA from a 1.2 V supply (2.7 nJ/bit) at 0 dBm output, which could decrease the peak power consumption by 3 times relative to the current state-of-the-art radios for WSs [14].

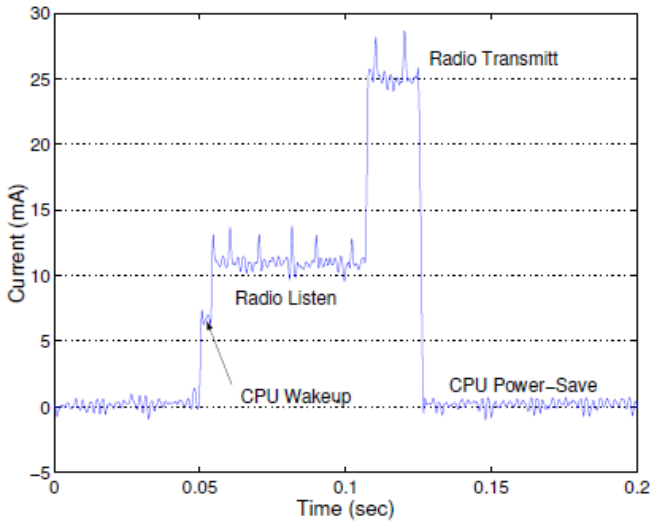

Figure 2.3 Measured current consumption for transmitting a single radio message at maximum transmit power on the Mica2 node [12].

While a simple approximation of overall power usage can be derived from estimates of node duty cycle and communication rates, the detailed power consumption profile and pattern of power loading is important to consider when selecting suitable cells and predicting battery life for WSs. For pulsed discharge operations in WSs, the battery life cannot be evaluated based just on the overall power usage. For example, the cell voltage will most likely drop below the cut-off voltage during a discharge pulse for data transmission, a fact that is not represented in an analysis based on average power consumption [15]. In a WSN deployment study, sensor nodes significantly underperformed relative to their expected lifetimes, and lessons were learned that "the periodic, constant power load presented to the batteries is ill suited to extract the maximum capacity" [16]. There is very little work that has investigated the battery behavior in the context of WSNs and, specifically, the interactive effect of battery characteristics and WS operation conditions. Understanding the influence of WS operating conditions on battery performance and lifetime is critical to enable energy-efficient, long-lived WSNs.

2.2 Battery-aware design

Prolonging the operating life of battery-powered WSs is a principal objective in the WS system and WSN design. Because the desired small form factor for the system prohibits the use of large capacity batteries, battery life often limits the operating time of a WS. The battery-driven nature is evident for applications where replacement of on-board batteries is cost prohibitive or even impossible once the sensors are deployed. For portable sensing devices powered by rechargeable batteries, it is also highly desirable for the system to last longer between charges. This has driven the research and development of numerous low-power or energy-efficient technologies that aim at minimizing energy consumption of WSs. However, battery capacity is a function of not only the total power consumption, but also of the manner in which the system discharges the battery and the specific characteristics of the battery itself [15, 17, 18]. Recently, there is growing interest in the "battery-aware" or "battery driven" system design, which by exploiting the battery characteristics in the system design, promises further improvements in battery life beyond that achievable through conventional low-power design alone [17, 19, 20].

Research showed that the operating conditions or duty cycle of WSs can greatly impact the amount of deliverable energy from a battery. Park et al. investigated the interactions between WSN parameters and battery characteristics using an experimental test-bed comprising MICA2 hardware [8], commercial lithium-coin batteries and a battery simulator Dualfoil [21]. They observed that use of a battery-aware approach for selection of transmission power levels led to a 52% increase in the amount of data that could be sensed and transmitted before the battery was exhausted, relative to an approach that assumed a finite, but ideal energy source of equivalent capacity [17]. In a more recent study, Chau el al. examined the gain of battery runtime due to

battery “recovery effect” on commercial sensors, and analyzed battery recovery in the presence of saturation threshold and random sensing activities. They proposed to exploit battery recovery effect to optimize the energy efficiency in the design of wireless sensor networks [22].

Maximizing battery life through battery-aware design requires incorporating battery state information into a system design strategy. Battery models are useful tools because they can be used to predict battery behavior under various design conditions. Several different battery models have been considered [19, 20]: 1) the empirical or analytical models, which capture the non-ideal discharge behavior with simple mathematical descriptions [18], 2) electrical circuit models, which construct a coupled circuit network to represent the battery [23], 3) stochastic models, where the battery is represented by a finite number of charge units, and the discharge behavior is modeled using a discrete time transient stochastic approach [15], 4) electrochemical models, which use partial differential equations to describe the physical, kinetic and thermodynamic processes in the batteries, and solve these equations along with the geometric parameters and boundary conditions to simulate the electrochemical performance of porous electrodes [21, 24].

There has been extensive research on electrochemical modeling of lithium batteries [24]. Using a combination of model and experiments, one can understand the limiting mechanism in batteries for a particular application. Electrochemical models of lithium batteries are closely tied to specific batteries, and at the same time require a large number of parameters. While they are capable of accurate and detailed predictions in the hands of electrochemists, they are hard to configure and tune, and provide limited analytical insight for system engineers. Relatively simple models and analysis that capture the battery characteristics most relevant to the battery-aware

design, and which are more readily accessible to system engineers, are greatly needed in order to truly enable battery-efficient system designs.

2.3 Coin type batteries

In spite of accelerated progress in WSs and WSNs over the last decade, the ability to provide power to distributed wireless sensors remains a challenge. Currently many wireless sensors rely on an on-board battery as the power source [6]. Lithium batteries represent an attractive option due to their high voltage and high energy density. Small-sized lithium batteries, either replaceable (primary) or rechargeable (secondary), are commercially available as coin type cells. The most common primary lithium coin cells on the market are MnO_2/Li (CR) and $(CF)_n$/Li (BR) cells [25]. BR series are most suitable for use at low to medium discharge rates and for applications that require extended reliability and safety over a broad temperature range (0-80°C). CR series have a narrower operating temperature range, but are more suitable for uses that require strong load pulse characteristics. The rechargeable lithium coin cells include MnO_2/LiAl (ML) and V_2O_5/LiAl (VL) cells [26]. The ML series have a higher energy density than the VL series, while the latter is ideal for applications where voltage stability is more important than capacity.

Other coin cell chemistries commonly used today are AgO_2/Zn (SR), MnO_2/Zn (LR) and Air(O_2)/Zn (PR) [27]. The silver oxide coin cells have very stable output voltage until the sudden drops that occurs at end of life. The alkaline coin cells are the least costly among all these options, while the costs of the other four chemistries, including the two lithium ones, are comparable [28]. Table 1.1 lists the different types of primary coin cells and their electrochemical characteristics. The energy density was calculated based on the dimensions and weight of the commercial products from each type of chemistry that offer a capacity around

120 mAh. The nominal voltage of these cells was used for the energy calculation. We can see that the highest energy density comes from the Zn/Air cells, which almost double the energy density of the lithium coin cells.

Table 2.1 Overview of commercially available primary coin type cells

Letter code	Cathode	Anode	Electrolyte	Nominal voltage (V)	Energy density	
					J/g	J/cm^3
LR	MnO_2	Zn	Alkali	1.5	280	1000
SR	AgO_2	Zn	Alkali	1.55	350	1500
PR	Air(O_2)	Zn	Alkali	1.4	1400	4000
CR	MnO_2	Li	Organic	3.0	840	2400
BR	$(CF)_n$	Li	Organic	3.0	860	2000

Cell selection for wireless sensors requires a balance of energy and size, and energy does not necessarily vary linearly with size, especially when small-sized coin cells are considered. It is well recognized that the energy density of batteries decreases gradually with reduced size due to the increasing amount of passive packaging material in proportion to active material in small batteries [29]. Table 1.2 shows a few examples of different sizes of coin cells and their energy densities. It is clear that the energy density of these coin cells decreases significantly when the battery size decreases. The rechargeable lithium coin cells (ML and VL) have much lower energy density than the two primary batteries (PR and CR) because of the active material and the electrode design used in these cells to provide good cyclability.

The coin type cells, with cathode layer thickness being a few hundred microns or higher, are sometimes referred as “energy” cells as opposed to “power” cells, which are designed with much thinner electrodes for high-rate applications. They are most suitable for low-rate current drain applications such as memory backup. The average power required for wireless sensors is

frequently low, since many of them operate on an intermittent duty cycle in order to minimize the power consumption [8-11]. The average power of a WS (on the order of a few to hundreds of μW) can be easily met by small coin cells. However, the high power pulses must also be supplied in order to enable functions such as RF transmission and reception. The pulse power capability of the coin cells must be evaluated before they can be used more effectively in power systems for WSs.

Table 2.2 Comparison of size and energy characteristics of different coin cells

Cell model	Capacity (mAh)	Diameter (mm)	Height (mm)	Weight (g)	Volume (cm^3)	Energy density	
						J/g	J/cm^3
PR521	33	5.8	2.15	0.2	0.057	830	2900
PR1662	1100	16	6.2	3.7	1.2	1500	4400
CR1025	30	10	2.5	0.7	0.2	460	1700
CR2477	1000	24.5	7.7	10.5	3.6	1000	3000
ML414	1.2	4.8	1.4	0.08	0.025	160	510
ML1220	17	12.5	2	0.8	0.25	230	750
VL621	1.5	6.8	2.1	0.3	0.076	50	210
VL1220	7	12.5	2	0.8	0.25	90	310

In this study, we consider rechargeable lithium coin cells that are able to meet the power requirements of existing and future WSs, which can potentially be used in battery/power harvesting power supplies. ML cells were chosen because of their higher energy density compared to VL cells. ML1220 cells were used for most of the tests of this work because they are the smallest cells capable of providing the 10-20 mA pulse current needed for WSs. The testing procedures, analysis and tools developed in this work can be used for VL series and other energy type lithium cells.

2.4 Electrochemical characteristics of batteries

2.4.1 Components and assembly of lithium coin cells

A battery is a device that converts the chemical energy contained in its active materials directly into electric energy by means of an electrochemical oxidation-reduction (redox) reaction. A cell consists of three major components, cathode, anode, and electrolyte [18]. Figure 2.4 shows a cross sectional view of a lithium coin cell [30]. In this example, the cathode is a porous composite electrode containing manganese oxide material. The anode is lithium metal on a stainless steel current collector mesh. The anode and cathode are separated by a polymeric sheet (separator). Liquid solution electrolyte that consists of lithium salts dissolved in organic solvents fills the pores of the electrode and separator.

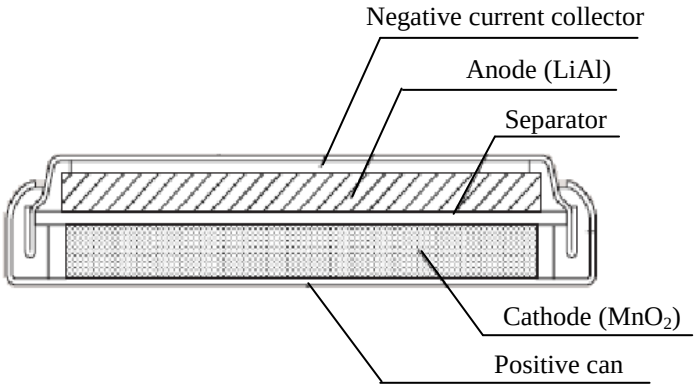

Figure 2.4 Schematic of lithium coin cell construction

2.4.2 Operation principles of lithium batteries

In a lithium battery, lithium ions move between the two electrodes. During discharge, lithium ions de-intercalate from the crystal structure of the anode, and intercalate into the crystal structure of the cathode. The lithium ions flow through the electrolyte whereas the electrons

generated from the negative electrode go through the external circuit to do work [31]. By convention the cathode and anode are labeled by the redox processes that happen during discharge.

The physical and chemical processes in a lithium battery can be further explained by considering an example with MnO_2 as the active material in the cathode. The reaction in the cathode can be represented by:

$$Mn^{IV}O_2 + xLi^+ + xe^- \underset{\text{Charge}}{\overset{\text{Discharge}}{\rightleftharpoons}} Li_xMn^{III}O_2 \qquad (2.1)$$

During the discharge process, the electrons from the external circuit flow through the current collector and the solid conductive network of the cathode, and reach the surface of the active material (MnO_2). Li^+ also reaches the surface of the active material by moving through the electrolyte between the two electrodes. At the surface of the active material, the lithium intercalation (forward) reaction occurs and then the lithium diffuses into the active material from the reaction sites on the surface.

Accompanying the electrochemical reactions, voltage losses occur inside the battery, which reduce the measured or output voltage of a cell. Those losses include: 1) activation or kinetic polarization, which drives the reaction at the electrode surface, 2) ohmic polarization, which is caused by the ohmic resistance (or sometimes referred as IR internal resistance) of the cell, and 3) concentration polarization, which arises from the concentration differences of the reactants and products at the electrode surface and in the bulk as a result of mass transfer.

The kinetic overpotential η_s and the reaction rate can be related by the Butler-Volmer equation [31]:

$$i = i_0[\exp(\frac{\alpha_a F}{RT}\eta_s) - \exp(-\frac{\alpha_c F}{RT}\eta_s)] \quad (2.2)$$

where i_0 is the exchange current density, analogous to the rate constant used in chemical kinetics. α_a and α_c are the apparent transfer coefficients, normally both taken to be 0.5 for lithium batteries. F is Faraday's constant, R is the ideal gas constant and T is temperature (Kelvin). In some cases where the current density or the overpotential is small, the Butler-Volmer expression can be simplified as a linear equation

$$i = i_0 \frac{(\alpha_a + \alpha_c)F}{RT}\eta_s \quad (2.3)$$

The linear expression is common in modeling low current density processes in porous electrodes. It has the advantage that it can be solved explicitly for the overpotential.

The IR resistance of a cell is the sum of the ionic and electronic resistances, including the ionic resistance of the electrolyte (within the separator and the porous electrodes), the electronic resistances of the composite electrode layers, the current collectors, tabs and metal covers, and the contact resistance between the active mass and the current collector. These resistances are ohmic in nature, yielding a linear relationship between current and voltage drop.

Concentration overpotential is associated with mass transport limitations. Mass transfer in an electrochemical system requires a description of the movement of ionic species, material balances, current flow, electroneutrality, and fluid mechanics [31]. Mass transport to or from an electrode surface can occur by essentially three processes: 1) convection, 2) migration in an electric field, and 3) diffusion. Convection can be neglected for both solid and liquid phases in lithium batteries. In many cases, migration in the solid material can also be negligible [24]. Migration in the liquid phase can be described mathematically with the use of the transference number, which represents the fraction of current carried by a specific ion due to migration (in the

absence of concentration gradient) [31]. Diffusion is a most important process in a battery system, which can be described by Fick's second law:

$$\frac{\partial c}{\partial t} = D\frac{\partial^2 c}{\partial x^2} \tag{2.4}$$

In the electrolyte phase, the Fick's law can be used for the ionic species (c_+ or c_-) or the electrolyte (c_l), with the corresponding diffusivities (D_+, D_- or D_l). The concentration overpotential η_c caused by the concentration difference existing between the electrode surface ($c_{l,E}$) and the bulk of the electrolyte ($c_{l,B}$) can be expressed as [18]

$$\eta_c = \frac{RT}{nF}\ln\frac{c_{l,B}}{c_{l,E}} \tag{2.5}$$

In the solid phase, the active material of the insertion electrodes consists of mobile cations (i.e. Li^+), mobile electrons and immobile host matrix. Equation (2.4) in spherical coordinate is normally used to describe the transport of lithium ions in the active particles (c_s) which can be modeled as spheres. The potential of the solid material is a function of state-of-charge (or lithium concentration) for the insertion electrodes of lithium batteries. The potential vs. composition (i.e. coulometric titration curve) is characteristic of the specific insertion material, and can be obtained by charging/discharge a cell at a sufficiently small current.

2.4.3 Time constants of physical phenomena

The time-dependent behavior of a lithium battery is influenced by the various physical processes in the battery, the characteristic times of which vary over a wide range. Figure 2.5 illustrates the typical time ranges of importance for several different battery processes [32]. As described by Jossen [32], the response of the battery to an electric field takes place very rapidly (~microseconds), and thus the ohmic overpotential can be observed almost instantaneously. At

the electrode-electrolyte interface, double layer charging occurs in parallel to the electrochemical charge transfer reaction [33]. The electric double layer is the result of charge separation in a thin region (on the order of 1nm) immediately adjacent to the electrode surface. The current that flows through the battery is divided at the interface into faradaic current, which contributes to the charge transfer reaction, and non-faradaic current that is used for double layer charging. As the double layer capacitance is very limited, the characteristic time for double layer charging is generally on the millisecond scale; after this short time, all of the current flows through the charge transfer reaction. Ong and Newman demonstrated that double layer effects occur within a few milliseconds in lithium-ion batteries, and thus can be neglected for current pulses with frequencies less than 100 Hz [56].

Unlike the Ohmic and double layer effects, mass transfer is a much slower process with a time scale of seconds to hours. The characteristic time is defined as R^2/D_s for diffusion in a spherical particle, where R is the radius of the particle and D_s is the diffusion coefficient of the material, and L^2/D_l for diffusion in the electrolyte, where L is length scale of interest and D_l is the electrolyte diffusion coefficient. Next to the mass transfer effects are long term effects such as cycling and aging, which are not considered in this study.

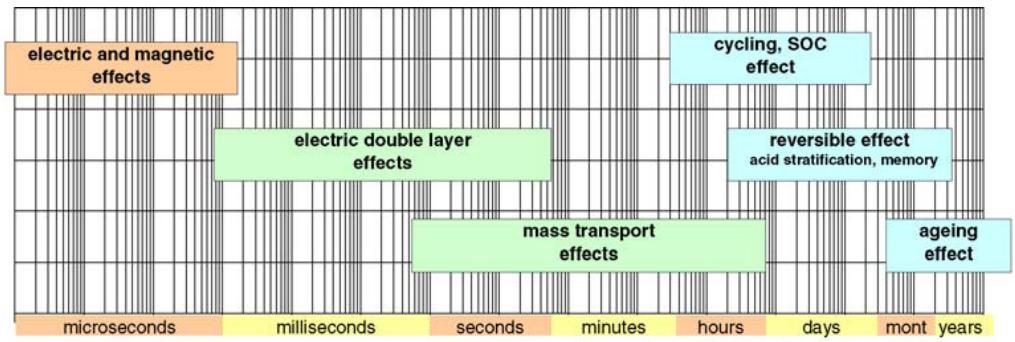

Figure 2.5 Typical time constants of different dynamic effects of batteries [32] (used with permission)

2.4.4 Battery pulse and relaxation behavior

The maximum or theoretical capacity of a battery is determined by the chemical energy stored in the active materials in the electrodes. It would be desirable to assess all of this capacity during discharge. However, losses due to polarization occur when a current passes through the electrodes. The polarization effects become more severe as the current increases. Therefore, if the cutoff voltage remains the same, less capacity can be accessed at a higher current rate since voltage losses are greater and the cutoff voltage is reached sooner, limiting discharge capacity. In particular, at current rates where the mass transfer fails to keep up with the reaction rate, the active species accumulate or are depleted at the electrode surface, cause the cell voltage to drop prematurely below the specified cutoff voltage. This phenomenon is often referred to as the rate capacity effect [18, 34].

When a discharge current is interrupted (e.g. the battery is switched to a low current drain or stands idle), the overpotentials caused by that current are relaxed and concentration gradients are reduced. The battery reaches a new open circuit potential or quasi-steady state depending on the relaxation condition. There are several phenomena associated with the relaxation of the cells, typically with varying time constants [35]: relaxation of ohmic and kinetic overpotentials, relaxation of the double layer capacitance, local equalization of the state of charge, and reduction of concentration gradients in the solid material and in the electrolyte. This “recovery effect” can result in an increase in battery life for repeated pulse discharges, which increases the feasibility of using small-sized low-rate cells in WSs. Particularly, significant improvements in battery capacity may be possible by exploiting the recovery mechanism in lithium batteries through battery-aware system design and selection of the pulse discharge parameters.

Pulsed battery discharge has received increasing attention in recent years. Most studies, however, are focused on pulses that would be encountered in hybrid electric vehicle (HEV) operation, which are a high rate discharge of tens of seconds followed by a rest period of seconds to minutes. For example, the hybrid pulse power characterization (HPPC) test procedure [57] consists of a discharge pulse for 18 s followed by open-circuit relaxation for 32 s. Smith and Wang developed a 1D model to include transient solid phase diffusion and used it to describe constant and HPPC data [58]. Bernardi and Go analyzed the pulse (40 s) and relaxation (5 mins) behavior of a lithium ion battery designed for HEV with a more detailed mathematical model, and identified the contributions of different electrochemical processes to the cell voltage [59]. Earlier work of Fuller et al. studied the transient phenomena of relaxation interspersed between discharge and charge cycles of much longer duration (~hours). They found that the voltage relaxation was influenced very little by concentration gradients in the electrolyte, whereas equalization of local state of charge across the electrode was the primary driving force for redistribution of material [60]. To our knowledge, so far there has been no electrochemical analysis that dealt with battery pulse discharge characteristics of WSs.

2.4.5 Battery materials

The CR and ML lithium coin cells chosen for this study use manganese oxide based material as the cathode. Li/MnO_2 was one of the first lithium/solid cathode systems to be used commercially and is now the most widely used primary lithium battery [18]. Early work on Li/MnO_2 was unsuccessful due to gas generation caused by a high moisture content. Sanyo employed the anhydrous heat-treated manganese dioxide (known as HEMD), and succeeded in commercializing Li/MnO_2 primary cells in 1976 [36]. Detailed investigation showed that HEMD was mainly a disordered pyrolusite material formed by rearrangement of the ramsdellite MnO_2 in

the ramsdellite/pyrolusite intergrowth of the parent γ-manganese dioxide [37]. On discharge, pyrolusite is lithiated in an irreversible process followed by insertion of additional lithium in a reversible process [38].

In the 1980's, Ikeda et al. investigated the cycle performance γ/β MnO_2. It was found that expansion of the crystal lattice occurs when lithium ions are inserted into its structure. However, the degree of expansion does not increase much after a large initial change at a quite low depth of discharge. Considering that, they developed a lithium-containing manganese dioxide (named composite dimensional manganese oxide, CDMO), which had some amount of lithium in its crystal structure before cycling, and greatly improved the rechargeability [39, 40]. The initial material consists of a mixture of MnO_2 and LiOH, which undergoes a heat treatment to yield CDMO.

$$yMnO_2 + z\ LiOH \longrightarrow (y-z/2)MnO_2 + z/2\ Li_2MnO_3 + z/2\ H_2O \qquad (2.6)$$

$LiAl/MnO_2$ secondary batteries were commercialized in the 1990's initially by Sanyo [41]. The commercial $LiAl/MnO_2$ secondary ML coin cells use LiAl alloy with Mn additives as the anode to enhance the cycling performance. A lithium salt in a 3-ingredient solvent (ethylene carbonate, butylene carbonate and DME) is used as electrolyte [42]. The cycle life of the battery is a strong function of depth of discharge (DOD). For example the ML cells can withstand 20,000 cycles, 3,000 cycles and 500 cycles under discharge conditions of 1%, 5% and 20% DOD respectively [43]. Currently the smallest rechargeable batteries on the market are Panasonic ML414 cells. These cells are 4.8 mm in diameter and 1.4 mm in thickness, having a rated capacity of 1.2 mAh and an overall weight of 0.08 g. The largest of ML cells are Sanyo ML2430, with 24.5 mm in diameter and 3mm in height, and 100 mAh total capacity [26].

2.5 Battery/power harvesting hybrid power strategy

2.5.1 Hybrid power supplies

Although duty cycling helps to extend wireless sensor operating lifetime, it does not remove the energy constraint placed by the battery. As WSs continue to shrink and incorporate more functions, they impose increasingly stringent energy requirements on a system. For distributed wireless sensors that need a longer operating life, a hybrid power source that combines an energy harvesting device with a rechargeable battery is of great interest [44, 45].

Power harvesting uses the external environment as a source of energy (e.g., light, vibration, temperature differences etc.). The energy conversion devices (e.g. solar cells, piezoelectric generators, thermoelectric generators) can provide a certain level of power, depending on the availability of energy. Research shows that it is reasonable to expect from tens of μW to a few mW of power to be harvested from ambient energy [45]. The fact that the harvested power may be irregular and discontinuous, and that power from the ambient sources is insufficient for the peak power, requires WSs to retain local energy storage to buffer the energy flow.

In a "battery/power harvesting" hybrid system, the battery provides power when peak power is needed or when energy harvesting is not available. When the energy harvesting device is operating, it supplies the standby power to the sensor system and charges the battery. Because standby periods are much longer than the discharge pulses, the energy harvesting device can operate at much lower power levels. The peak power is almost always provided by the battery, because the energy conversion devices either lack the ability to adjust to transient loads [46], or it is impractical to size them to meet the peak power requirement [44]. Coupling energy harvesting techniques with rechargeable batteries can theoretically extend the WS lifetimes

indefinitely (in practice, the lifetime will be limited by the cycle life of the battery). A well designed hybrid system has the potential to reduce the overall size of a power supply by allowing smaller batteries than would be required in a non-renewable system [44].

A hybrid power system needs rechargeable batteries that are small in size, have a long cycle life and possess sufficient pulse power capability [47, 48]. The rechargeable lithium coin cells available in the market are manganese oxide (ML) and vanadium oxide (VL) cells as shown in Table 1.2. Prakash et al. evaluated the self-discharge and polarization losses of various sizes of ML and VL cells for use in battery/fuel cell hybrid power supplies [46]. The self-discharge was evaluated as a function of cell potential and cell area. The polarization losses were expressed in terms of discharge efficiency, which is defined as the ratio of the average discharge voltage and average charge voltage.

Cook and Sastry considered a broad range of commercial cells of various sizes and chemistries, both primary and rechargeable, and developed an algorithm for cell selection (single cell or hybrid power bundles of cells) for wireless microsystems [61, 62]. Using this power optimization code and the battery data base, they identified power solutions under specified constraints (e.g. power, volume) and compared the results in terms of factors important to microsystems such as weight, size, operating life, etc. However, their method of predicting battery life was to assume that all cycles occur continuously; the battery recovery effect was not taken into account in their work. They recognized that these assumptions could result in significant overestimates of battery lifetime, but left resolution of this issue to future work.

2.5.2 Battery charging strategy

An appropriate battery charging strategy is critical for extending operational lifetime as well as providing performance stability for WSs. Since a hybrid system extracts energy from the

environment, recharge of the battery depends on the availability of energy. The operation of the energy harvesting devices may be 1) intermittent, which means recharge of the battery is only available for certain periods of time or 2) continuous, in which case the battery can be charged after every pulse during the standby period following the discharge. Battery charging can be subject to wide variations in energy availability and wide variations in power levels. Special control electronics are needed to protect the battery from overcharge.

Many different charging and termination schemes have been developed for different chemistries and different applications. The most common charging methods include constant current or constant voltage charging, pulse current charging [49, 50] and intelligent charging with special battery management control [51]. The charging termination can be controlled by current or voltage level, charging time or voltage change dV/dt. The conventional charging strategy for lithium batteries includes a constant current charging and constant voltage taper charging: first the battery is charged at a constant current until the potential reaches an upper voltage limit, then a constant voltage charging is applied until the current reduces to a pre-determined small value.

Lithium batteries often suffer from energy losses during cycling, which result in a less than 100% charge efficiency [52-54]. Battery charge efficiency is the ratio (expressed as a percentage) between the amount of charge removed from a battery during discharge and the amount of charge used during charging to restore the original capacity. It is also called the coulombic efficiency or charge acceptance. Charge efficiency and charge time can be influenced considerably by temperature, battery state of charge and charging strategy [18, 55]. The energy losses during pulse cycling may eventually lead to battery performance degradation if it is not

properly compensated during charging. It is imperative to evaluate the charging strategies to find the most energy efficient charge conditions for hybrid power systems for WSs.

2.6 Summary

In the near future, the physical world will be seamlessly connected to the online world through wireless sensors and devices. Lithium coin batteries represent an attractive option for use in wireless sensors, due to their small size, high voltage and high energy density. Presently there is a lack of experimental data that evaluates the performance characteristics of actual coin cells in WSs. Prolonging the operating life of battery-powered WSs is a principal objective in the WS system design. Maximizing battery life through battery-aware design requires an understanding of both the electrochemistry dependent battery characteristics and the way the system uses the battery.

Battery electrochemical analysis requires an understanding of the basic principles and physical processes that control battery performance. Battery modeling and analysis that capture the battery characteristics most relevant to the battery-aware design are needed in order to truly enable battery-efficient system designs. Such theoretical modeling and analyses, as well as assessment of the experimental behavior of lithium cells under sensor duty cycles will be provided in the next few chapters of this dissertation. The purpose of this work is to investigate the performance of rechargeable lithium coin cells under WS discharge and charge conditions and how the battery behavior during pulse discharge is influenced by the battery characteristics, to provide understanding and practical guidelines to optimize battery lifetime and find the most energy efficient operating conditions for WSs.

3 EXPERIMENTAL APPARATUS AND PROCEDURE

This chapter describes the electrochemical and other characterization testing equipment and testing procedures used in this study.

3.1 Commercial coin cells

A variety of coin cells were tested for initial cell evaluation and screening. A picture of these cells is shown in Figure 3.1. The battery size and chemical properties can be found in Section 2.3 of the background chapter. With the exception of the zinc-air (PR521) batteries, which were from Energizer, the other three types of cells used in this study including the ML1220, are from one single manufacturer, Panasonic. It is worth mentioning that international standards [18] are followed for the letter and numerical designations of these coin cells, and that the nomenclature is well recognized across battery manufacturers.

This dissertation is mainly focused on the use of ML1220 cells. The exact battery size, including the case, can be found from the manufacturer's data sheet. To measure the size and other properties of the cathode and anode inside these cells, a battery was carefully dissembled and the electrodes were removed from the case. The diameter and thickness of the electrodes were measured with an electronic digital micrometer (Chicago Brand Industrial Inc., Fremont, CA). The mass of the electrodes was measured by an electronic balance (Sartorius, GMBH, Gottingen, Germany). SEM pictures were taken of the ML1220 cathode in order to estimate the

active particle size and the porosity of the electrode. A four line probe (lab-designed) was used to measure the conductivity of the cathode layer.

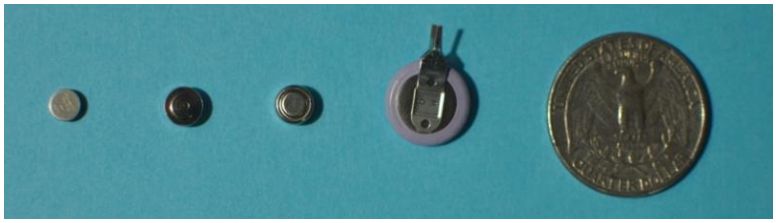

Figure 3.1 Commercial coin cells. (1) ML414 (rechargeable), (2) PR521 (primary), (3) SR527 (primary), and (4) ML1220 (rechargeable) with a quarter dollar (USA).

3.2 Electrochemical cycling

3.2.1 Testing equipment

Battery pulse cycling tests were conducted using a Maccor 4300 16-channel battery testing system (Maccor Inc.). The Maccor battery tester at BYU is configured with four-current range channels, which have a current control range of -150 to +150 µA, -5 to +5 mA, -150 to +150 mA, and -5 to +5 A. The available voltage range for each channel is 0 V to +5 V. The accuracy for current and voltage on these channels is ± 0.02% Full Scale Range (FSR).

The Maccor battery tester is operated by Maccor standard test software, which conforms to normal methods of operation for a Microsoft Windows based program. In the standard test mode, the minimum time step is 10 ms. Maccor battery tester also comes with a different pulsing mode to generate constant current pulses from 1 s down to 100 µs. A time step smaller than 10ms would have required special factory modification of the system configuration and settings.

An Arbin BT2000 8-channel battery tester was used for some of the pulse-relaxation tests. The Arbin battery tester is configured with three-current range channels, which have a current control range of -200 to +200 μA, -10 to +10 mA, and -0.5 to +0.5 A. The available voltage range for each channel is 0 V to +5 V. The accuracy for current and voltage on these channels is ± 0.02% FSR. The Arbin battery tester is controlled by Mits-Pro software, and the minimum time step is 15 ms.

3.2.2 Testing procedures

In the testing procedures, "C-rate" is sometimes used to define the current. It is a commonly adopted way to normalize currents for cells of different capacities. 1 C-rate corresponds to a norminal current at which a cell will be completely discharged in one hour. For example, 1 C-rate for a 17 mAh cell equals to 17 mA.

A voltage range of 2.0-3.1 V is used for the ML1220 cells, as per the manufacturer's specifications. The open circuit voltage of the cells as shipped is 2.7 V. All cells received were first discharged to 2.0 V at 0.05 mA, and then charged to 3.1 V before testing. Battery charging was performed at a constant current of 1 mA to a maximum voltage of 3.1 V, followed by charging at a constant voltage of 3.1 V until the current dropped below 5 μA. This two-step charging was used to fully charge the cell to 3.1 V after different types of discharge tests, unless otherwise stated.

An example of the testing procedure used for pulse discharge cycling is listed as follows. The duty cycle parameters for this test were: peak current I_p=10 mA, standby current I_s=25 μA, pulse length t_p=100 ms, standby period t_s=2 s.

(1) Let the battery rest for 30 s;

(2) Discharge at 10mA for 0.1 s;

(3) Discharge at 25 μA for 2 s;

(4) Repeat step 2 and 3 until the voltage drops below 2.0 V and collect data every 200 cycles;

(5) Enter a 4-h rest step once the 2.0 V cutoff is reached at any point of discharge;

(6) Charge at 1 mA to 3.1 V;

(7) Charge at 3.1 V until current drops to less than 5 μA.

An example test procedure for pulse discharge and recharge cycling with the following duty cycle parameters: I_p=10 mA, charging current I_c=100 μA, pulse length t_p=100 ms, charging period t_c=10 s and rest period between discharge and charge t_r=2 s.

(1) Let the battery rest for 30 s;

(2) Discharge at 10 mA for 0.1 s;

(3) Rest for 2 s;

(4) Charge at 0.1 mA for 10 s;

(5) Rest for 2 s;

(6) Repeat step 2 to 5 for 20,000 cycles, and collect data every 200 cycles;

(7) Enter a 12-h rest step

(8) Charge at 1mA to 3.1 V;

(9) Charge at 3.1 V until current drops to less than 5 μA.

3.3 Electroanalytical characterization and microscopy

Electrochemical impedance spectroscopy. Electrochemical impedance spectroscopy (EIS) was used to study the system response to the application of a periodic small amplitude ac

signal. This method is now widely applied to the characterization of electrode processes and complex interfaces. EIS tests on ML1220 cells were performed using a frequency response analyzer (Gamry Instruments, PC4-750, EIS 300) with the frequency range of 100 kHz to 50 mHz. In the EIS experiment, the galvanostatic mode is used where a small sinusoidal current was applied to the cell between the cathode and anode, and the response of the voltage was measured. EIS experiments were carried out on fully charged cells that had been allowed to relax at open circuit for 5 hours following charging.

Film conductivity measurement. The effective conductivity, as opposed to the intrinsic conductivity of a material, represents the overall conductivity of a mixture of components such as that found in the cathode of a battery. The effective conductivity of the cathode film was measured with use of a four line probe approach. The four line point probe is similar to a four point probe in that it uses two of the four line probes to pass the current while measuring the voltage with the other two line probes. The effective conductivity was calculated with the following equation:

$$\sigma^{eff} = \frac{I}{V}\frac{l}{A} \tag{3.1}$$

where σ^{eff} is the effective conductivity, I is the applied current, V is the voltage, l is the distance between the inner two lines (i.e. 3.8 mm), and A is the cross-sectional area of the film, which is calculated from the electrode film thickness and width.

The four line probe method is based on changing the geometry of a four point probe so that the film can be contacted by a larger surface area, which should result in a more consistent contact with the film and lower variability in the measurements. This geometry also allows for testing of battery electrode films under pressure. Details for the four line probes designed by the BYU battery lab can be found in ref [63].

Scanning Electron Microscopy. Scanning electron microscopy (SEM) images were obtained using a Philips XL30 S-FEG, operated at 5 keV. For interior views of the cathode structure, the electrode disk was cut to expose a cross sectional view for SEM imaging.

4 TRANSIENT BEHAVIOR DURING PULSE DISCHARGE

4.1 Introduction

The reduction in size and power consumption of electronic devices has enabled development of small autonomous systems for sensing and communication [64]. In spite of accelerated progress in the development of wireless sensors (WSs) and wireless sensor networks (WSNs) over the last decade, the ability to provide power to distributed wireless sensors remains a challenge. Most currently available wireless sensors require batteries as the energy source [6]. However, the desired small form factor for the system often prohibits the use of large capacity batteries. Additionally, in some applications, replacement of on-board batteries can be cost prohibitive or even impossible once the sensors are deployed. Consequently, energy efficiency is of utmost importance in WSN design. There is also a growing awareness that the operating conditions or duty cycle of WSs can greatly impact the amount of deliverable energy available from a battery [17, 22]. A more complete understanding of the influence of WS operating conditions on battery performance and lifetime is critical to our ability to maximize the energy that can be extracted from a given battery in order to prolong the operating life and/or reduce the size of battery-powered WSs.

Lithium or lithium-ion batteries represent an attractive option for use in wireless sensors, due to their high operating voltage and high energy density. Small lithium batteries, either replaceable (primary) or rechargeable (secondary), are commercially available as coin type cells,

whose diameters range from less than 5 mm to 2-3 cm [25]. A number of lithium coin battery chemistries have been developed to meet various application requirements and voltage levels [18]. These include the CR (primary) and ML (secondary) series, which use manganese oxide-based cathodes and a lithium-aluminum alloy anode. For the MT series, lithium titanium oxide is used for the anode to produce a cell with a nominal voltage of 1.5 V, suitable for direct use in a number of consumer applications. Commercial lithium coin cells, in general, are designed to maximize energy density, and are most suitable for low-rate current drain (3-100 μA) applications such as memory backup.

The average power required for wireless sensors is frequently low, since many of them operate on an intermittent duty cycle in order to minimize the power consumption [9, 12, 44, 45]. Duty cycles commonly seen with WSNs consist of very short (tens to hundreds of milliseconds) pulses of mA magnitude separated by much longer "standby" periods where little or no power is required. The resulting average power (on the order of a few to hundreds of μW) can be easily met by lithium coin cells. However, the high power pulses must also be supplied in order to enable functions such as RF transmission and reception. In many cases, the maximum or peak current is orders of magnitude greater than the standby current. The pulse power capability of lithium coin cells must be understood and characterized in order to most effectively use these cells in power systems for WSs. Specifically, an understanding of the transient response of the batteries to intermittent current pulses and a description of the physical processes that determine that response are needed in order to predict battery performance and optimize battery life for WS applications.

In this study we investigate battery discharge characteristics under WS operating conditions, and demonstrate the suitability of small-sized commercial lithium coin cells for

sensor duty cycles. This chapter is focused on electrochemical analysis of the transient pulse discharge and the subsequent relaxation processes that take place in the battery in order to provide a basis for understanding and optimizing battery performance for sensing duty cycles. A quantitative mathematical description of the observed battery behavior is provided as part of this analysis. The knowledge, insight, and tools developed in this chapter are applied in the following chapter where we present, explain and optimize battery performance during discharge and charge for duty cycles characteristic of autonomous microsensing systems.

4.2 Experimental

The most common rechargeable lithium coin cells on the market are MnO_2/LiAl (ML) and V_2O_5/LiAl (VL) cells. The ML cells typically have a higher energy density than the VL cells (e.g. the nominal capacity of ML1220 is 17 mAh compared to 7 mAh of VL1220). ML1220 cells (Panasonic) were chosen for use in this study as the ML1220 is the smallest cell in ML series that is able to provide the 10-20mA pulse current needed for many WSs [9, 12]. The diameter and height of these cells, including the case, are 12.5 mm and 2 mm respectively. The cathode disk inside the case has a diameter of ~7.6 mm and thickness of ~1.0 mm. The ML series cells use a composite manganese oxide for the cathode [39], and a lithium-aluminum alloy for the anode [41]. The electrolyte consists of a lithium-ion conducting salt solvated in ethylene carbonate, butylene carbonate and dimethyl carbonate [42]. The rated capacity at 30 μA between 2.0 V and 3.1 V is 17 mAh. The 2.0-3.1 V voltage range is recommended by the manufacturer to secure a long cycle life, and was adopted for this study.

The open circuit voltage of ML 1220 cells as shipped is about 2.7 V. The cells were first discharged to 2.0 V at 0.05 mA, and then charged to 3.1 V before testing. Battery charging was performed at a constant current of 1 mA to a maximum voltage of 3.1 V, followed by charging at

a constant voltage of 3.1 V until the current dropped below 5 μA. Pulse cycling tests and transient pulse-relaxation tests were performed with a Maccor 4300 battery testing system. Electrochemical impedance spectroscopy (EIS) tests were performed using a frequency response analyzer (Gamry Instruments, PC4-750, EIS 300) over a frequency range of 100 kHz to 0.1 Hz. In the EIS experiment, the galvanostatic mode is used where a small sinusoidal current was applied to the cell between the cathode and anode, and its response in terms of voltage was measured. EIS experiments were carried out on fully charged cells that had been allowed to relax at open circuit for 5 hours following charging. All tests were carried out at room temperature.

4.3 Results and discussion

The battery capacity during continuous, constant current discharge was evaluated for a range of currents between 0.03-50 mA (Fig. 4.1). At low rates (30-50 μA), the observed capacity was essentially the rated capacity of 17 mAh. At moderate to high rates, the capacity decreased significantly with increasing discharge current. The insert shows the battery performance at higher currents (10-50 mA), corresponding to C-rates of 0.6 to 3.0 C. At 10 mA, the discharge time was 275 s and the capacity obtained was 0.76 mAh, about 4.5% of the full capacity. At 20 mA, the battery discharged for ~30 s before the cut-off voltage was reached, and the capacity achieved was less than 0.2 mAh. When the current was higher than 30 mA, the battery reached 2.0 V in less than 3 s, reflecting little usable capacity at that rate. Although 20 mA is only equivalent to a 1.2 C-rate for the battery, it corresponds to a current density of 44 mA/cm^2 based on the geometric area of the cathode disk. When the cross sectional area including the case of the coin cell is considered, the cell delivered ~40 mW/cm^2 at 20 mA, and 1.2 J/cm^2 out of the 125 J/cm^2 total energy available was obtained before the cut-off voltage was reached.

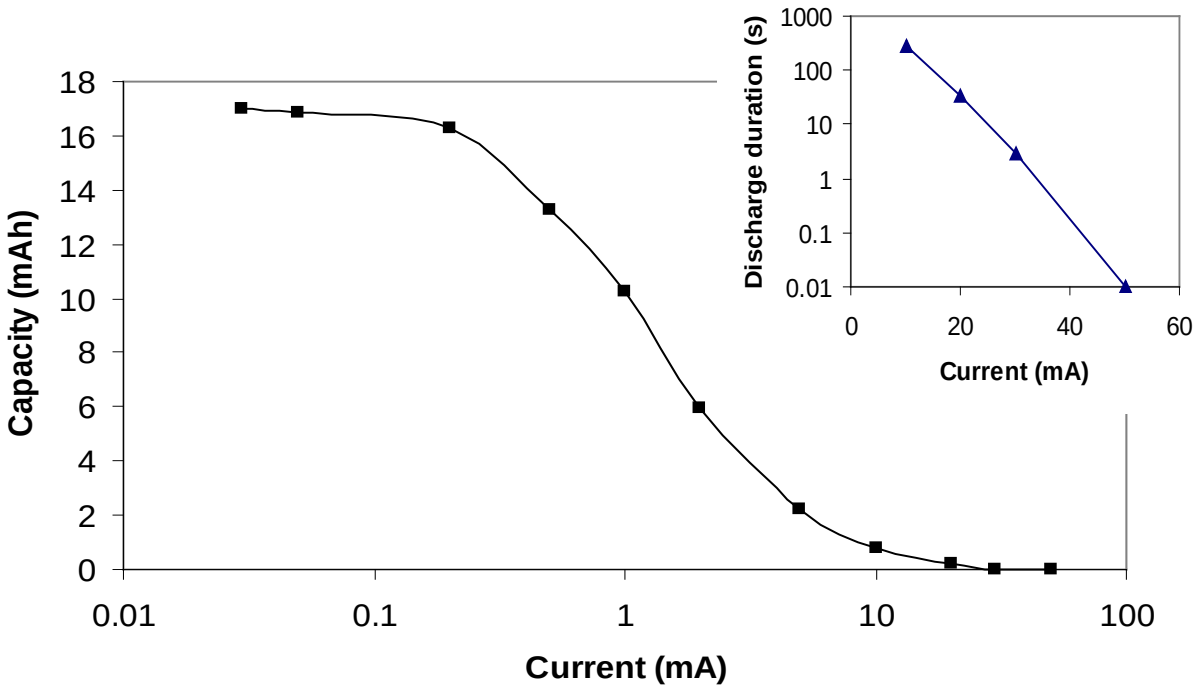

Figure 4.1Performance of ML1220 cells during galvanostatic discharge at different rates (lines are used to guide the eye).

When the battery was pulse discharged (10 mA, 0.1 s pulses and 25 μA, 2 s standby), a recovery of the battery voltage was observed during the standby period. This resulted in a significant increase in capacity relative to a constant current discharge at the same 10 mA rate, as shown in Fig. 4.2. An example of the detailed current and voltage profiles for this duty cycle is shown in Fig. 4.3. Data were collected every 200 cycles, and data for 3 sequential cycles were recorded each time. Figure 4.2 shows the total 201 recordings that appear as 201 pulses, as the 3 sequential cycles overlap on this scale. A total of 40,200 pulses were obtained before the voltage dropped to 2.0 V. The overall capacity of the battery operating under the pulse duty cycle was

11.7 mAh, of which 95% was delivered by the 10 mA peak current. This was about 70% of the full capacity of the cell, and was 15 times higher than the capacity obtained from a continuous discharge at 10 mA. The peak power delivered was 20-28 mW as the voltage decreased along the discharge, which was sufficient to provide the active power needed for microsensors and low-power WSs.

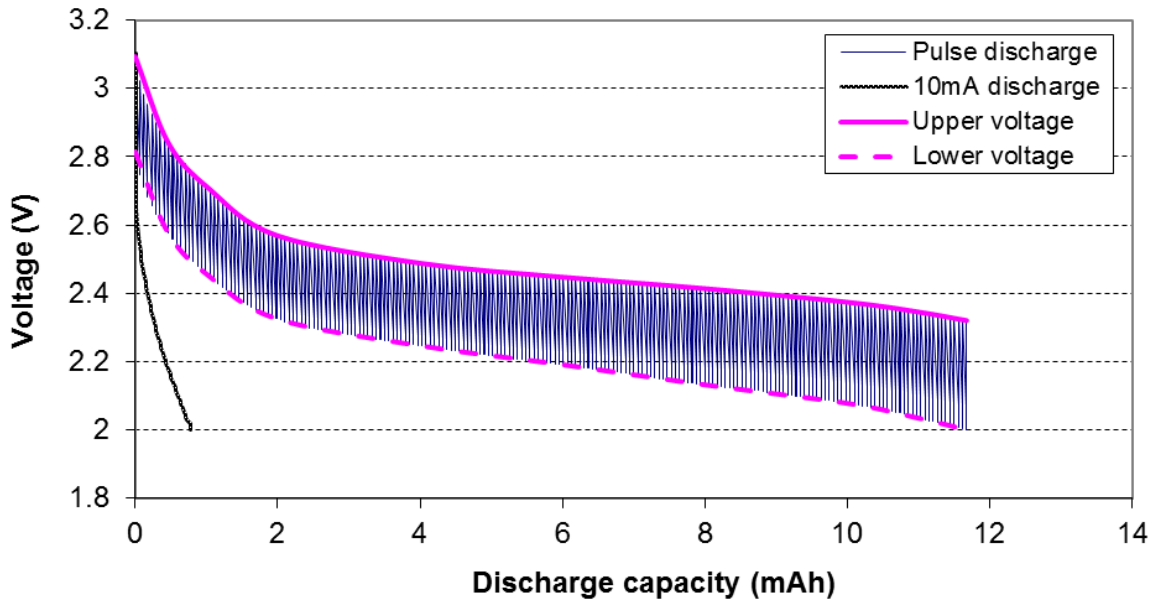

Figure 4.2Pulse discharge of ML1220 using a duty cycle with 10 mA, 0.1 s pulses and 25 μA, 2 s standby between cycles.

During pulse discharge of the battery, the operating voltage varied between an upper and a lower voltage, as shown in Figs. 4.2 and 4.3, where the upper voltage was the highest voltage reached during standby (point B in Fig.4.3) and the lower voltage was the lowest voltage during a pulse (point A). The operating voltage plays a key role in determining battery lifetime and power in wireless sensing systems. The full discharge capacity for the battery under a given duty cycle is assumed to be reached when the battery voltage drops below the lower limit specified for

the cell. For a WS system, this limit will be reached during a discharge pulse where point A in Fig. 4.3 drops below the cut-off voltage. The upper and lower voltages of the pulse discharge depend on losses associated with the various electrochemical processes taking place in the cell.

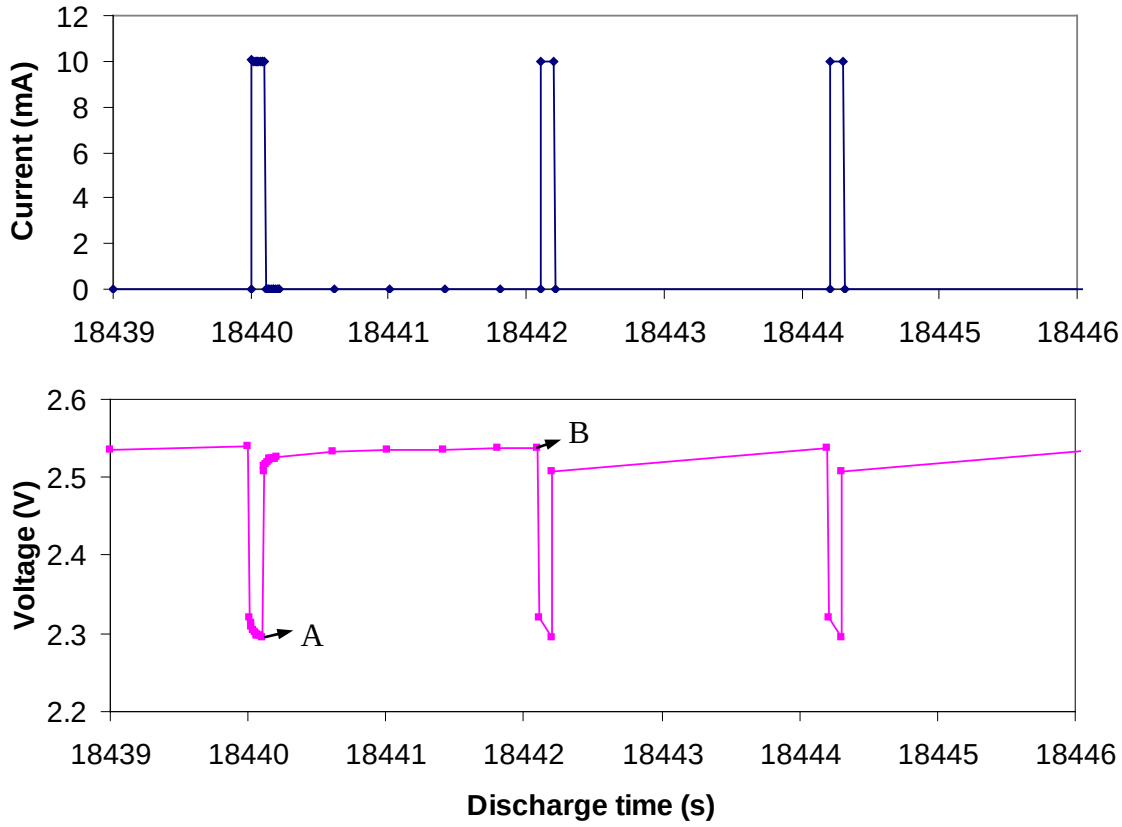

Figure 4.3 Current and voltage profile of the 8801th-8803th cycle of the pulse discharge described in Fig. 4.2.

Important aspects of this study include identification of the dominant electrochemical processes that control the behavior of the battery, and the development of a theoretical description of those processes that includes the time dependent cell voltage observed during pulse discharge. The need for this information is evident from the results shown in Fig. 4.2, where use of pulse discharges with intermediate relaxation increased the capacity of the battery

by a factor of 15 over the capacity observed at the same rate under constant discharge conditions. An understanding and quantitative description of battery behavior during WS duty cycles will provide a basis for optimizing battery and system performance and lifetime.

4.3.1 Transient analysis of pulse discharge

Figure 4.4 shows voltage vs. time data for 5 mA, 10 mA and 20 mA pulses of 400 ms duration that were initiated from an initial open circuit potential (OCP) of 3.1 V. Data were recorded every 10 ms during the first second following initiation of the pulse, and then at longer time intervals (0.1 s) for the balance of the relaxation period. The voltage profiles, both during and after the pulse, had two parts: a region of rapid voltage change and a region of slower change. When the current was applied, there was an immediate voltage drop, dV1, which was estimated as the difference between the open circuit voltage before the pulse and the voltage at the first measurement point (t = 10 ms). As time increased, the cell voltage continued to decrease due to the mass transport processes in the battery. The voltage change, dV2(t), is measured relative to the voltage at 10 ms. In Figure 4.4, dV2 shows the voltage change from t = 10 ms to t = 400 ms, i.e. dV2(400 ms). After the current was interrupted, an immediate voltage rise was observed. This voltage change, labeled as dV3, was determined by the difference between the end of discharge voltage at 400 ms and the voltage corresponding to the first data point of relaxation at 410 ms. Following this immediate voltage jump, there was a slower relaxation stage until the voltage remained constant at the open circuit value (relaxation at longer times not shown in the figure). This voltage change, dV4(t) was determined by the difference between the voltage measured 10 ms after completion of the pulse (410 ms for this example) and the final value at or near the open circuit voltage of the battery. Because the pulse duration was very short, the change in the state-of-charge of the battery was negligible. For example, a 400 ms,

20 mA pulse discharge consumed a capacity of 0.002 mAh, which changed the battery capacity by only 0.013%. For this reason, the equilibrium potential of the battery was considered to be the same before and after the pulse discharge.

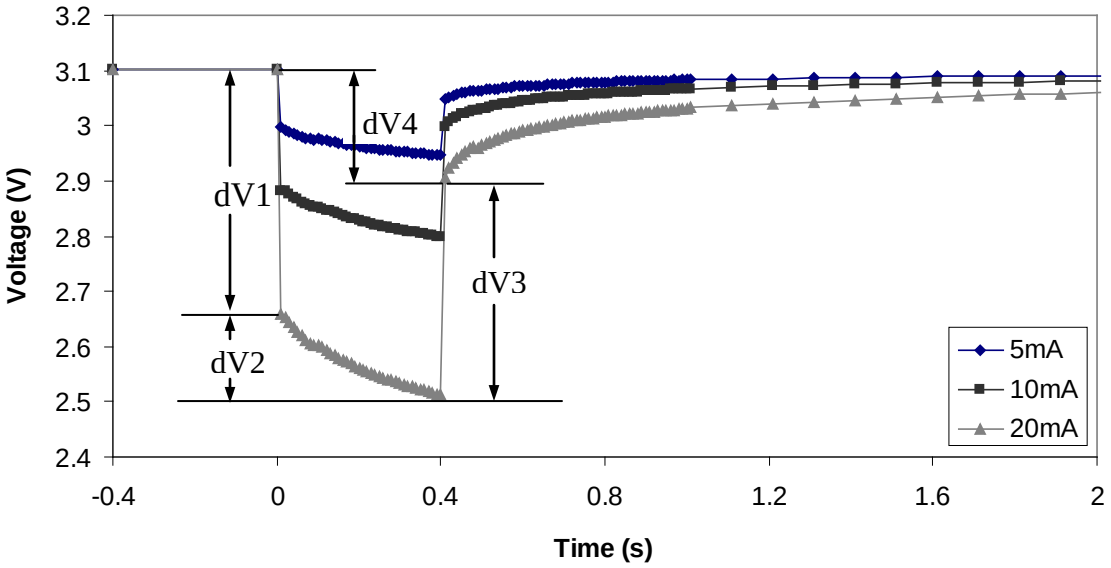

Figure 4.4 Voltage response to 400 ms long 5 mA, 10 mA and 20 mA pulses (voltage change illustration labeled for the 20 mA pulse)

In order to recognize the processes important to the short time scales of interest, electrochemical impedance spectroscopy (EIS) was performed on fully charged ML1220 cells. Figure 4.5 shows the Nyquist plots where the imaginary part of the impedance was plotted as a function of the real part, with low frequencies at the right and high frequencies at the left in the graph (0.1-100k Hz). The intercept of the semicircle and the Zreal axis at high frequencies (~100k Hz) yielding a value of ~13 Ω for the battery, which includes both ionic and electronic resistances. These resistances are characterized by a linear relationship between current and voltage, and dominate the behavior at high frequencies where other resistances are not important.

IR losses/recovery constitute a significant portion of the rapid voltage changes dV1 and dV3 shown in Fig. 4.4.

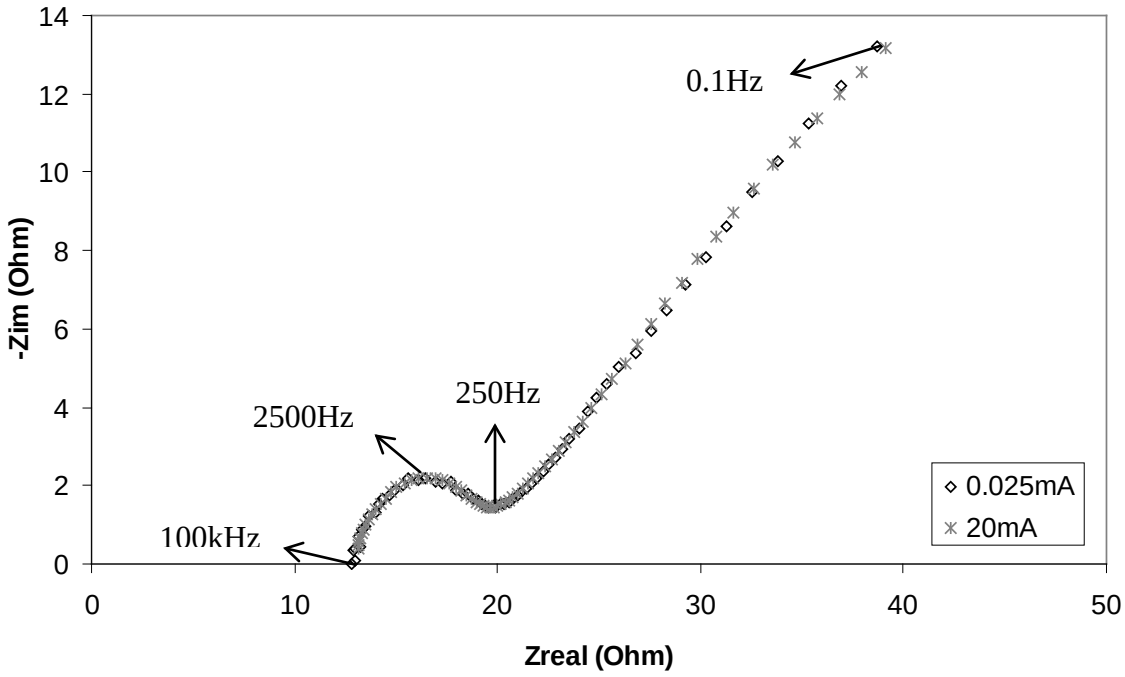

Figure 4.5 Nyquist plot of EIS results for the ML1220 for a fully charged cell (OCV = 3.1 V) at two different current amplitudes

The complex impedance in the mid-frequency range (250-60 kHz) includes the influence of both the double-layer capacitance and the charge-transfer resistance of the battery [33]. The time constant for double-layer charging was estimated from the frequency (~2500 Hz) at the top of the semicircle as ~0.5 ms [65]. Because this time is short relative to the times of interest to the current study, double layer charging was not included in our transient modeling. The approximately linear portion of the Nyquist plot at low frequencies (0.1-250 Hz) is associated with diffusion effects in both the electrolyte and the solid phase active material.

In Figure 4.5, EIS experiments were carried out at an RMS current amplitude of 25 μA, as well as at a much higher value of 20 mA. The variation of impedance with current can be used to investigate the kinetic behavior of the battery [66]. If the relationship between current and surface overpotential is exponential, as is frequently the case, the observed kinetic impedance should decrease as the current increases. In contrast, when the current varies linearly with the surface overpotential, the resulting impedance will not depend on the amplitude of the current. As seen in Fig. 4.5, the 20 mA and 25 μA curves are essentially the same, indicating linear kinetics over the current range used in our studies.

The rapid voltage change (dV1 and dV3 in Fig. 4.4) that occurred at the beginning and ending of each pulse was further analyzed and plotted against the applied current in Fig. 4.6. This rapid voltage change was caused by the total of IR resistance and kinetic resistance of the cell. From the EIS results, the Ohmic and kinetic resistances were estimated as 13 Ω and 7 Ω respectively. The total resistance added up to ~20 Ω, which at 5, 10 and 20 mA should cause a voltage drop of 0.1, 0.2 and 0.4 V respectively. These values compare reasonably well with the observed voltage changes shown in Fig. 4.6. Both dV1 and dV3 were linearly proportional to the applied pulse current, consistent with the linear kinetics described above. The fast voltage change after the pulse (dV3) is a rapid relaxation of the overpotentials associated with dV1, and should be similar in magnitude to dV1. The difference between dV1 and dV3 at the same current is likely due to the effects of local composition.

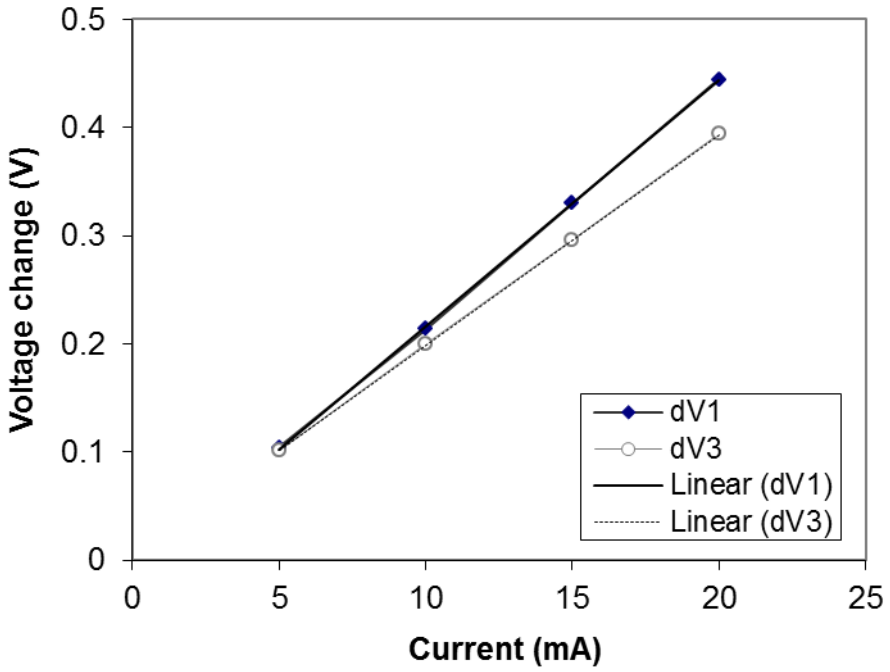

Figure 4.6 The rapid voltage change during (dV1) and after (dV3) current pulses of different magnitude.

While the rapid voltage change dV1 was a function of only the pulse current, the slower voltage change dV2 during the pulse appeared to depend on both current and time. When dV2 in Fig. 4.4 was plotted against the square root of the time, a linear relationship was immediately apparent (see Fig. 4.7). The slightly irregular voltages between 0.25-0.3 $s^{1/2}$ are an artifact caused by the testing system software around t = 60-90 ms due to a time step adjustment during data collection. Because dV2 was calculated relative to the voltage at 0.01 s, dV2 was zero at $\sqrt{t}$ = 0.1 $s^{1/2}$ for all currents. This, of course, is an approximation as the effects related to composition change begin immediately. The intercepts extrapolated from the linear correlations to t=0 are related to the voltage changes that took place in the first 0.01 s. The square root of time dependence is characteristic of that observed for the concentration during transient diffusion, which may be important in this system. The slopes of the curves increased with current (for a

constant pulse width of 400 ms), with the magnitude of the slope roughly proportional to the current.

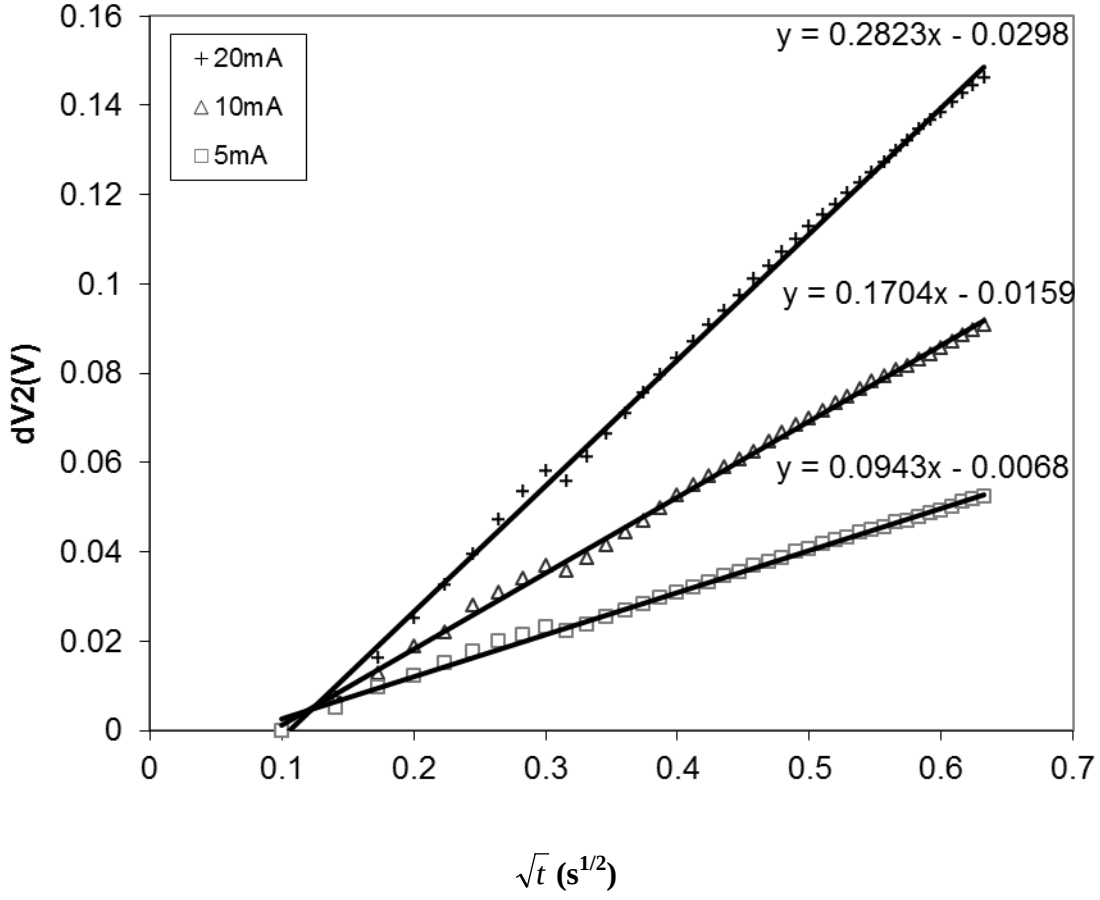

Figure 4.7 Transient voltage change as a function of the square root of time during the 0.4 s pulse discharge at currents of 5, 10 and 20 mA.

A similar linear relationship between the voltage and the square root of time was observed by Weppner and Huggins [67] for a Li_3Sb electrode. Their experiments, performed on dense planar electrodes, showed a linear relationship between voltage and solid-phase concentration over a limited range of SOC, and voltage/time behavior that was controlled by diffusion in the solid phase. The applicability of these conditions to the cells of interest to the

present study is examined below. In doing this we note that, in contrast to the planar electrodes used by Weppner and Huggins, the ML1220 cells have a thick porous cathode, and application of their analysis to the present study will require a knowledge of the current distribution in the porous electrode.

As we seek a quantitative description of the slow transitions that take place during pulse discharge and relaxation (see Fig. 4.4), an understanding of the physical processes that control cell performance is critical. In ML1220 cells, the cathode layer (1 mm) is much thicker than the separator (50-100 μm) and the LiAl anode layer (100-200 μm). The lithium diffusion coefficient of LiAl alloy was found to be on the order of 10^{-6} cm^2/s at 415 ˚C [68] and 10^{-9} cm^2/s at room temperature [69], which is significantly higher than that of the manganese oxide material used in the cathode. For a lithiated manganese dioxide ($Li_{0.33}MnO_2$), the diffusion coefficient was in the range from 3×10^{-12} to 6×10^{-11} cm^2/s [70]. Moreover, the LiAl alloy anode is typically cycled across a two-phase (α+β) region, within which the voltage of the LiAl electrode remains constant during lithium insertion and extraction [71]. Therefore, it is unlikely that the slow changes in voltage observed during pulse discharge are due to the anode. It is hence reasonable to expect that the transport processes in the cathode dominate the transient voltage change during the pulse.

As we examine transient transport in the cathode, we first consider the role of liquid phase transport. At room temperature, the diffusion coefficient of the electrolyte is generally in the range of 2×10^{-6} - 4×10^{-6} cm^2/s depending on the lithium ion concentration [72]. Since the detailed composition and properties of the electrolyte are unknown, we assume a diffusivity value on the lower end, 2×10^{-6} cm^2/s, for calculation purposes. If the Li concentration is 1M, and the porosity of the cathode layer is 0.4, the total amount of Li^+ in the liquid phase of the cathode

is ~1.8×10^{-5} mole. A 20 mA 0.4 s pulse consumes ~8.3×10^{-8} mole of Li^+ in the cathode and releases the same amount of Li^+ to the electrolyte in the anode. This should cause little change to the bulk concentration of the electrolyte in the cathode. The Li-ion concentration at the electrode surface may vary somewhat from that of the bulk, but the associated overpotential is not expected to be large due to the large interfacial area of the porous electrode and the short discharge time. Indeed, an estimate of the concentration overpotential associated with differences in the concentration between the particle surface and the bulk of the pore was only 0.2 mV. Consequently, it appears that the solid phase mass transfer in the cathode is the dominant contributor to the voltage change during the pulse.

To gain insight into the current distribution across the cathode, the dimensionless exchange current [31] is considered for linear kinetics:

$$\nu^2 = (\alpha_a + \alpha_c)\frac{Fai_0L^2}{RT}\left(\frac{1}{\kappa^{eff}} + \frac{1}{\sigma^{eff}}\right) \qquad (4.1)$$

If ν^2 is large, the reaction distribution in the electrode is non-uniform. The penetration depth, within which reaction rates are appreciable, can be estimated by L/ν, where L is the thickness of the electrode. α_a and α_c are the apparent transfer coefficients, (often taken to be 0.5 for lithium batteries), F is Faraday's constant, R is the ideal gas constant and T is temperature (298 K for this study). Physical parameters include: a, the specific surface area per volume; κ^{eff}, the effective conductivity of the electrolyte; σ^{eff} the effective electronic conductivity of the matrix; and i_0, the exchange current density.

For initial calculation, the particle size (R_p= 3 μm) and cathode porosity (ε=0.4) were assumed based on SEM images of the cathode. The dependence of the results on these values will be shown later. The specific surface area can be estimated from R_p and ε for spherical particles by

$$a = \frac{3(1-\varepsilon)}{R_p} \tag{4.2}$$

To obtain the electronic conductivity of the cathode layer, the cathode was removed from the battery, washed in a diethyl carbonate solvent, and dried in a glovebox. The conductivity was then measured with use of a four point probe [63, 73]. The measured value of 0.52±0.04 S/cm represents the effective conductivity σ^{eff} of the cathode matrix consisting of conductive additives, active material, and polymer binder. The ionic conductivity of the electrolyte is about 0.01 S/cm at room temperature, based on a solution of 1M $LiPF_6$ in carbonate solvent mixtures [72]. The effective conductivity of the electrolyte, κ^{eff}, is the bulk conductivity corrected by volume fraction of the liquid phase in the cathode as follows [24],

$$\kappa^{eff} = \kappa\varepsilon^{1.5} \tag{4.3}$$

This value is always less than the intrinsic value since $\varepsilon < 1$. The value of $\kappa^{eff}/\sigma^{eff}$ is therefore less than 0.01/0.52 or 0.019. Small values of $\kappa^{eff}/\sigma^{eff}$ indicate that the reaction occurs preferentially near the electrode-solution boundary close to the separator region [31].

The exchange current density can be inferred from the following relationship for linear kinetics [24]:

$$i = i_0 \frac{(\alpha_a + \alpha_c)F}{RT}\eta_s \tag{4.4}$$

Equation (4.4) can be rewritten as

$$i_0 = \frac{RT}{(\alpha_a + \alpha_c)F}\frac{1}{\frac{\eta_s}{i}} = \frac{RT}{(\alpha_a + \alpha_c)F}\frac{1}{R_{ct}} \tag{4.5}$$

Since the LiAl anode is known to have higher exchange current densities [74, 75], the kinetic resistance obtained from the EIS result in Fig. 4.5 was due principally to the reaction at

the cathode. R_{ct} was estimated to be 3 Ω-cm^2 based on the cross sectional area of the cathode disk, and the superficial i_0 based on this area was calculated as 8.0 mA/cm^2. The actual interfacial area for reaction was estimated as $a \cdot S\frac{L}{\nu}$, where S is the cross-sectional area of the cathode. The penetration depth L/ν was assumed to be the same for short current pulses and for high frequency AC experiments. If R_{ct} is expressed in terms of $a \cdot S\frac{L}{\nu}$, Eqs. (4.1) and (4.5) can be solved simultaneously by iteration to yield a ν^2 value of 188. The resulting penetration depth, L/ν, was 73 μm, much less than the electrode thickness of 1 mm. Thus, the reaction takes place preferentially at the separator-electrode interface in a region of ~70 μm.

During a short discharge pulse, diffusion in the solid phase can be approximated as a 1-D planar system, since solid diffusion only reaches a very thin layer on the surface of the active particle (diffusion length $2\sqrt{Dt}$ is 0.04 μm when t=0.4 s, D=10^{-11} cm^2/s). The governing equation for transient mass transfer under these conditions is Fick's second law,

$$\frac{\partial c}{\partial t} = D\frac{\partial^2 c}{\partial x^2} \tag{4.6}$$

The initial and boundary conditions are

$$t = 0 \qquad c = c_0 \tag{4.7}$$

$$t > 0 \qquad -D\frac{\partial c}{\partial x}\Big|_{x=0} = \frac{i}{F} \tag{4.8}$$

$$c(\infty, t) = c_0 \tag{4.9}$$

with x=0 as the surface and $x=R_p$ as the center of the active particle. D is the solid phase diffusion coefficient, and i and c_0 are current density and initial concentration, respectively. We assume that the reaction distribution is uniform inside the reaction zone. The local current

density i can then be calculated based on the interfacial area $a \cdot S \frac{L}{\nu}$. When t << R_p^2/D, the solution of Eq. (4.6) under conditions (4.7) - (4.9) can be approximated as

$$c(x=0,t) = c_0 + \frac{2i\sqrt{t}}{F\sqrt{\pi D}} \tag{4.10}$$

The change in the cell voltage can be related to the change in the solid surface concentration in Eq. (10) by thermodynamics, i.e. the coulometric titration curve of the active material. The result is an equation that describes the time dependence of the voltage in terms of the electrochemical and material properties of the lithium intercalation material [67]:

$$\frac{dE}{d\sqrt{t}} = \frac{2V_m}{\sqrt{\pi D}} \frac{i}{F} \frac{dE}{dy} \tag{4.11}$$

where V_m is the material molar volume and dE/dy is the slope of the voltage vs. composition curve of the active material. The change in V_m, D and dE/dy with composition can be neglected for a short pulse, so $dE/d\sqrt{t}$ should be linear with respect to the current density i, consistent with the results in Fig. 4.7. Equation (4.11) can be rearranged to calculate the solid diffusion coefficient [67]:

$$D = \frac{4}{\pi} \left(\frac{i \cdot V_m}{F}\right)^2 \left(\frac{dE/dy}{dE/d\sqrt{t}}\right)^2 \tag{4.12}$$

With the above equation, we calculated the diffusion coefficient of the Li_yMnO_2 cathode material used in ML cells. Here V_m was assumed to be the molar volume of MnO_2. This is a reasonable approximation, given that the molar mass of Li_yMnO_2 varies little from MnO_2, and the density of most lithium manganese oxide material (e.g. $Li_yMn_2O_4$ [76]) varies typically within 20% of that of MnO_2. dE/dy at 3.1V was measured with use of data from Ref [74], and $dE/d\sqrt{t}$ was obtained from Fig. 4.7 at 5, 10 and 20mA. We estimated the diffusion coefficient

D to be $(3.9\pm1.2)\times10^{-11}$ cm^2/s, which was very close to the values reported in [70]. In contrast, D was incorrectly calculated to be 2.7×10^{-13} cm^2/s if a uniform current distribution was assumed for the entire cathode and the total interfacial area was used for current density calculation, illustrating the importance of accounting for the non-uniform current distribution in thick electrodes.

The calculations above are based on estimated values of porosity and particle size. The impact of these two parameters was evaluated, and the results are shown in Fig. 4.8. The results indicate that the penetration depth increases with porosity, but changes little with particle size, and the resulting diffusion coefficient increases with decreasing porosity and increasing particle size. In Eq. (4.2) the specific area decreases with either increasing porosity or particle size, leading to a decrease in ν. Increasing the porosity also increases the values of κ^{eff}, causing L/ν to increase. The particle radius is varied over a relatively wide range, which causes a significant change in the specific area. The reaction area depends on both specific area and penetration depth. The diffusion coefficient decreases with increasing porosity when the change in L/ν dominates. D varies over an order of magnitude when the particle radius varies from 1 μm to 4 μm, which is driven by the change in the specific area a. It is clear that the calculated diffusion coefficient is affected by both porosity and particle size. However, the variation caused by uncertainties in these design parameters is small relative to that resulting from the assumption of a uniform current distribution throughout the porous electrode, and can be minimized with improved information regarding the structure and properties of the electrode.

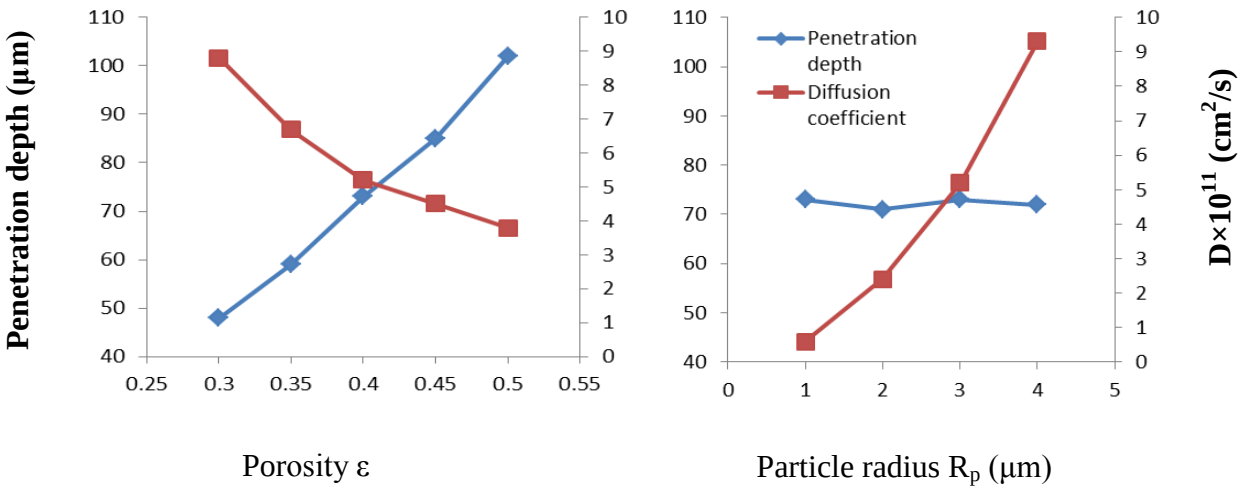

Figure 4.8 Influence of porosity and particle size on the penetration depth and solid diffusion

Equation (4.11) can be integrated over the pulse length to yield an expression for the voltage change. In Fig. 4.7, dV2 was measured relative to the voltage at t=10 ms. By including the voltage changes in the first 10 ms (the y-intercepts), we have the total voltage change during the pulse relative to the voltage at t=0 as:

$$\Delta V_p = F_1 \cdot \frac{I}{F_2} \cdot \sqrt{t} \qquad (4.13)$$

where ΔV_p varies linearly with applied current I and with square root of time, $F_1 = \frac{2V_m}{\sqrt{\pi D}} \frac{1}{F} \frac{dE}{dy}$, and $F_2 = a \cdot S \frac{L}{\nu}$. F_1 is a function of the material properties of the battery including the solid diffusion coefficient, molar volume and thermodynamics; F_2 reflects the influence of battery design parameters like electrode thickness, geometric area, particle size and porosity. For the short pulses used in WSs, F_1 and F_2 can be approximated as constants when the battery state-of-

charge (SOC) does not change appreciably. When these electrochemical parameters are not available, data from a single short pulse can be used to determine F_1 and F_2 from the relationship between the voltage and $\sqrt{t}$ as shown in Fig. 4.7.

Equation (4.13) can be used for quick and easy estimation of the voltage change under various pulse conditions at a given SOC. When combined with the linear relationship between the instant voltage drop dV1 and the applied current, the total voltage change for the pulse can be predicted to yield an estimate of the lower voltage. Caution need to be paid to both the current and pulse length range where the above linear relations strictly hold true. For pulse current no greater than 20 mA, the linear dependence of the voltage on the square root of time was found valid for pulse length up to 1 s, with lower current having longer linear region (e.g. 2 s for 5 mA). At higher current (e.g. 20 mA), a deviation from the linear dependence of the voltage on the applied current (~20% lower) was also found, as shown by the slopes in Fig. 4.7. Possible explanations include a significant change of the thermodynamic factor over the pertinent stoichiometric range at longer times or at higher currents, which were discussed in more detail in Ref. [67]. In the case of ML1220 cells, the deviation may also be due to the non-uniform reaction distribution inside the reaction zone and the resulted non-uniform local solid surface concentration.

4.3.2 Transient analysis of relaxation

In the previous section we established solid phase diffusion as the primary factor that controlled the rate of voltage change beyond the initial voltage drop associated with kinetic and ohmic effects. This section focuses on the relaxation behavior after a pulse discharge. As illustrated in Fig. 4.4, the voltage profile after a pulse consists of an initial rapid change due to

immediate relaxation of the voltage losses associated with kinetic and ohmic resistances, followed by a period of slower change that is associated with relaxation of the concentration gradient in the solid phase. The slow concentration relaxation is critical and is likely the reason for the difference between the low capacity observed for constant current discharge and the much higher capacity observed for pulse discharge at the same rate, but with time for relaxation between the intermittent pulses (see Fig. 4.2). The interaction of duty cycle and relaxation needs to be understood in order to predict the battery performance in WSs. In this section we quantify the relaxation behavior with use of a transient voltage analysis similar to that used in the previous section.

The voltage profile for the relaxation period is shown in Fig. 4.9 for a variety of different discharge pulses, each with a current between 5 and 20 mA and duration between 100 and 400 ms. The transient voltage change, $dV4(t)=V_{OCP}-V(t)$, is plotted as a function of the inverse square root of time in Figs. 4.10 and 4.11. The relaxation time used in Figs. 4.10 and 4.11 is defined as zero at the end of the discharge pulse, and increases from that point. In this section we use t for relaxation time, and τ for a specified pulse length previous to a relaxation period. The discontinuity in the voltage curves evident for time axis values of approximately 3.5 $s^{-1/2}$ is due to an artifact of the measurement system as mentioned above.

Because the rapid voltage changes dV1 and dV3 are similar in magnitude, dV4 at the beginning of the relaxation is similar in magnitude to dV2 at the end of a pulse, i.e. $dV4(t=0) \approx dV2(\tau)$ (see Fig. 4). It is apparent from Fig. 4.9 that the magnitude of the voltage change during relaxation increased with increasing pulse current and length. The rate of change of dV4 was greatest at the beginning of the relaxation period, and slowed as the concentration gradient relaxed. dV4 varied linearly with $1/\sqrt{t}$ at relaxation times greater than ~ 0.5 s ($1/\sqrt{t} < 1.4$ $s^{-1/2}$)

for all the pulses shown in Figs. 4.9 and 4.10. In addition, pulses of different current and duration approached the same limit if the amount of charge passed during the pulse was the same. For example, in Figs. 4.9 and 4.10 we see that the dV4 values for the (20 mA, 200 ms) and (10 mA, 400 ms) pulses were very close in magnitude for $1/\sqrt{t}$ <1.4. Figure 4.11 provides an expanded view of the curves that illustrates the linearity for times greater than 0.5 seconds; for clarity, the curves that are overlapped with the relaxation voltage for (5 mA, 400 ms) and (10 mA, 400 ms) pulses are not shown in Fig. 4.11.

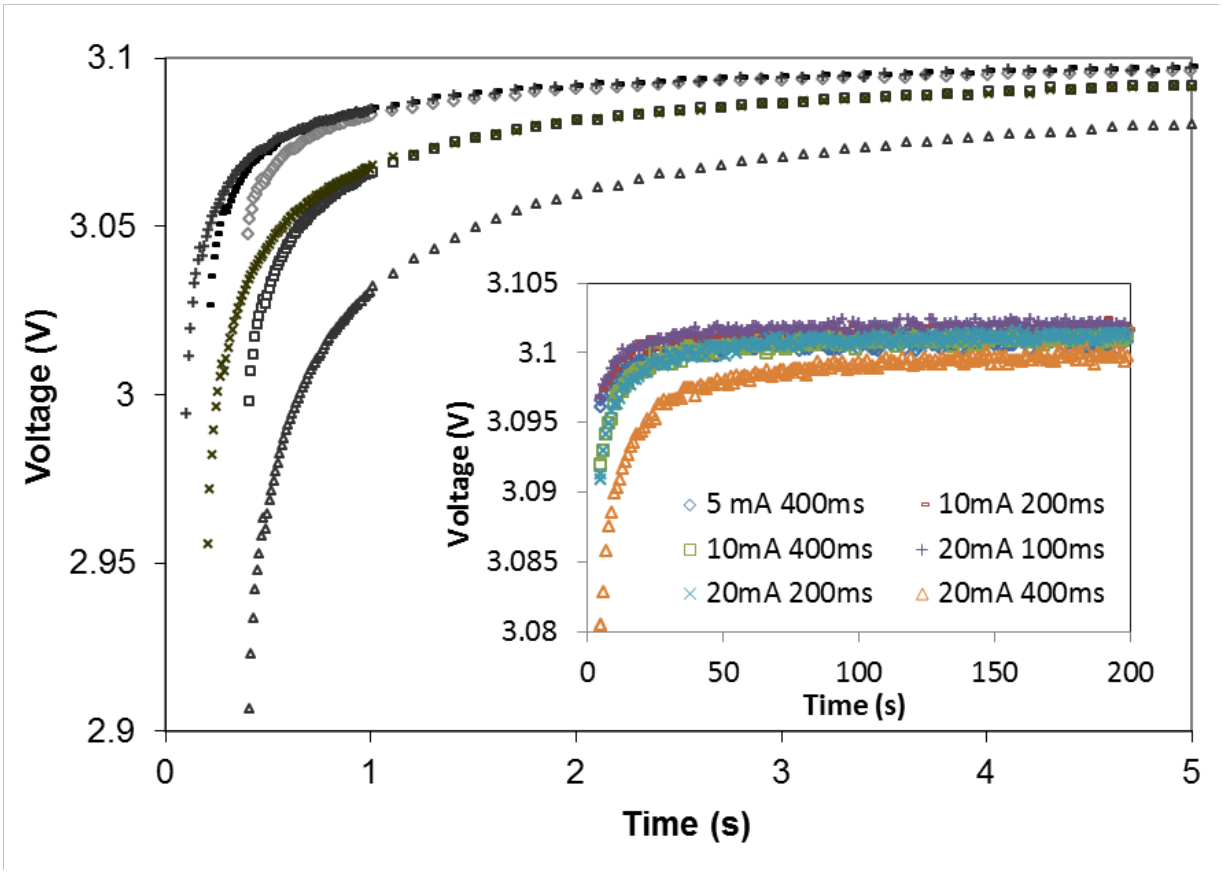

Figure 4.9 Voltage relaxation curves following pulses of various currents and lengths. Time is measured from the initiation of the pulse. Insert: relaxation curves for test times from 5-200 s.

The voltage at short times reflected the impact of the local concentration gradient. For example, at t=0.01 s (right axis of the graph), dV4 for the (20 mA, 100 ms) pulse was the same as that for the (10 mA, 400 ms) pulse, but later dropped to a lower value due to the lower amount of charge passed during the pulse. The initial value reflected the fact that the surface concentration and local gradient are higher for the higher current pulse, giving a temporarily higher voltage loss that subsequently relaxed to the value expected from the amount of charge passed.

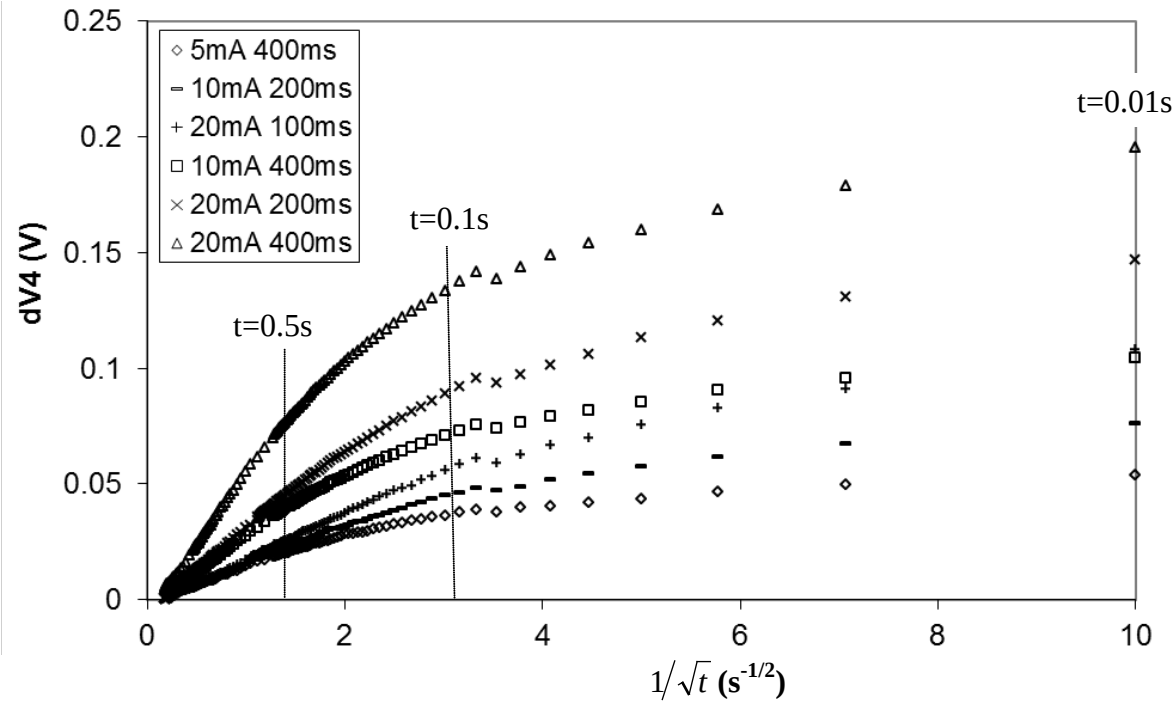

Figure 4.10 Transient voltage change versus $1/\sqrt{t}$ during relaxation for $t = 0.01$-30 s

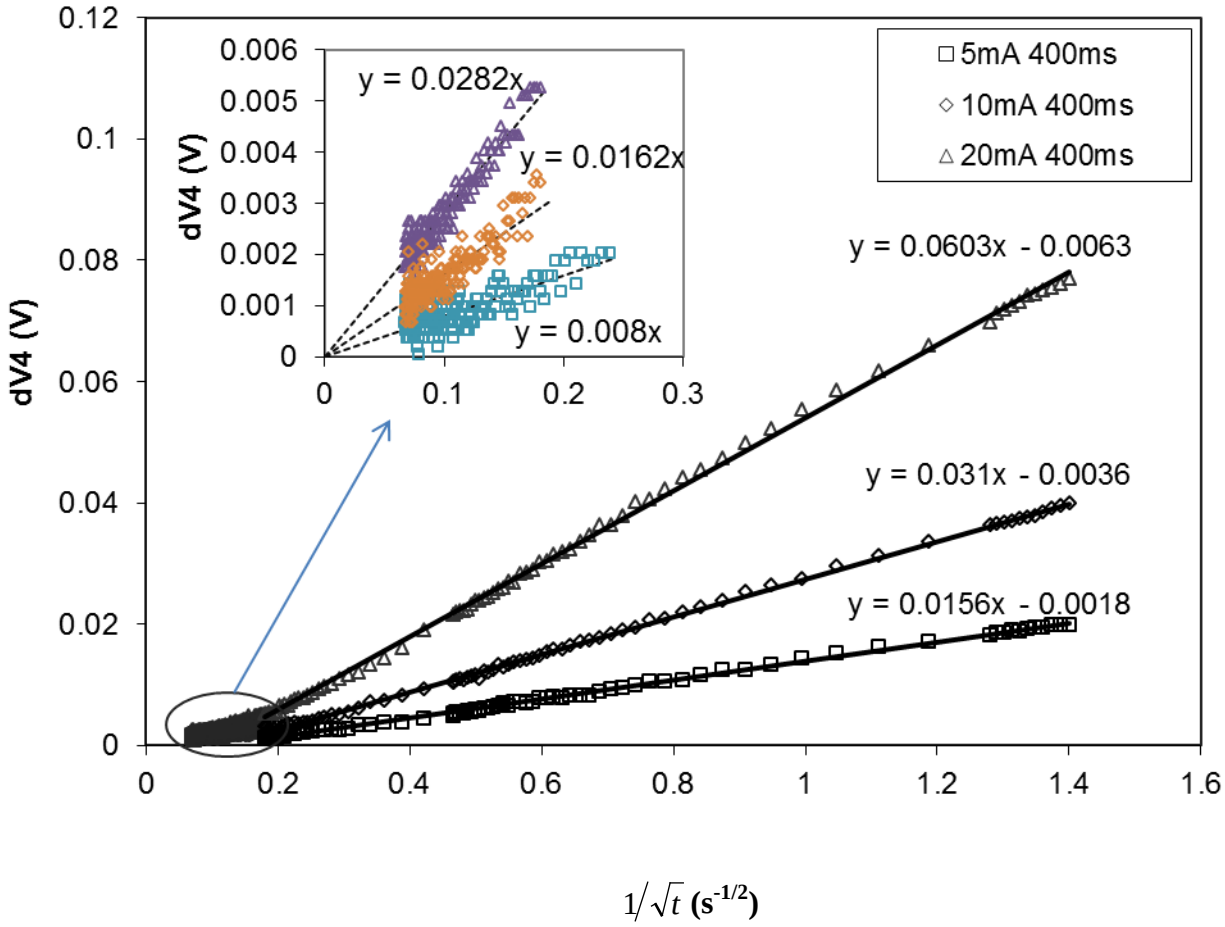

Figure 4.11 Transient voltage change versus $1/\sqrt{t}$ during relaxation for $t = 0.5$-30 s (Insert for $t = 30$-200 s)

At longer times ($t = 0.5$–30 s), the initial concentration distribution in the thin outer layer of the active material particle is of less importance, and diffusion into the bulk of the particle becomes analogous to that of a known quantity of the diffusing species at the surface of the particle that undergoes semi-infinite diffusion. Diffusion in the solid phase can be approximated as a 1-D system because the solid diffusion penetration length ($2\sqrt{Dt}$ = 0.4 μm at t=30 s) is small relative to the active particle radius (3 μm). The solution for Fick's second law thus can be expressed as [77]

$$c(x,t) = c_0 + \frac{M}{\sqrt{\pi D t}} \exp\left(\frac{-x^2}{4Dt}\right) \qquad (4.14)$$

where c_0 is the concentration in the particle prior to the pulse (assumed to be uniform), x is the distance from the surface of the particle, and M is the total amount of material added during the pulse per surface area. M is assumed to be present at the surface of the particle in this calculation and can be calculated from the current density i and the pulse length τ by $M = i\tau/F$. The current density, i, should be calculated based on the actual interfacial area $a \cdot S \frac{L}{\nu}$, as illustrated in the previous section.

Similar to the derivation of equations (4.11) and (4.12), the change of voltage can be related to the change of lithium concentration at the surface of the active particle (at x=0) as follows:

$$\frac{dE}{d(1/\sqrt{t})} = \frac{V_m}{\sqrt{\pi D}} \frac{i \cdot \tau}{F} \frac{dE}{dy} \qquad (4.15)$$

Equation (4.15) shows that $dE/d(1/\sqrt{t})$ should vary linearly with the current level and pulse length, consistent with the experimental results shown in Figs.4.10 and 4.11. Note that the voltage change in the region where Equation (4.15) is valid depends only on the product of the pulse current and the pulse time, consistent with the overlapping results noted earlier. As expected, and consistent with Eq. 4.15, the slopes of the lines in Fig. 4.11 were proportional to the pulse currents at a constant pulse length of 400 ms. With the same physical parameters used in the previous section and the $dE/d(1/\sqrt{t})$ data from Fig. 4.11 (t=0.5-30 s), we used Equation (4.15) to estimate the diffusivity as $D = (4.3\pm0.3)\times10^{-11}$ cm^2/s. This value agrees well with the value of 3.9×10^{-11} cm^2/s obtained from Equation (4.12) using the pulse data instead of the relaxation data used here. The agreement between the diffusivities estimated from the two

equations, the linearity of the data with the expected functions of time, the linear dependence of the slopes on the current density for a given pulse length, and the overlap of curves with similar values of $i \cdot \tau$ all confirm the validity of the relationships used to describe voltage changes with time both during the pulse and during relaxation.

At long times (30-200 s), the rate of voltage change became slower than that expected from Eq. 4.14, as shown in the inset of Fig. 4.11. The reason for this behavior is likely that the assumption of planar semi-infinite diffusion (Eq. 4.14) is no longer valid at long times. Other factors may also contribute, such as the redistribution of lithium ions from the reaction zone to other areas on the electrode. When the cell voltage is relaxed to within 2 mV of the OCV, the change in cell voltage becomes comparable to the measurement noise (2 mV is the voltage resolution of the Maccor battery testing system used), making observation of further voltage relaxation impossible. We thus define a "near full relaxation" as cell voltage relaxation to within 2 mV of the OCV for a certain state-of-charge.

Although over 50% of the overall voltage relaxation took place within the first 0.5 s after the pulse (the "short time" region in Fig. 4.10 at $1/\sqrt{t}$ >1.4), the standby time intervals, within which a WS is most likely to operate, correspond to the linear region shown in Fig. 4.11 (seconds to minutes). About 80% of the overvoltage due to diffusion effects is relaxed within 2 s of relaxation in the intermediate linear region (0.5-30 s), and only 2-5% of voltage change takes place in the long time relaxation region (30 s or longer). Because the establishment of concentration gradients leads to voltage losses, the extent of time available for relaxation may have a significant impact on the available capacity and performance of a battery under WS cycle conditions. In the next chapter, these impacts are demonstrated experimentally and discussed in the context of the limiting processes identified in this work.

Cell voltage during relaxation can be estimated based on the above linear relationships and Eq. (4.15). In the intermediate linear region, Equation (15) can be integrated to yield:

$$\Delta V_r = F_3 \cdot \frac{I \cdot \tau}{F_4} \cdot \frac{1}{\sqrt{t}} \qquad (4.16)$$

where ΔV_r is the variation of voltage from the OCP, which varies linearly with the inverse of square root of time, current I and length τ of the pulse applied just prior to the relaxation. When the y-intercepts (in Fig. 4.11) are small relative to the voltage change of interest, this should introduce little error, especially at short relaxation times of less than 5 s. To be more precise, the OCP used for ΔV_r can be corrected by the y-intercepts for each current. In Equation (4.16), $F_3 = \frac{V_m}{\sqrt{\pi D}} \frac{1}{F} \frac{dE}{dy}$, and $F_4 = a \cdot S \frac{L}{\nu}$. F_3 and F_4 are similar to functions of F_1 and F_2 as defined in Eq. (15), i.e. $F_3 = ½ F_1$, $F_4 = F_2$. They can be obtained from the relaxation data or from the F_1 and F_2 data from the pulse experiments in the previous section.

In the long time relaxation region, although the mathematical description of the diffusion process may be different, the linear relationships of voltage change with $1/\sqrt{t}$ and with pulse current I and length τ still hold true (see Fig. 4.11). When voltage change becomes small and slow, of particular interest is the estimation of time needed for relaxation to within a certain voltage of OCP when the pulse parameters vary. From the above analysis, in the linear regions we have the relaxation time:

$$t \propto I^2 \cdot \tau^2 \qquad (4.17)$$

Equation (4.17) can be used for estimation of minimum time for a certain voltage relaxation ΔV_r, or most often, for near full relaxation (e.g. within 2 mV of OCP). This simple relationship can be very useful when choosing a standby time for a pulse, or considering trade-offs between operating parameters for different duty cycles.

4.4 Summary

In this chapter, we have examined the transient behavior of a commercial lithium coin cell during pulse discharge and subsequent relaxation as would occur as part of a sensor duty cycle. A quantitative description of the voltage change with time during the pulse and relaxation is provided as part of the study. With EIS experiments, we identified the magnitude of the rapid voltage losses that occur upon initiation and termination of the pulse that are associated with ohmic and interfacial resistances. The EIS results also indicated near-linear behavior of the system over the range of current considered. Solid phase diffusion in the cathode was found to be the major contributor to the "slow" transient voltage change that occurred during and after a pulse. A simple analytical model was developed to describe this time-dependent voltage and the corresponding concentration distribution for a thick porous electrode with a non-uniform current distribution. A fit of the analytical model to experimental data, equivalent to that shown previously in the literature for planar electrodes, permitted an estimate of the solid phase diffusivity. Independent fitting of the pulse data and relaxation data both yielded a diffusivity of $D \sim 4\times10^{-11}$ cm^2/s , which agrees well with measured values for this system [70].

The voltage change with time, both during a pulse and following a pulse, were accurately described by the analytical expressions presented in this paper. Thus, this study provides insight into and a description of the factors that influence and control battery behavior during pulsed cycling. Of particular note is the observation that the time required for relaxation is much longer than the pulse length. Consequently, the relaxation time and its relationship to the desired duty cycle will be a critical factor in determining the suitability of a cell for sustained pulse discharge. The quantitative description of the voltage change with time during the pulse and relaxation provides a convenient and powerful tool for predicting cell voltage for WS duty cycle pulse

operation. It serves as a basis for understanding and optimizing battery performance for sensor duty cycles.

5 EXPERIMENTAL STUDY OF PULSE DISCHARGE CYCLING

5.1 Introduction

In the previous chapter, the transient behavior of a commercial lithium coin cell during pulse discharge and subsequent relaxation as would occur as part of a sensor duty cycle was investigated. This chapter will focus on the performance characteristics of these lithium coin cells during sustained pulse discharge cycling. The transient analysis developed for a single pulse in the previous chapter is used to explain and understand the battery performance during sustained pulse discharge cycling under various conditions. In particular, the goal is to evaluate and understand how the pulse duty cycle characteristics affect 1) the overall battery capacity or lifetime, and 2) the operating cell voltage during the discharge pulse and the subsequent relaxation.

A WS pulse discharge cycle can be defined by the duty cycle parameters, i.e. peak current I_p, standby current I_s, pulse length t_p, standby period t_s. Duty cycle factor (or duty cycle) $\mathcal{D}$, defined as the ratio of the duration of the pulse to the total period of a cycle, i.e. $\mathcal{D} = t_p/(t_s+t_p)$, is a dependent parameter also commonly used to describe the intermittent operation in wireless communication. The duty cycle parameters directly impact the energy consumption profile of a WS. In addition to influencing the overall energy consumption, these parameters determine how the energy is spent (e.g. the amount of energy consumed at the peak current relative to that spent at the standby current to sustain the device). More importantly, as stated in the previous

chapters, the duty cycle parameters may significantly affect the total battery capacity or battery life that can be accessed by the pulse cycling.

The discharge capacity for the battery under a given duty cycle is defined as the value of the capacity at the point when the battery voltage drops below a specified lower limit (i.e. cutoff voltage). For a WS system, this limit will be reached during a discharge pulse, which is the portion of the duty cycle where the voltage is lowest. This is different than what would be seen during a continuous galvanostatic discharge. For the pulse cycling of WSs, attention needs to be paid to both the overall energy consumption and the pulse power profile. While we expect these duty cycle parameters to impact the battery behavior, it is not known how and to what extent they affect the battery capacity and the resulting energy consumption profile. For example, an interesting situation is that different combinations of these parameters may lead to the same overall energy consumption. In this case the capacity results and its correlation to the parameters may be very useful for system optimization. Another important question is how to maximize the battery capacity by adjusting the duty cycle factor when the peak and standby power are fixed, which is often encountered in WS system operation.

In this chapter we present a systematic experimental study that addresses these questions. The influence of these duty cycle parameters on battery capacity and operating voltage is studied, and an analysis of voltage changes associated with the various pulse discharge conditions is provided. A key objective of the work is to provide a quantitative basis for the selection of WS design parameters to maximize battery efficiency.

5.2 Experimental

The rechargeable ML1220 coin-type cells (from Panasonic) studied in the previous chapter were used in this investigation. The open circuit voltage of ML 1220 cells as shipped is about 2.7 V. The cells were first discharged to 2.0 V at 0.05 mA, and then charged to 3.1 V before testing. After this initial discharge-charge cycle, a duty cycle test consisting of 0.1 s, 10 mA pulses separated by 2 s, 25 μA standby periods was performed until the battery reached a cutoff voltage of 2.0 V. This duty cycle test was used to characterize the cell internal resistance and pre-screen the batteries. The total capacity (or the total number of pulse cycles) obtained prior to reaching the cutoff voltage was used as a principal indicator for evaluating cell performance. The observed cell-to-cell variation was generally within 3%, suggesting excellent consistency among the coin cells. The very few cells that exhibited higher deviation in this initial screening test were not used in the experiments. After this initial pulse cycling, (and after each individual pulse cycling test), the battery was charged to 3.1 V by a two-step charging procedure, which was introduced in chapter 4.

The pulse discharge tests were designed so that the impact of each operating parameter (i.e. peak current I_p, standby current I_s, pulse length t_p, standby period t_s) could be evaluated. The testing conditions for evaluating these parameters are shown in Table 5.1. Each test used a minimum of two cells, and additional repeats or additional cells were used if the observed deviation for the original two cells exceeded 5%. The experimental results showed excellent consistency due to the prescreening tests and the relatively small cell-to-cell variation of the commercial cells.

Table 5.1 Pulse discharge performance test table

	Standby current (μA)	Standby time (s)	Pulse current (mA)	Pulse length (s)	Duty cycle (%)
Standby Current	0 / 25 / 50 / 100	2	10	0.1	5
Standby time	25	0.5 / 1 / 2 / 5 10 / 20 / 50 / 100	10	0.1	17 / 9 / 5 / 2 1 / 0.5 / 0.2 / 0.1
Pulse current	25	2	5 / 7.5 / 10 / 12.5 / 15	0.1	5
Pulse length	25	0.25 / 0.5 / 1 / 2 5 / 10 / 20	10	0.05	17 / 9 / 5 / 2 1 / 0.5 / 0.2
	25	1 / 2 / 4 / 5 10 / 20 / 40 / 80	10	0.2	17 / 9 / 5 / 4 2 / 1 / 0.5 / 0.2
	25	1 / 2 / 4 / 5 / 8 / 10 20 / 40 / 80 / 160	10	0.4	29 / 17 / 9 / 7 / 5 / 4 2 / 1 / 0.5 / 0.2

Because the ML1220 cells exhibited good cycle life for incomplete discharge (e.g. >100 cycles at 50% DOD [43]), which is expected for WS pulse cycling, most cells were reused several times after charging for different pulse cycling tests. The same duty cycle test (10 mA, 0.1 s pulses and 25 μA, 2 s standby) as used for the initial screening was performed after the cells finished a series of pulse cycling tests, to examine the cell condition change or cell fading. The very few cells that exhibited variation larger than 5% were discarded and the tests were repeated with other cells. It was found that the total capacity obtained before and after the pulse cycling tests changed very little, mostly within 3%, and thus the effects of testing order or cell fading on the cell performance were negligible for this study.

5.3 Results and discussion

Figure 5.1 shows the voltage profile of a ML1220 cell that was pulse discharged with 10 mA, 0.1 s pulses and 25 μA, 50 s standby until the cutoff voltage (2.0 V) was reached. A total of 12,100 pulse cycles was obtained and, since data were collected every 100 cycles, 121 cycles are shown in Fig.5.1. The overall capacity extracted from the battery was ~15 mAh, which was 88% of the 17 mAh capacity rated at 30 μA. This duty cycling increased the capacity of the battery by a factor of 20 over the capacity observed at the 10 mA rate under constant discharge conditions (see Fig. 4.1 or Fig. 5.2).

The operating voltage of the pulse cycling varied between an upper and a lower voltage, where the upper voltage was the highest voltage reached during standby and the lower voltage was the lowest voltage during a pulse. The upper voltage for a pulse discharge is determined by the voltage at the end of the standby period, for which two relationships need to be considered. The first is the voltage relaxation with time, which was discussed in detail in the previous chapter. The second is the average current of a pulse discharge, which can be expressed as

$$I_{ave} = \frac{I_p t_p + I_s t_s}{t_p + t_s} \tag{5.1}$$

For a single pulse initiated at OCP, or for pulse cycles that allow full relaxation between the pulses, the relationship from the previous chapter (Eq. 4.14) can be used to describe the voltage relaxation between the pulses. For pulse cycles that only allow partial relaxation between the pulses, a concentration gradient is left unrelaxed in the solid material that increases with pulse cycling. This “background” concentration gradient is very likely related to the average mass transfer rate of the lithium ion, which can be expressed by the time average current. Physically, the exhibited cell voltage is associated with the lithium concentration at the surface of the solid intercalation material. During sustained pulse cycling, the upper voltage is the result of both this “background” concentration gradient and the relaxation of the concentration gradient caused by the pulse discharge right before a standby period.

The voltage profiles of the ML1220 cells during galvanostatic discharge at different rates are shown in Fig. 5.2. The upper voltage during the pulse cycling will be compared with the OCP or the discharge voltage profile at the rate of the average current of the pulse operation in the following sections. In Fig. 5.1 we can see that the upper voltage aligned well with the 25 μA discharge curve, which approximates the OCV profile of the cell, indicating full relaxation between the pulses.

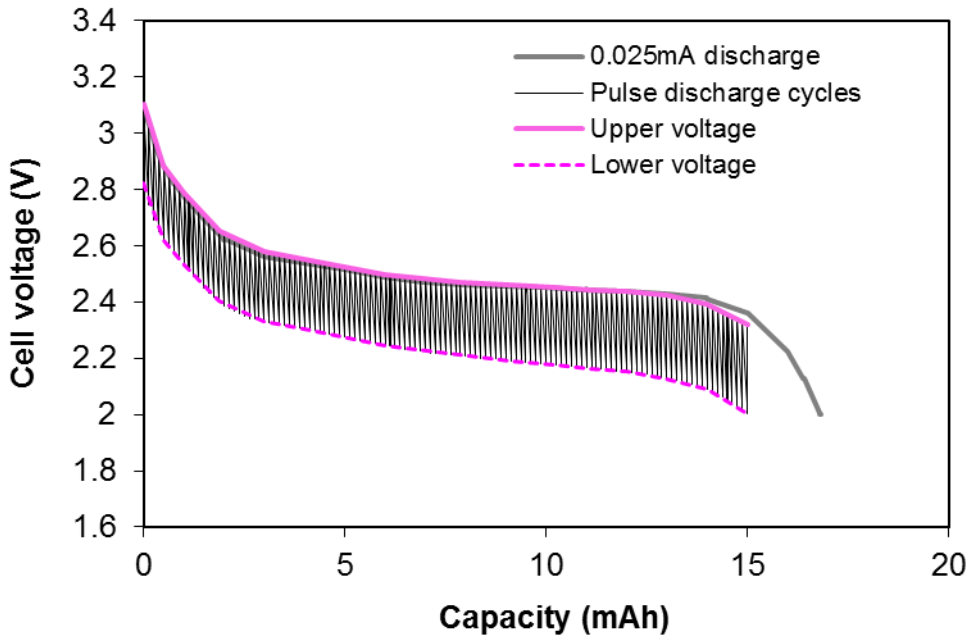

Figure 5.1 Pulse discharge of ML 1220 cells using a duty cycle with 10 mA, 0.1 s pulses and 25 µA 50 s standby.

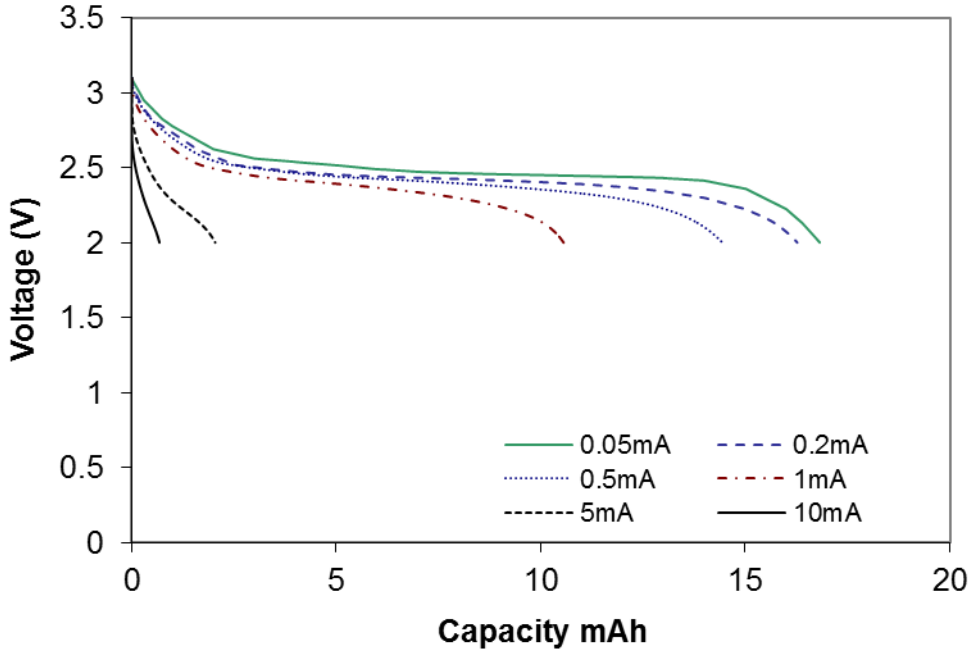

Figure 5.2 Voltage profiles of ML1220 cells during galvanostatic discharge at different discharge rates.

The lower voltage reflects the drop in voltage from the upper voltage that occurs during sustained pulse discharge. Fig. 5.3 (a) shows a few pulse discharge profiles at different capacities (subset of Fig. 5.1); the voltage change that resulted from each these pulses is shown in Fig. 5.3(b). The insert in Fig. 5.3 (a) shows an example of a detailed voltage profile for a pulse where the fast voltage change dV1 and the slower voltage change dV2 are illustrated. The total voltage loss, dV total, is the sum of dV1 and dV2, which is equal to the difference between the upper and lower voltage at a certain state-of–charge (SOC). The fast voltage drop dV1 is due mainly to the ohmic and kinetic resistances of the cell, and changes linearly with the applied pulse current. It is a large fraction of the total overpotential for the short pulses considered in this study and does not depend on the length of the pulse. In contrast, dV2, the voltage loss due to transport limitations in the cathode active particles, is a function of both the pulse current and pulse length.

In Fig. 5.3 (b), both dV1 and dV2 follow a similar trend vs. capacity (or SOC), where they are high at the beginning and towards the end, with a minimum around 2-5 mAh (70-90% SOC). This observation corresponds well with results in literature [78]. The change of dV1 is probably due to penetration of the reaction zone (see previous chapter) more deeply into the electrode with time as the cell is discharged, which affects the ohmic resistance. The change in dV2 reflects the changes in F1 and F2 as a function of SOC (see Eq. 4.14).

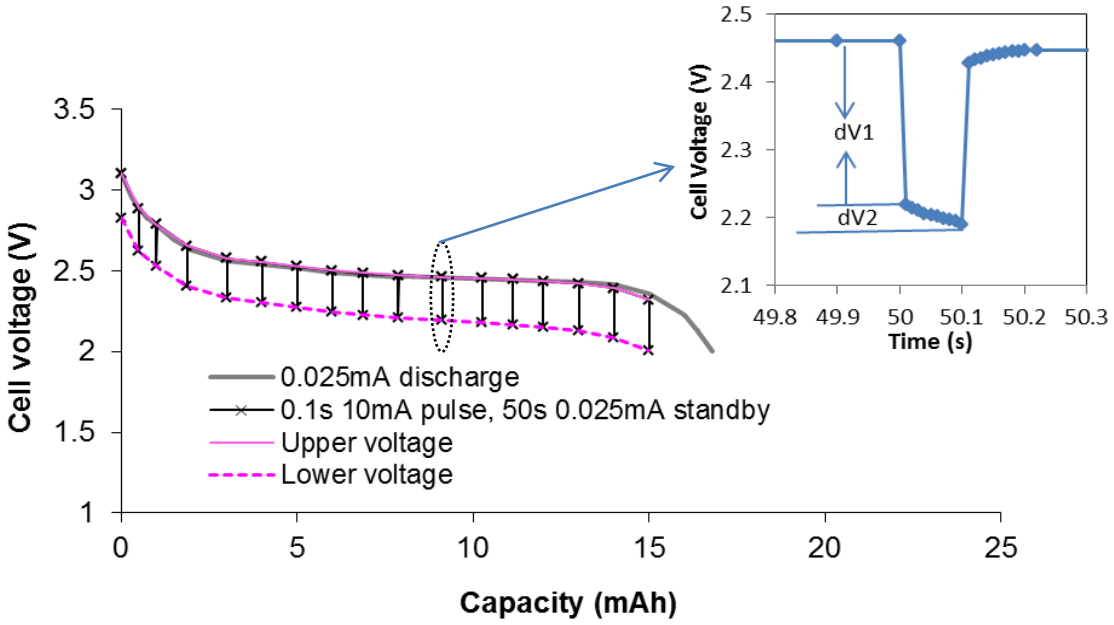

(a)

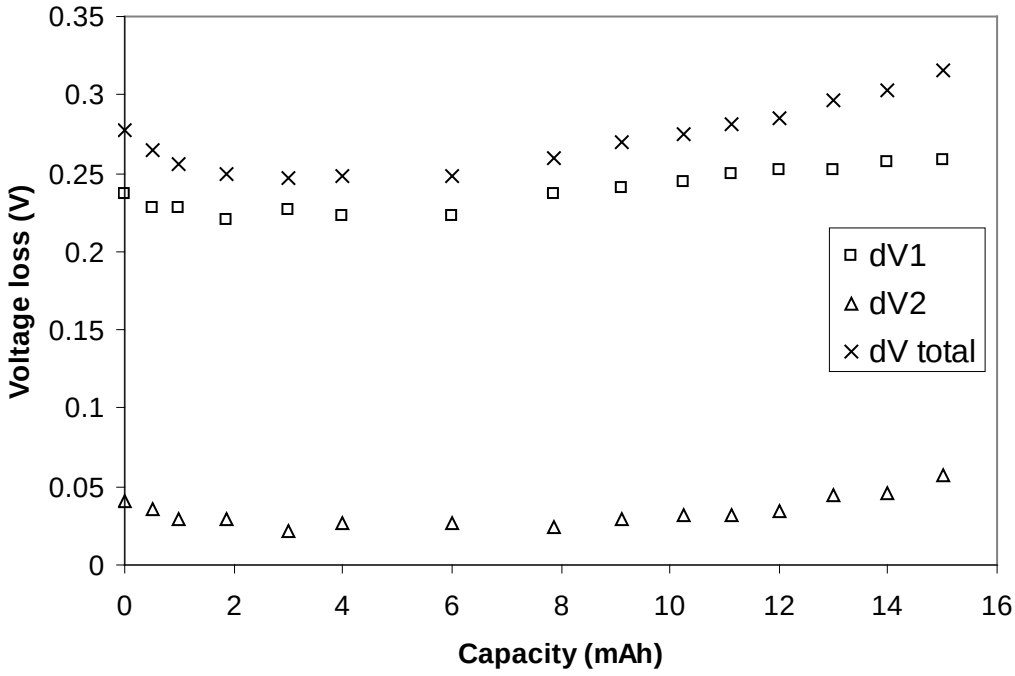

(b)

Figure 5.3 Selected discharge voltage profiles (a) and voltage losses (b) at different state-of–charge of the pulse cycling shown in Fig. 5.1.

In Fig. 5.1 and 5.3, we showed an example of pulse cycling and the accompanying voltage losses analysis for a standby time that permitted full relaxation (or nearly so) between the pulses. Understanding the voltage change with duty cycle characteristics is vital for battery operating life prediction. To this end, we carried out extensive studies under various pulse cycling conditions, and the results are presented in the following sections in terms of each of the duty cycle parameters. The impact of the time average current on upper voltage and capacity is also provided.

5.3.1 Impact of standby current

The standby current of a WS system is determined by the total power consumption of the electronics in sleep mode. The impact of standby current on the battery capacity and operating voltage of the cell is shown in Fig. 5.4. The duty cycle consisted of 10 mA, 0.1 s pulses followed by a 2 s standby period at a current of 0, 25, 50 or 100 μA. The total capacity was the same for standby current of 0 and 25 μA. It decreased when the standby current increased from 0 to 50 μA (by 3%) and to 100 μA (by 7%). Changes in both the upper and lower voltages affect the total capacity that can be accessed. We can see from Fig. 5.4 (b) that the voltage profiles did not vary significantly as a function of standby current, especially for standby currents lower than 50 μA. In fact, the voltage profiles for standby current of 0 and 25 μA were nearly identical.

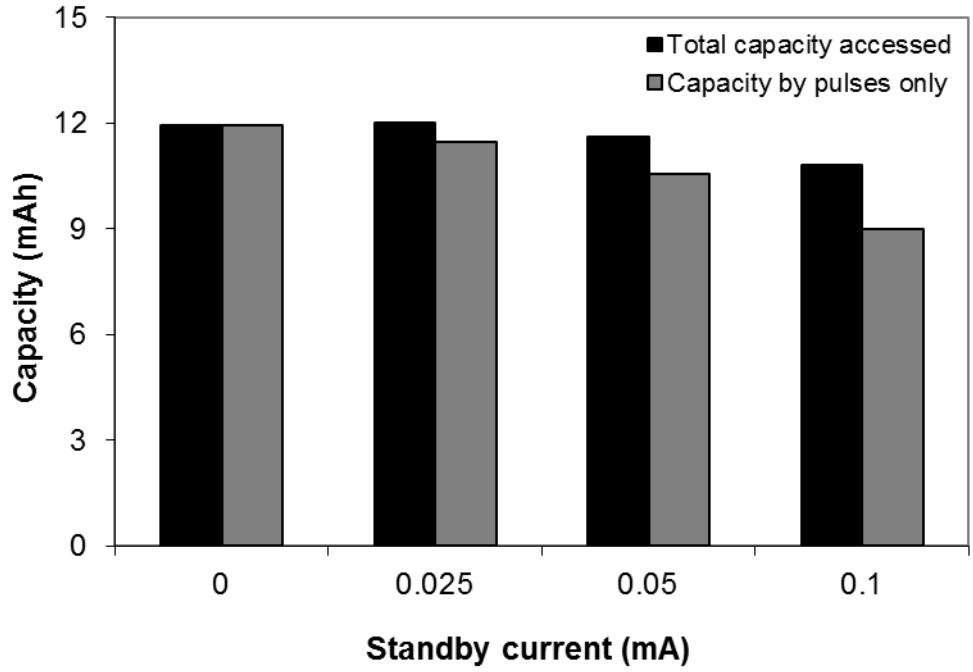

(a)

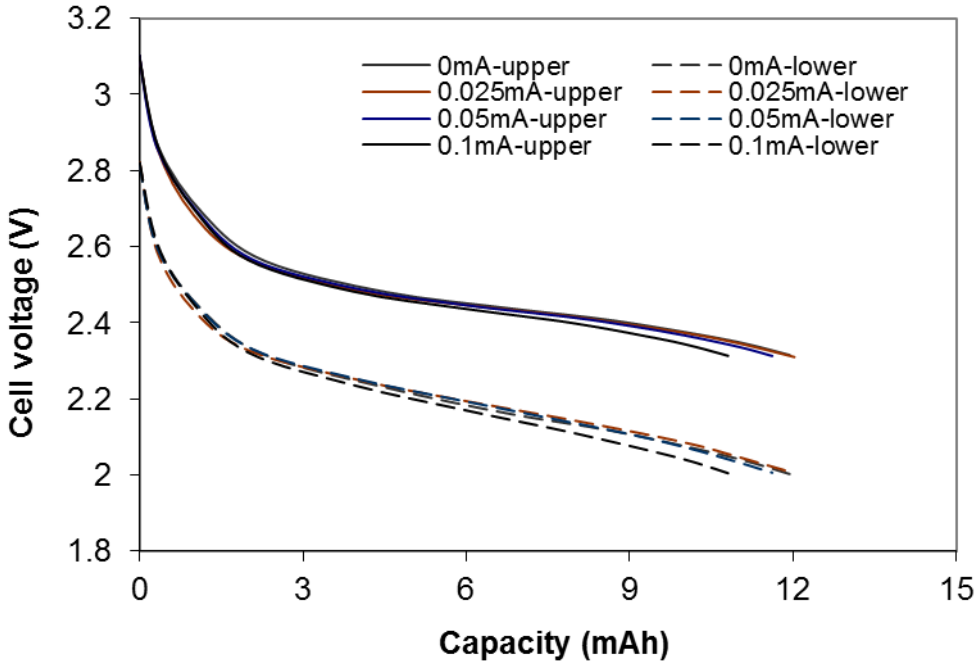

(b)

Figure 5.4 Impact of standby current on battery capacity (a) and cell operating voltage (b). Duty cycle parameters: I_p=10 mA, t_p,=0.1 s, t_s=2 s, I_s=0-100 μA.

The voltage relaxation is essentially a relaxation of the concentration gradient in the cathode active material that builds up during pulse discharge. The magnitude of the current pulse (10 mA) is 100-400 times that of the standby current (100-25 μA); hence the influence of the standby current on the voltage relaxation after the pulse is small. In addition, for ML1220 cells, the voltage profiles measured for galvanostatic discharge at rates of 25 and 50 μA (corresponding to C-rates of 0.0015-0.003) were very similar, and were used to approximate the open circuit voltage of the cell in this study. For this reason, the voltage analysis for relaxation at zero current can be used for relaxation at low currents (≤50 μA) without introducing significant error. In this work, standby current of 25 μA was used unless otherwise stated.

Mathematically, the total capacity C_{tot} is equal to the product of the capacity per pulse cycle and the total number of cycles:

$$C_{tot} = (I_p t_p + I_s t_s) \cdot N \qquad (5.2)$$

Both the pulse and the standby power impact the total energy consumption. The percentage of capacity delivered at the peak current in the form of pulses can be calculated through:

$$\theta_p = \frac{I_p t_p}{I_p t_p + I_s t_s} = \frac{I_p \mathscr{D}}{I_p \mathscr{D} + I_s (1 - \mathscr{D})} \qquad (5.3)$$

Clearly θ_p decreases as the standby current increases. The capacity delivered by the pulses only C_{pul} can be obtained from C_{tot} θ_p. In Figure 5.4 (a), the capacity C_{pul} decreased as the standby current increased, reflecting the change of both C_{tot} and θ_p with standby current. During WS operation, the amount of capacity delivered by the peak current is directly related to the amount of data transferred during the pulses. It is an important factor to consider and may be of great interest for system optimization in terms of data transfer.

5.3.2 Impact of standby time

The impact of standby time on the battery capacity and operating voltage is shown in Fig. 5.5. The duty cycle factor $\mathcal{D}$ ranges from 0.2% (standby time 50 s) to 17% (0.5 s). The total capacity increased when the standby time increased, but when the standby time was greater than 10 s, the change of total capacity was minimal. A pulse-relaxation transient analysis of the 10 mA 0.1 s pulse (see the previous paper chapter) shows that at relaxation times of 0.5 s and 2 s, the cell is about 11 mV and 5 mV lower than the OCP (3.1 V), which implied only a partial relaxation between the pulses. At 10 s, the voltage is relaxed to within 1 mV of the equilibrium voltage, and there is little voltage change when the standby time is increased further. This corresponds well with the capacity and voltage results shown here.

In fact the upper and lower voltage profiles for standby times of 10, 15, 20 and 50 s were essentially identical, and data for t_s=20 s is shown as an example of these long standby times in Fig. 5.5 (c). In situations where standby time is sufficiently long for complete relaxation, the lower voltages were a function of pulse current and length only, and were not affected by the standby time. The upper voltage is the highest voltage recovered during the standby period, which equal to the OCP at a given SOC for full relaxation (since the standby current is low I_s=25 μA). Therefore the upper voltage profiles for standby time of 10, 15, 20 and 50 s were the same and all follow the OCP curve of the cell. When the standby time only allows for incomplete relaxation, both the upper and lower voltages shifted downwards, the cutoff voltage was reached sooner and a lower fraction of the battery capacity was utilized.

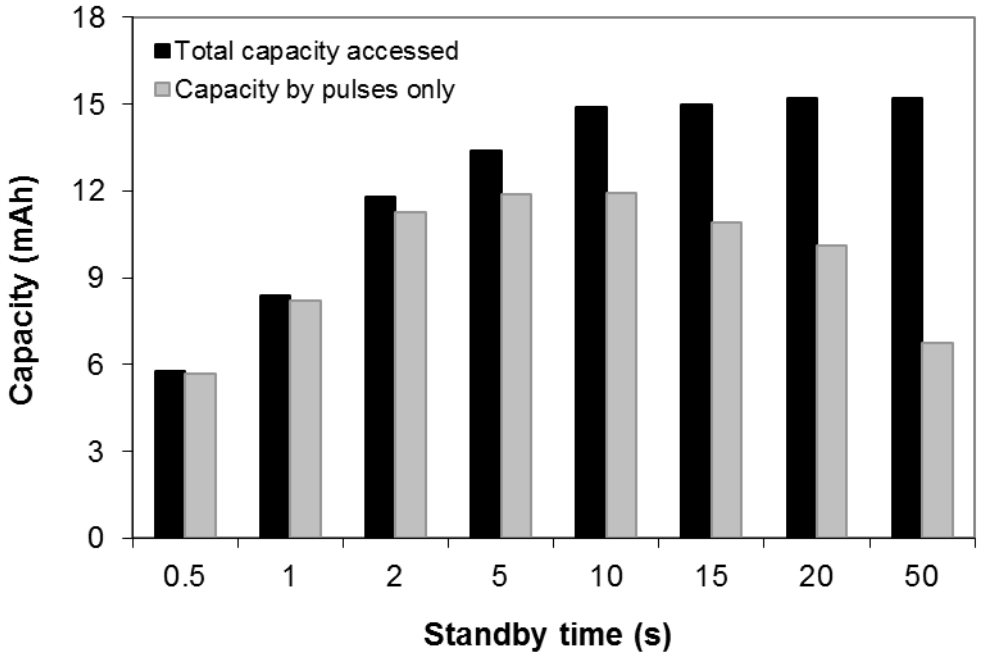
Total capacity accessed
Capacity by pulses only
Capacity (mAh)
18
15
12
9
6
3
0
0.5
1
2
5
10
15
20
50
Standby time (s)

(a)

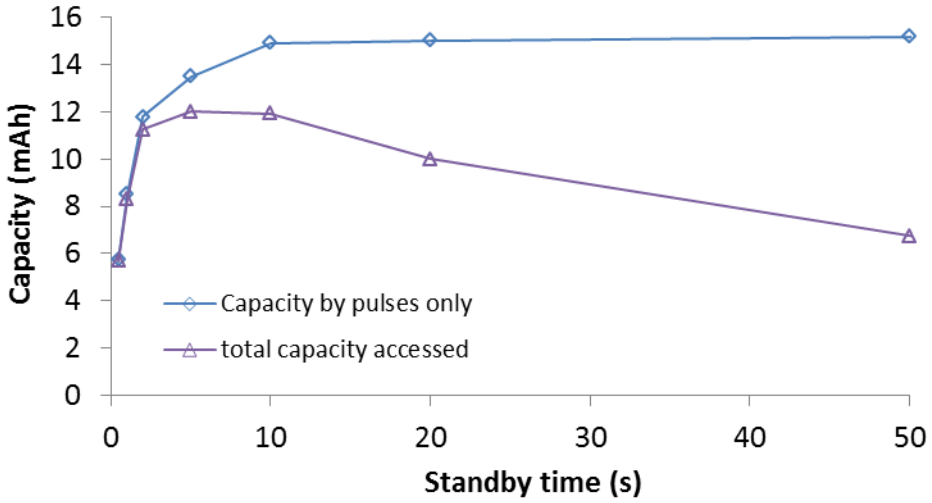
Capacity (mAh)
16
14
12
10
8
6
4
2
0
Capacity by pulses only
total capacity accessed
0
10
20
30
40
50
Standby time (s)

(b)

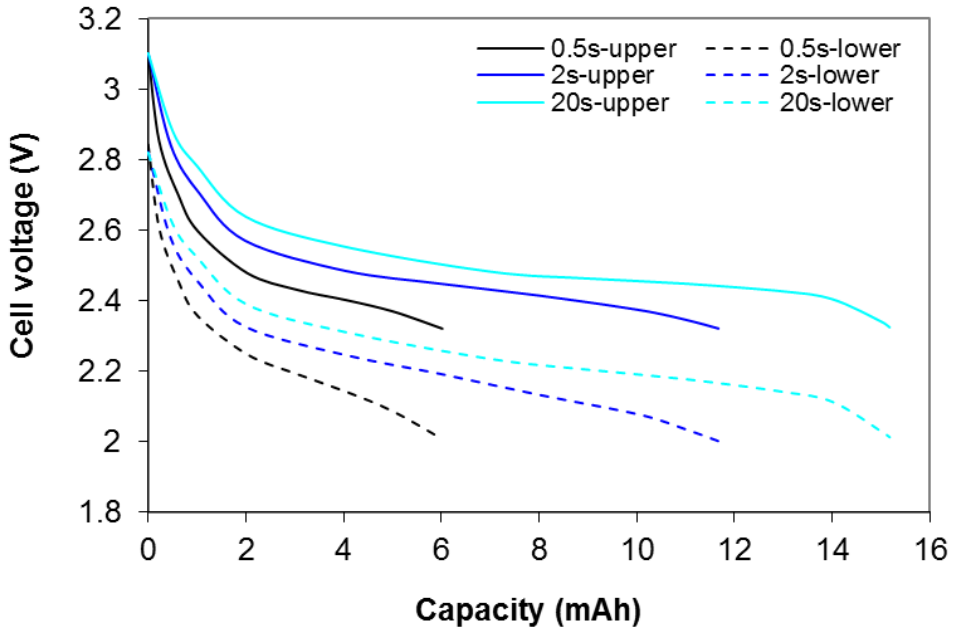

(c)

Figure 5.5 Impact of standby time of pulse discharge on battery capacity (a) and operating voltage (c). In (b) a linear scale of standby time is used. Duty cycle parameters: I_p=10 mA, t_p=0.1 s, I_s=25 μA, t_s=0.5-50 s.

When the standby time is sufficiently long for near complete relaxation of the voltage, the total capacity remains constant; additional increases in the standby time result in fewer pulses per time and, consequently, a lower fraction of the total power delivered at the pulse current (also see Equation 5.2). In Fig. 5.5(a) and (b), the percentage of capacity delivered by the pulses θ_p ranges from 99% (0.5 s) to 44% (50 s standby time). The maximum capacity delivered at the peak current occurs around t_s=5 s when $\mathcal{D}$=2%. If the WS needs to be optimized for the amount of data transferred operating by a cell, then this should be the optimal point. There are other system optimization goals that can be met by adjusting the standby time. For example, if the WS operation needs to be optimized for both the amount of data and the rate of data transfer, (that is,

the highest battery capacity and at the same time the highest possible sampling rate is needed), a standby time of t_s=2 s should be a good option. At t_s=10 s, the system can transfer a largest amount of data while the operating lifetime of the device based on the wall clock is optimized.

The upper voltage is measured at a low rate standby current (25 μA), and is a more accurate description of the local surface concentration of the electrode. To provide an easy way to understand this, we note that the local concentration in the electrode, especially the surface composition of the cathode active material, is similar when the battery is relaxed to a similar voltage. Therefore, use of the upper voltage as the starting point allows us to compare the voltage losses from a similar initial value. As shown in Fig. 5.6 (b), the voltage loss versus the upper voltage follows the same trend for the different standby times used. The results for 2 s and 20 s are close to each other, while voltage loss for 0.5 s is slightly lower than the other two, especially at low voltages near the end of discharge.

When the voltage loss elements dV1 and dV2 of the pulses in Fig. 5.6 were further analyzed, we found that dV1, the instant voltage loss, changed little with standby time, while dV2, the voltage loss due to solid diffusion effects, was obviously lower for the 0.5 s than the 2 s standby. We note that the average current was I_{ave}= 0.5 mA when t_s=2 s and I_{ave}=1.69 mA when, t_s=0.5 s. At higher average currents, there is a higher "background" concentration gradient, which will yield a lower upper voltage for a given state-of-charge (capacity). Also, the 0.5 s standby time was not sufficient to relax the concentration gradient, which would contribute to the observed behavior.

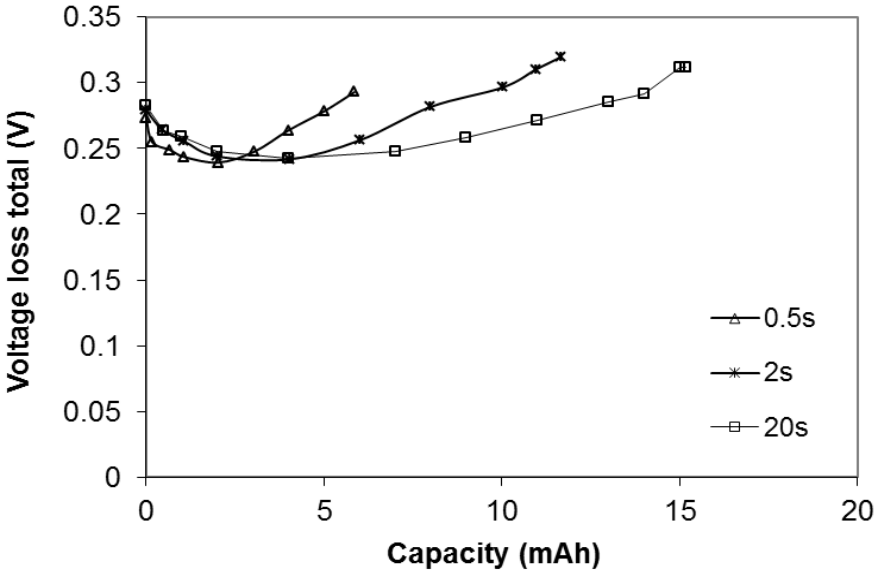

(a)

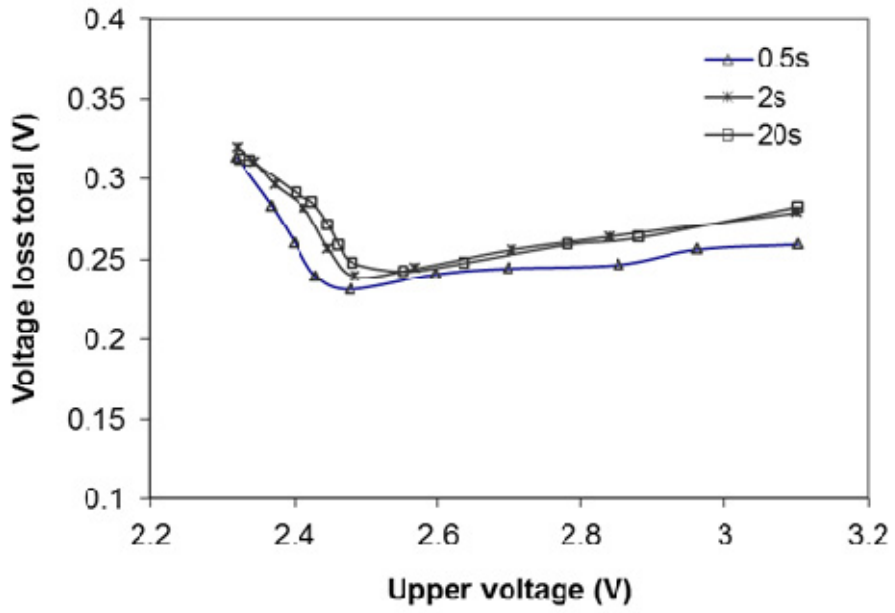

(b)

Figure 5.6 Total voltage loss of pulse discharge with 0.5 s, 2 s and 20 s standby time against capacity (a), and against upper voltage (b).

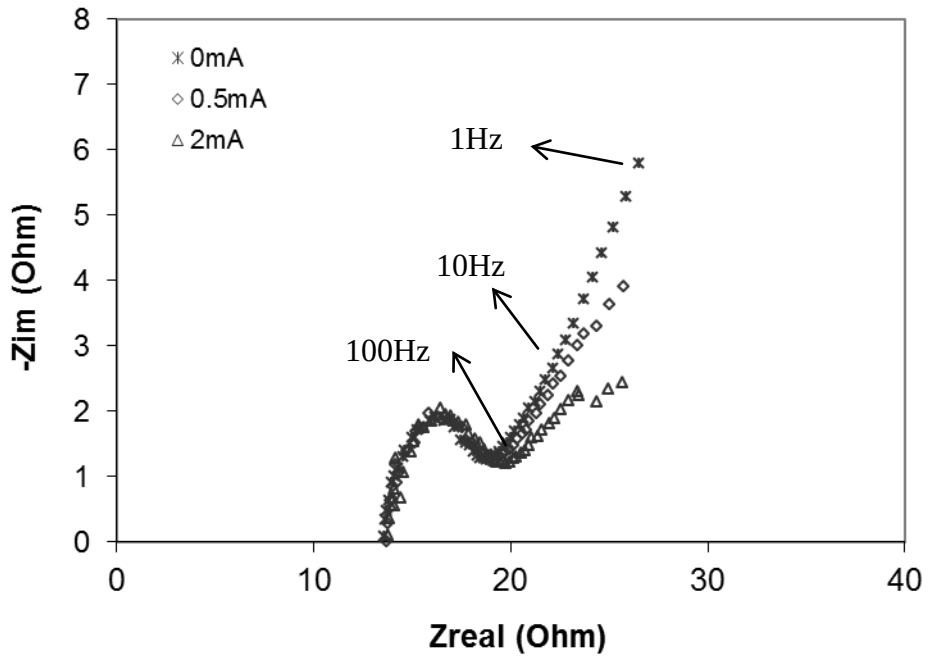

Figure 5.7 Nyquist plot of EIS experiment with DC current of 0, 0.5 mA and 2 mA (frequency 1 to 100,000) and a 25 μA sinusoidal AC current.

As discussed in the previous chapter, the voltage loss dV2 is primarily caused by the lithium composition change at the surface of the active material particle, which can be lowered if the ion transport is faster in the particle. To verify this, an EIS experiment was performed on a cell with a 25 μA sinusoidal perturbation current, to which a DC background current of 0, 0.5 and 2 mA is applied. The result is shown in Fig. 5.7. It can be seen that the ohmic and kinetic resistances at high frequencies were barely changed by the DC current, which is consistent with the result that dV1 did not vary significantly with the standby current. At low frequencies, the Warburg segment of the 0.5 mA and 2 mA curves was lowered from the one with zero background current. At AC frenquency f =1-10, the difference in the Warburg impedance for the 0 mA and 0.5 mA data was relatively small, which explains the similarity of voltage losses for

the 2 s and 20 s curves in Fig. 5.6 (b). However, the diffusion impedance was appreciably lower when the background current was increased to 2 mA, which again confirms our explanation.

5.3.3 Impact of pulse current

The pulse current is associated with the transmission power level of the radio used in a wireless sensor, which also affects the transmission distance. The impact of pulse current on the battery capacity and operating voltage is shown in Fig. 5.8. The capacities, both the total capacity and the capacity by pulses only ($C_{pul} = C_{tot}\theta_p$), decreased as the pulse current increased. Although θ_p increases as the pulse current increases (see Equation 5.2), the resulting capacity C_{pul} was dominated by the change of the total capacity with the pulse current.

Pulse current affects both the lower and upper voltage during operation. In Fig. 5.8 (b), we can see that the variation in upper voltage was small. Although the extent of voltage relaxation at a certain standby time decreases as the pulse current increases, the 2 s standby time used allowed for more than 80% of the voltage relaxation between these pulses, and the variation in pulse current only caused a small difference in the transient voltage at the end of the 2 s standby period. The range of the average current for these pulses was small, varying from 0.26 mA (for 5 mA pulse) to 0.74 mA (for 15 mA pulse).

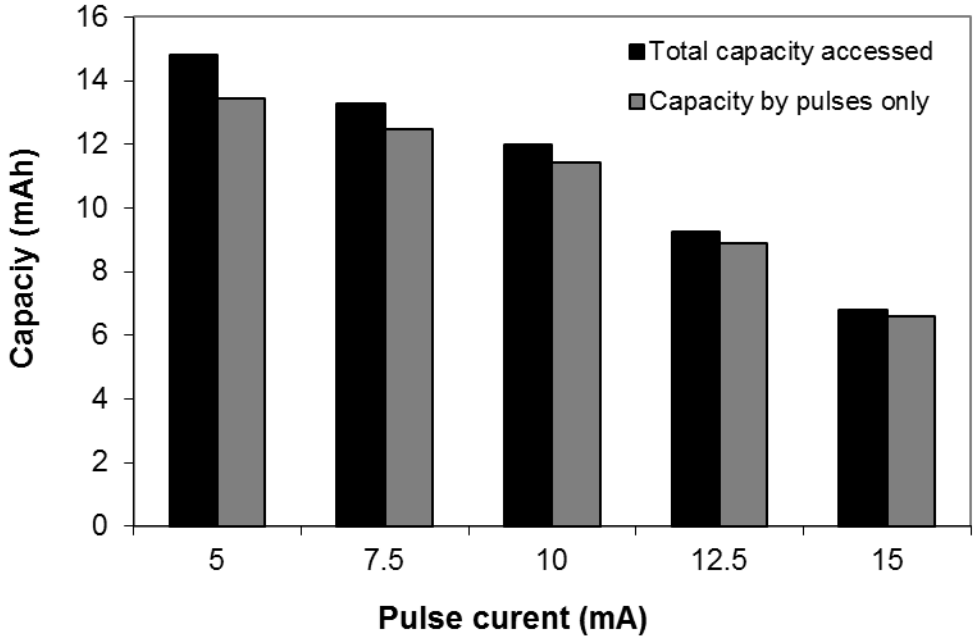

(a)

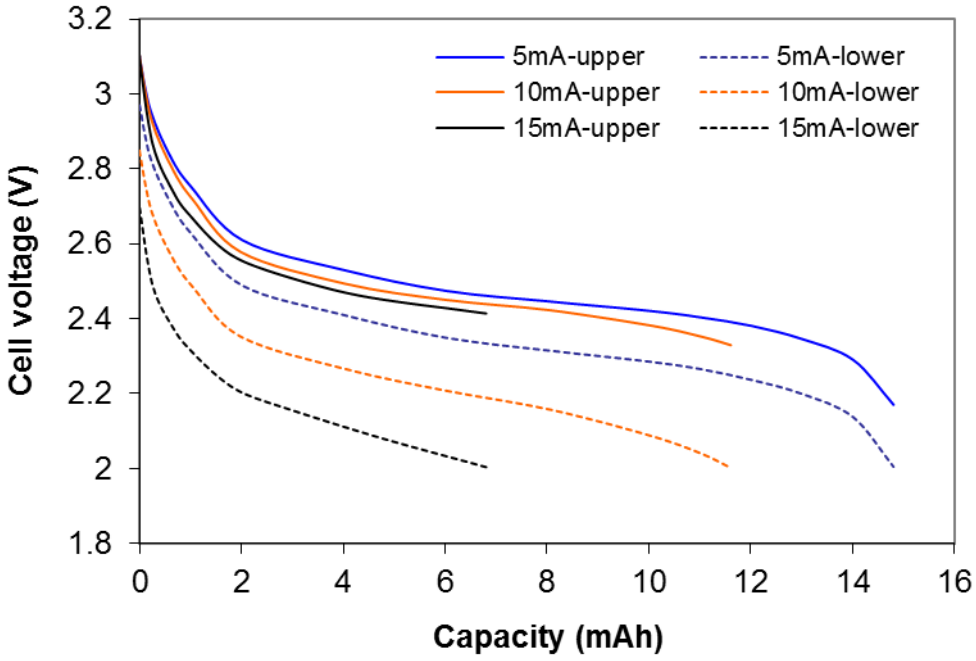

(b)

Figure 5.8 Impact of pulse current on battery capacity (a) and cell operating voltage (b). Duty cycle parameters: I_s=25 µA, t_s=2 s, t_p=0.1 s, I_p=5-15 mA.

The lower voltage, however, changed significantly with the pulse current. In the previous chapter, we established that both the fast voltage change dV1 and the slower voltage change dV2 change linearly with the pulse current applied. The total voltage loss for pulses of 5 mA, 10 mA and 15 mA vs. the upper voltage is shown in Fig. 5.9. It can be seen that the ratio of the voltage losses corresponds with the ratio of the pulse currents. The average operating voltage for a pulse, defined as the mid-point voltage between the upper and lower voltage, is about 100-150 mV lower when current is increased by 5 mA. It is worth mentioning that in the selection of pulse current, failure to consider this change of voltage loss with current may cause misleading results. For example, when keeping t_p and I_s constant, increasing pulse current from 10 mA to 30 mA while extending the standby time from 2 s to 6 s does not change the time-averaged current. However, while the total capacity achieved from the 0.1 s, 10 mA pulse was about 12 mAh, the capacity of the 30 mA pulse was almost zero, because the voltage loss was so high that it reached the cutoff voltage in the initial few pulse cycles.

The pulse current probably has the most significant influence on battery performance in that it determines the maximum capacity that can be extracted from a battery for a pulse discharge cycling. For a certain pulse current and length selected, the battery capacity can be maximized when full relaxation is achieved between the pulses by adjusting the standby time used (see section 3.2). This maximum capacity is determined when the cutoff voltage (2.0 V in this study) is reached during a discharge pulse, which depends on the lower voltage profile of the pulse cycles. The pulse current has a significant impact on the lower voltage, and thus has a significant impact on the battery capacity. For example, while a maximum capacity of 15 mAh was obtained for 10 mA 0.1 s pulses with a standby time of 10 s or longer, the maximum capacity that can be obtained for 20 mA 0.1 s pulses was less than 5 mAh with a standby time of

40 s or so. For ML1220 cells, a pulse current no greater than 15 mA is recommended, so that a capacity of more than 50% of the rated capacity can be achieved.

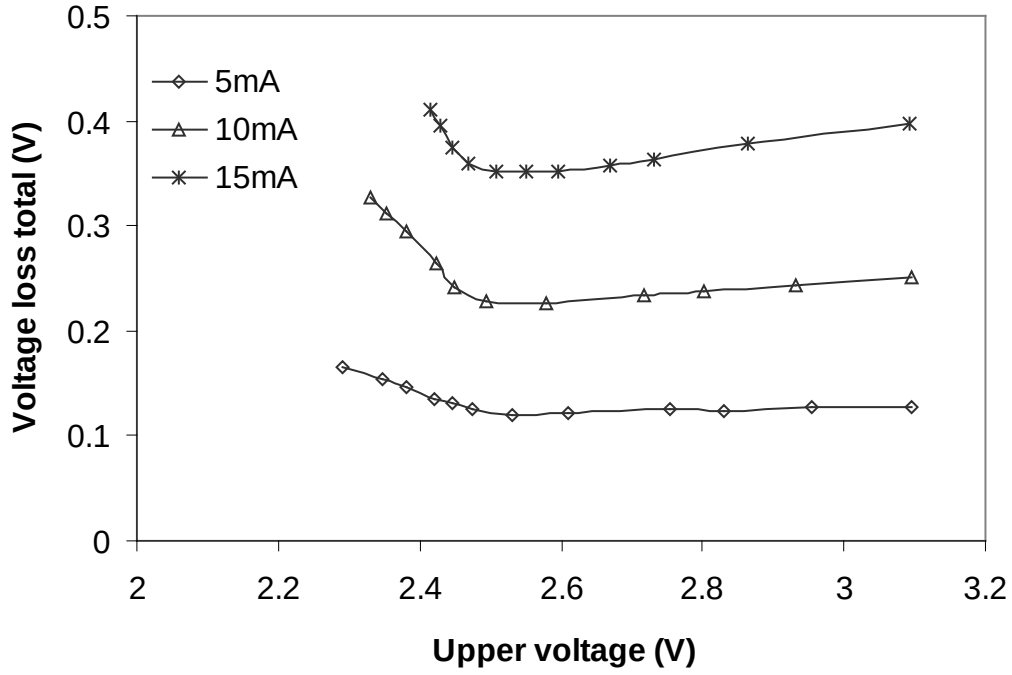

Figure 5.9 Total voltage loss of pulse discharge with 5 mA, 10 mA and 15 mA pulse current

5.3.4 Impact of pulse length

The impact of pulse length on battery capacity was quite different when the extent of relaxation between the pulses was different. In Fig. 5.5, we present the results of 0.05 s, 0.1 s, 0.2 s and 0.4 s pulses with a standby time of 2 s as an example. The capacities, both the total capacity and the capacity by pulses only ($C_{pul} = C_{tot}\theta_p$), decreased as the pulse length increased. The average current for the 0.05, 0.1, 0.2 and 0.4 s pulses were 0.27, 0.5, 0.93 and 1.7 mA respectively, and thus we see a significant variation in the upper voltage profiles.

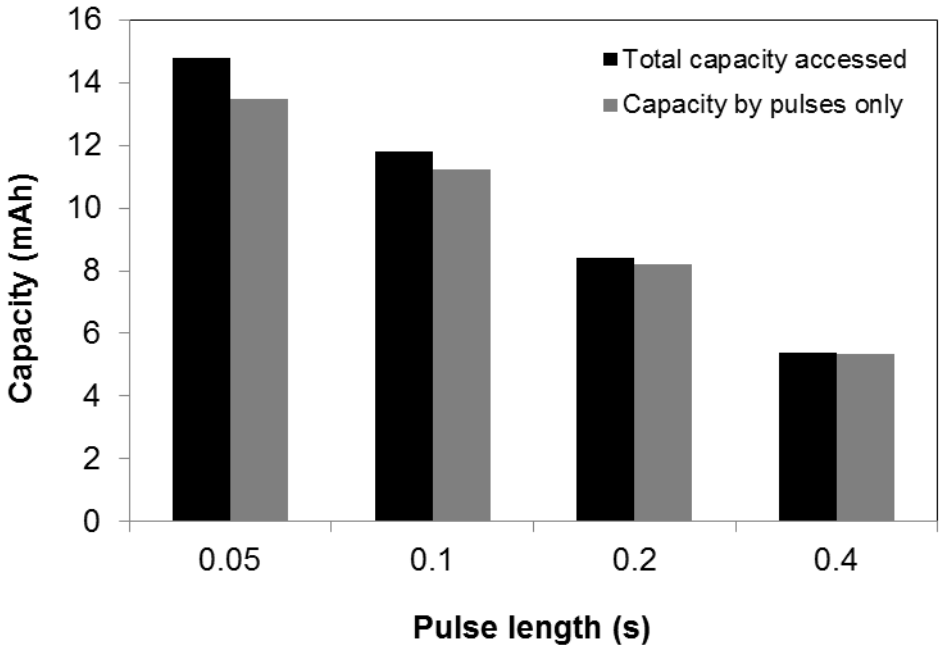

(a)

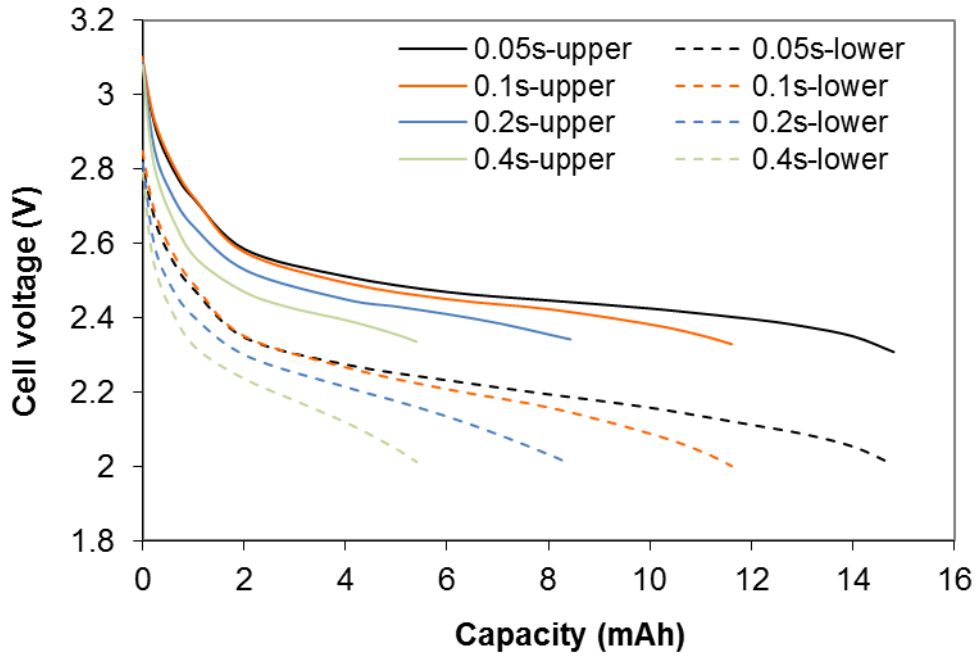

(b)

Figure 5.10 Impact of pulse length on battery capacity (a) and cell operating voltage (b). Duty cycle parameters: I_p=10 mA, t_p=0.05-0.4 s, I_s=25 μA, t_s=2 s.

The lower voltage shifted downwards because the voltage change dV2 increases with the square root of the pulse length. The total voltage loss for pulses presented in Fig. 5.10 is shown in Fig. 5.11. Again, we can see that, although the capacity from these duty cycles varied over a big range, the voltage losses followed the same trend vs. upper voltage as shown in the above sections. Over the majority of the voltage range, the voltage loss is the highest for the longest pulse length. The variation in voltage loss became smaller as the pulse cycling approached the end of the discharge.

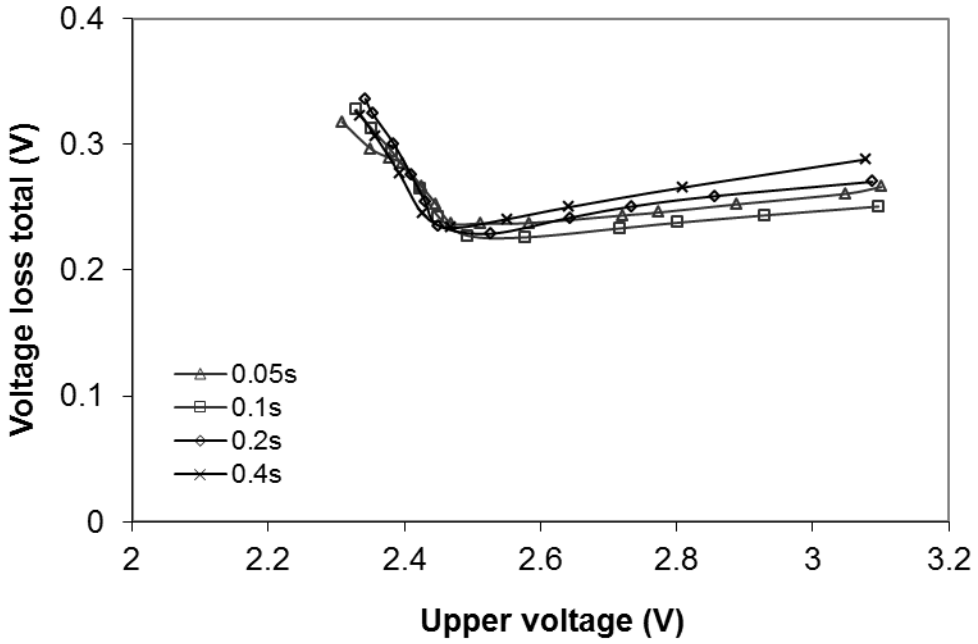

Figure 5.11 Total voltage loss of pulse discharge with pulse length of 0.05, 0.1, 0.2 and 0.4 s.

We investigated the battery performance over a broad range of standby times for each pulse length, and the capacity results are presented in Fig. 5.12 in terms of standby time t_s, ratio of standby time to pulse length t_s/t_p, and ratio of standby time to pulse length t_s/t_p^2. The standby times tested for each pulse length are summarized in Table 5.2, and the calculated t_s/t_p and t_s/t_p^2

values are listed in the table as well. These three factors are of interest here because: 1) standby time is one of the duty cycle parameters to describe a pulse discharge; 2) t_s/t_p is mathematically associated with the duty cycle factor $\mathcal{D}$ and the average current I_{ave}; 3) the voltage relaxation process after a pulse is best described by t_s/t_p^2 as discussed in the previous chapter.

Because duty cycle factor $\mathcal{D}$ can be expressed as

$$\mathcal{D} = \frac{t_p}{t_p + t_s} = \frac{1}{1 + t_s / t_p} \tag{5.4}$$

the average current I_{ave} can be expressed in terms of t_s/t_p and $\mathcal{D}$ as

$$I_{ave} = \frac{I_p + I_s \cdot t_s / t_p}{1 + t_s / t_p} = I_p \mathcal{D} + I_s (1 - \mathcal{D}) \tag{5.5}$$

Therefore, the average current I_{ave} or the duty cycle $\mathcal{D}$ does not change when varying the pulse length and the standby time if t_s/t_p is kept constant.

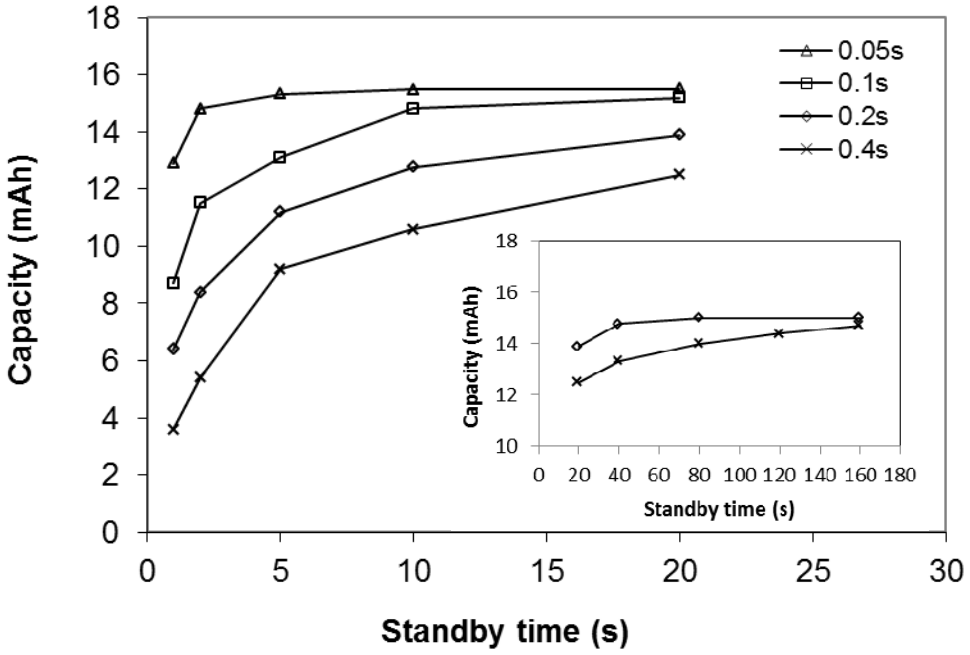

(a)

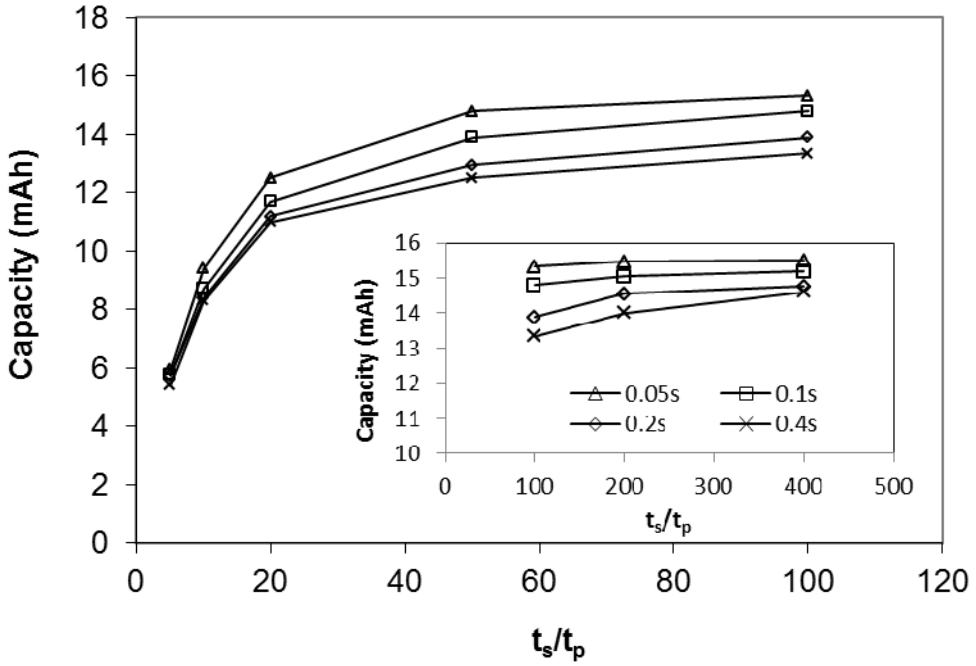

(b)

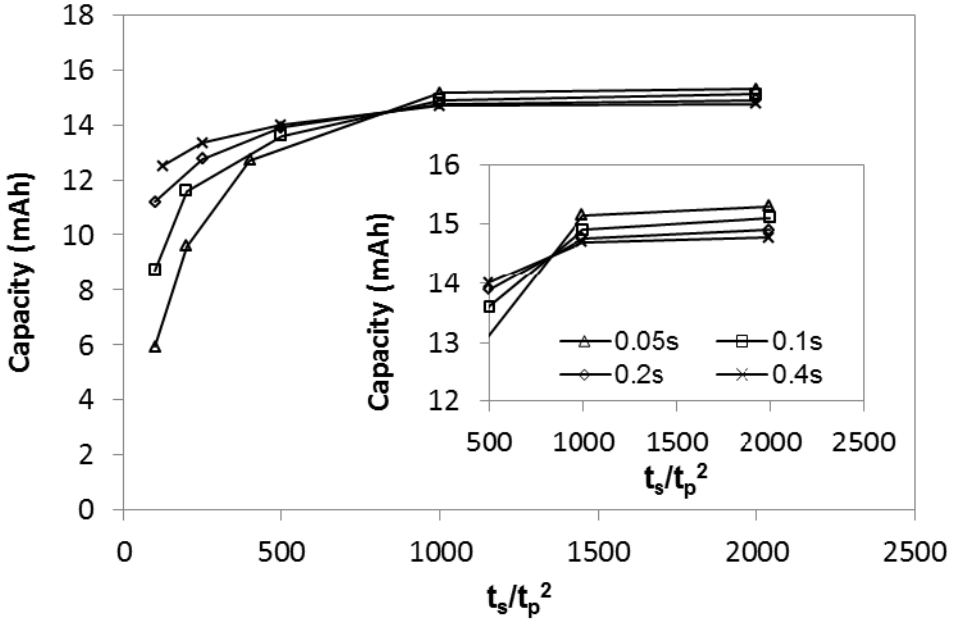

(c)

Figure 5.12 Impact of pulse length on battery capacity vs. t_s (a), t_s/t_p (b) and t_s/t_p^2 (c).

Table 5.2 Test table of standby times for different pulse length

t_p=0.05s			t_p=0.1s			t_p=0.2s			t_p=0.4s		
t_s (s)	t_s/t_p	t_s/t_p^2 (s^{-1})	t_s (s)	t_s/t_p	t_s/t_p^2 (s^{-1})	t_s (s)	t_s/t_p	t_s/t_p^2 (s^{-1})	t_s (s)	t_s/t_p	t_s/t_p^2 (s^{-1})
0.25	5	100	0.5	5	50	1	5	25	2	5	12.5
0.5	10	200	1	10	100	2	10	50	4	10	25
1	20	400	2	20	200	4	20	100	8	20	50
2	40	800	5	50	500	8	40	200	10	25	62.5
2.5	50	1000	10	100	1000	10	50	250	20	50	125
5	100	2000	20	200	2000	20	100	500	40	100	250
10	200	4000	50	500	5000	40	200	1000	80	200	500
20	400	8000	100	1000	10000	80	400	2000	160	400	1000

As shown in Fig. 5.12 (a), for each pulse length, the battery capacity increased as the standby time increased, until a maximum capacity was reached, and further increase in the standby time did not increase the battery capacity any further. At this point the standby time was defined as the minimum standby time for full (or near full) relaxation for this pulse length. The relationship between the minimum standby time and the pulse length is of great interest for WS energy optimization and system design parameter selection. As the analysis in the previous chapter showed, the standby time needed for full relaxation (t) at a certain SOC should increase linearly with pulse length squared, i.e. $t \propto I^2 \cdot \tau^2$, where I is the pulse current and τ the pulse length. From Fig. 5.5 we estimated the minimum time for near full relaxation of a 0.1 s 10 mA pulse to be ~10 s. Time needed for 0.05 s, 0.2 s and 0.4 s 10 mA pulse is then expected to be 2.5 s, 40 s and 160 s. We can see that this prediction corresponds well with the experimental results. The 0.2 s and 0.4 s pulses reached a stable capacity at standby time of 40 s and 160 s respectively, as shown in the insert of Fig. 5.12 (a).

In the case of full relaxation, i.e. at t_s/t_p=400 in Fig. 5.12 (b) and $t_s/t_p^2 \geq$1000 in Fig. 5.12 (c), the total capacity decreased with increasing pulse length, and the difference in capacity for 0.05 s and 0.4 s pulse was a little less than 1 mAh. When full relaxation is realized between the pulses, the upper voltage remains at the OCP of the cell and does not change with pulse length. The decrease in total capacity with increasing pulse length was mainly due to the lower voltage, which was lowered as the pulse length increased.

Over the broad range of the standby times tested, the two "extreme" conditions are when the standby times are very long, enough to reach full relaxation, and when the standby times are very short. We found that the two ratios t_s/t_p and t_s/t_p^2 can be used to describe the battery capacities under these two extreme conditions, which can be explained by the controlling mechanisms represented by these two ratios. At standby times sufficiently long for full relaxation, the battery capacity correlates well with large values of t_s/t_p^2, for example, when $t_s/t_p^2 \geq$1000 in Fig.5.12 (c). In fact, at t_s/t_p^2=1000, standby time t_s is 2.5, 10, 40, 160s for t_p=0.05, 0.1, 0.2, 0.4 s, which corresponds the minimum standby time for full relaxation discussed above. Note that t_s/t_p for minimum standby time for full relaxation increased from 100 to 400 when pulse length increased from 0.1 s to 0.4 s. When the standby times are very short, for example, at t_s/t_p=5 (t_s=0.25, 0.5, 1 and 2 s for t_p=0.05, 0.1, 0.2 and 0.4 s), the total capacity obtained was small and dominated by the rate-capacity effects caused by the relatively high average current (I_{ave}=1.7 mA at t_s/t_p=5) resulting from the pulse discharge. Under this condition, the impact of pulse length on capacity was almost negligible, as illustrated by the clustered points at low t_s/t_p in Fig. 5.12 (b).

Between these two extreme conditions, the capacity increased as t_s, t_s/t_p and t_s/t_p^2 increased. For the same value of t_s or t_s/t_p, the total capacity decreased with increasing pulse

length. However, the change of capacity with pulse length at certain values of t_s/t_p^2 was the opposite (e.g. when t_s/t_p^2 <800). From Table 5.2 we can see that this is caused by the rapid change of t_s/t_p^2 with pulse length t_p. While t_s/t_p^2 can be used to best describe the voltage relaxation process after a single pulse or under full relaxation, it is not suitable for use in sustained pulse discharge cycling under incomplete relaxation. Under these conditions, the resulting capacity is dominated by other competing factors.

5.3.5 Impact of average current

We showed in the previous sections that standby current has only a minor effect on the average current, while the pulse current affects the battery capacity in multiple ways. In this section, a discussion of the impact of the average current for pulse duty cycles with varying pulse length and standby time, and constant standby current and pulse current. In Fig. 5.13 (a), the voltage profiles of pulses with a constant t_s/t_p of 20 (t_s=1, 2, 4, 8 s and t_s/t_p^2=400, 200, 100, 50 s^{-1} for 0.05, 0.1, 0.2, 0.4 s pulses, respectively) is shown, where the extent of relaxation is between the two extreme conditions mentioned above.

In Fig. 5.13 (a), all four pulse cycles have the same average current of 0.5 mA, and their upper voltages clearly follow the constant 0.5 mA discharge curve. Based on the voltage profile results of t_s/t_p=10-100, we found that in situations of incomplete relaxation, the upper voltage was closely related to, and slightly higher than, the galvanostatic discharge voltage profile at the average current of the pulse cycling. The smaller the pulse length, the higher the upper voltage appeared to be. This is because the upper voltage is the result of both the “background” concentration gradient and the relaxation of the concentration gradient caused by the pulse discharge right before a standby period. The average current does a good job of describing the

background concentration gradient, and the small variation with pulse length is due to the voltage relaxation in the thin outer layer of the solid particle.

In Fig. 13 (b), the total capacity achieved from the different pulse duty cycles is shown against the average current. On the whole, the capacity follows the trend of the rate-capacity effects of the battery. At high average current (t_s/t_p=5), the capacities were low and varied little with pulse length. At the same average current, the capacities for shorter pulses were higher than those of longer pulses. As shown in Fig. 5.13 (a), this difference was mainly due to the change of lower voltage with pulse length. The voltage loss dV2 increases linearly with the square root of pulse length. dV2 values for 10 mA 0.05 s, 0.1 s, 0.2 s and 0.4 s pulses were 38 mV, 52 mV, 77 mV and 107 mV, respectively, based on the experimental results from a fully charged cell initially at 3.1 V. At the same average current, the variation in the battery capacities was 1-2 mAh.

To demonstrate how these results can be used, let us consider an example where as much amount of data as possible must be sent out from a node as quickly as possible. A longer pulse can transfer more data per cycle; however, the time needed for relaxation is also longer. We first consider the average current consumption and notice that, for the same average current, the percentage of energy delivered during the pulses (data transfer) remains constant when I_p and I_s are fixed. The energy consumption rate is directly related to the data transfer rate. A shorter pulse length and a standby time that allows for near full relaxation are preferred for the optimization of battery capacity. Decreasing pulse length (e.g. from 0.4 s to 0.05 s in Fig. 13 (b)) will increase the overall amount of data transferred by 10-20%, depending on the duty cycle parameters used. (I_p=10 mA, I_s=25 μA).

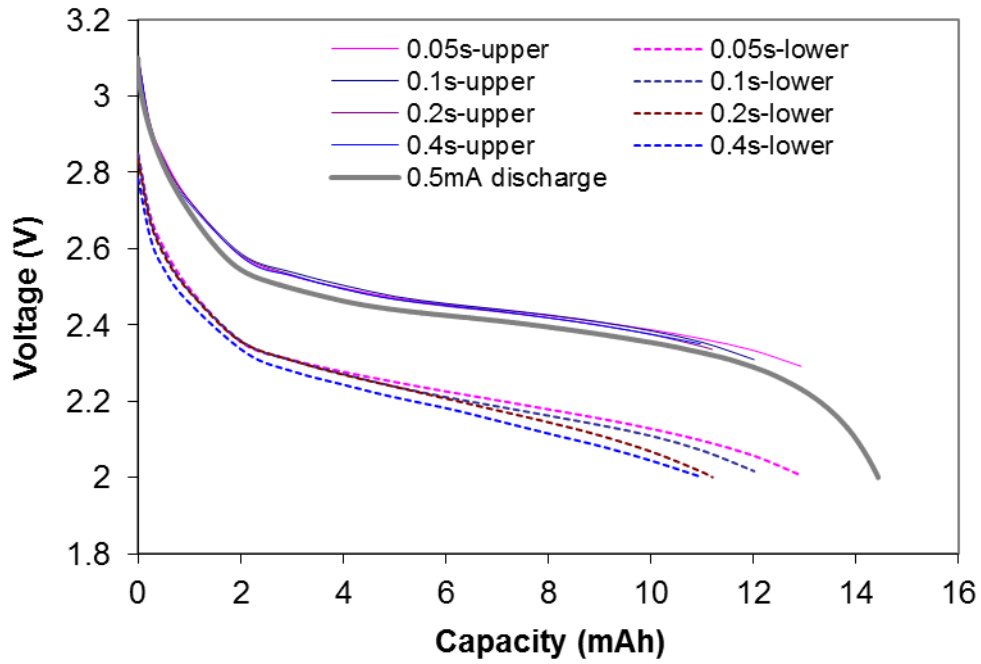

(a)

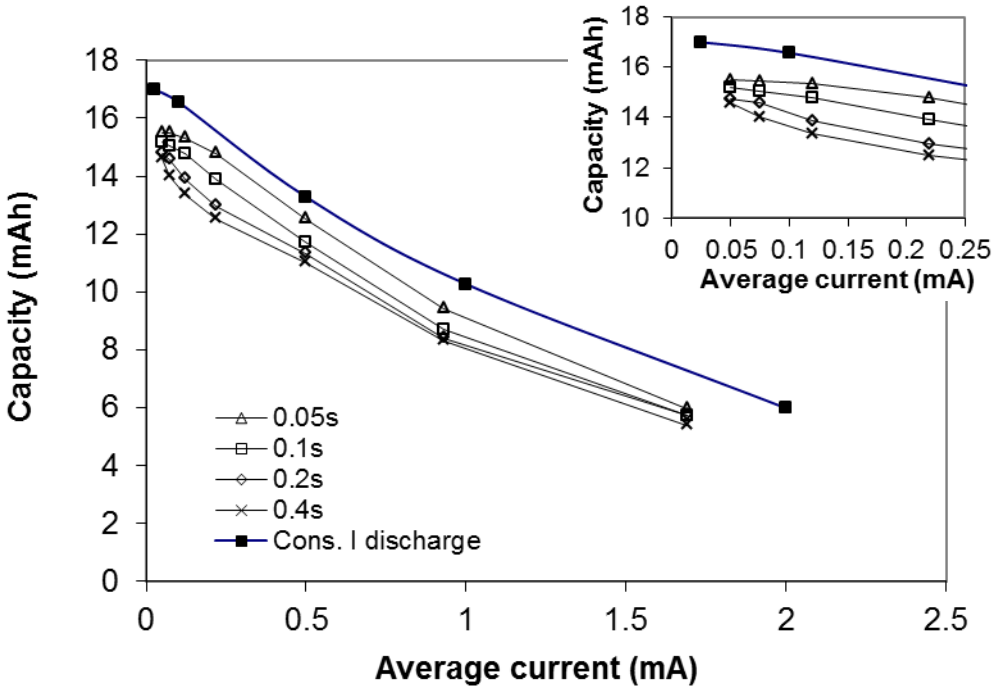

(b)

Figure 5.13 Impact of pulse length and average current on battery voltage for pulses with t_s/t_p =20 (a) and impact of pulse length and average current on total capacity (b). Duty cycle parameters: I_p=10 mA, t_p=0.05-0.4 s, I_s=25 µA, t_s=0.25 s-160 s.

Note that in this study the range of the parameters selected was relatively small, so that the sensitivity of the battery performance to the duty cycle parameters could be evaluated carefully. We can see for pulsed discharge (I_p=10 mA), capacity estimation that is based on the average current predicts the battery lifetime to within 10-20%.

5.4 Application to battery-aware WS system design

The results from Chapters 4 and 5, and the procedure illustrated thereby, can be used to predict the battery capacity more accurately during sustained pulse discharge cycling for a broad range of duty cycle parameters in order to optimize the WS system. The procedures and considerations in selecting the operating parameters of WS (I_p, I_s, t_p, t_s) are summarized below:

1. The standby current, I_s, of a WS system is normally on the order of μA or tens of μA. Due to the small magnitude of the standby current, its influence on the operating voltage and battery capacity is negligible. For ML1220 cells, we recommend a standby current of I_s <50μA (corresponding to 0.003 C-rate), based on the experimental results presented earlier. No significant impact on battery behavior was observed for standby currents of this magnitude for the ML1220. A similar C-rate for other cells should yield a similar result.
2. The pulse current, I_p, is associated with the transmission power level of the radio used, and needs to be considered first when selecting a battery for use with a WS as it determines the maximum capacity that can be extracted from a battery during pulse discharge cycling. The pulse capability of a cell can be evaluated with pulse cycling tests at different current levels with standby times sufficiently long for full relaxation between the pulses (see the next paragraph for standby time needed for full relaxation). We recommend using pulse currents that allow for greater than 50% of the full battery

capacity to be extracted through pulse discharge. The experimental studies on ML1220 showed that I_p<12.5mA should be used (see Figure 5.8).

3. Once the pulse and standby currents (I_p, I_s) have been determined, the battery capacity can be maximized by selecting the standby time, t_s, to allow for full (or near full) relaxation between the pulses for a pulse length t_p. A near full voltage relaxation corresponds to the state where, at the end of the standby period, the voltage is relaxed to within ~5mV of the open-circuit potential of the cell. The standby time needed to achieve this can be calculated from Equation 4.16. For example, application of Equation 4.16 to the ML1220 cell yields the following relationship from which the standby time may be estimated: $t_s/t_p^2 \geq 1000$ for I_p=10mA, I_p, I_s<50μA.
4. When a WS is operated with a higher duty cycle factor that allows for only partial voltage relaxation, the overall capacity achievable during pulse discharge cycling can be estimated as that of a galvanostatic discharge at the same average current as the duty cycle of interest. The actual pulse discharge capacity will generally be 10-20% lower than this estimate. At a given value of the average current, short pulse lengths tend to have slightly higher total capacity than longer pulse lengths.

The following two examples demonstrate how the testing procedures and results can be used for system optimization.

Case I: *Optimization of the duty cycle $\mathcal{D}$ to maximize the amount of data transferred from a node on limited battery energy*. Because the amount of energy consumed during the pulses directly relates to the amount of data transferred, this case involves how to choose a standby time t_s for a pulse length t_p (when I_p and I_s are known) so that the capacity delivered in the form of pulses is maximized. The capacity by pulses only is a product of the total capacity assessed and

the percentage of capacity delivered as pulses: $C_{pul} = C_{tot}\ \theta_p$. For a certain t_p, the change in C_{pul} is dominated by the change in C_{tot}, which decreases as $\mathcal{D}$ increases. As standby time increases and $\mathcal{D}$ becomes smaller, C_{tot} becomes constant at the maximum capacity, and C_{pul} is dominated by the change in θ_p with t_s. The maximum fraction of the battery capacity delivered as pulses occurs around $\mathcal{D}$ =2% for the different pulse lengths used with ML1220 cells.

Case II: *Maximize the rate of data sent with limited battery capacity*. In this case, the specific conditions chosen will depend on the priority of system optimization goals. Here we consider how such a problem might be approached. We first consider the relationship of the total capacity with the average current consumption (Fig. 5.13), and notice that energy consumption rate relates directly to the data transfer rate. For a duty cycle factor, $\mathcal{D}$, higher than 2%, i.e. the average current I_{Ave} higher than ~0.2mA, the change of C_{pul} is dominated by the change of C_{tot} with I_{Ave}. $\mathcal{D}$ values of 4-5% are recommended, in which case the energy consumption rate is more than doubled, while the C_{pul} is still close to the maximum value achieved at $\mathcal{D}$ =2%. For the same I_{Ave}, the percentage of energy delivered by the pulses remains constant if I_p and I_s are fixed. A shorter pulse length and a standby time that allows for near full relaxation are preferred from the battery's perspective. Decreasing pulse length (from 0.4s to 0.05) could increase the overall amount of data transferred by 10-20% at the same average data transfer rate.

5.5 Summary

Systematic experimental studies were carried out under various pulse cycling conditions. The pulse cycling tests were designed so that the impact of each operating parameter (i.e. peak

current I_p, standby current I_s, pulse length t_p, standby period t_s) was evaluated. Due to the small magnitude of the standby current, the influence of the standby current on the operating voltage and battery capacity was negligible, and thus the voltage analysis for relaxation at zero current can be used for relaxation at low currents ($\leq$50 μA) without introducing significant error. The pulse current had a significant impact on the lower voltage and determined the maximum capacity that could possibly be extracted from a battery affected by the duty cycle factor. For each pulse length studied, the battery capacity increased as the standby time increased, until a maximum capacity was reached and further increase in the standby time did not increase the battery capacity any further. The minimum standby time for full (or near full) relaxation was found to correlate well with ratio t_s/t_p^2.

In situations of incomplete relaxation, the upper voltage was the result of both a "background" concentration gradient and the relaxation of the concentration gradient caused by the pulse discharge right before a standby period. The "background" concentration gradient was associated with the average mass transfer rate of the lithium ion, which can be expressed by the time average current. At the same average current, the capacities for shorter pulses were higher than those of longer pulses. These results and the procedure illustrated thereby can be used to predict the battery capacity during sustained pulse discharge cycling for a broad range of variables in order to meet system optimization goals by selecting suitable duty cycle parameters for WS operation.

6 EXPERIMENTAL STUDY ON RECHARGE STRATEGIES

6.1 Introduction

For distributed wireless sensors that need a longer operating life than can be provided by a battery alone, hybrid power sources that combine energy harvesting with a rechargeable battery are of great interest [44-46]. Energy harvesting devices convert ambient energy into electrical energy, which is stored in the battery and utilized by the WS node. The most common sources of ambient energy include solar power, radio-frequency, thermal gradients and mechanical vibration. Research shows that it is reasonable to expect from tens of μW to a few mW (per cm^2) of power to be harvested from ambient energy [45]. Coupling energy harvesting techniques with rechargeable batteries can extend the WS lifetimes significantly. A well designed hybrid system also has the potential to reduce the overall size of a power supply by allowing smaller batteries than would be required in a non-renewable system [44].

In a "battery/power harvesting" hybrid system, the battery provides the peak power and the energy harvesting device supplies the standby power to the sensor system and charges the battery. Because standby periods are much longer than the discharge pulses, the energy harvesting device can operate at much lower power levels than the peak power. Since a hybrid system extracts energy from the environment, recharge of the battery depends on the availability of energy. The operation of the energy harvesting devices may be 1) intermittent, which means recharge of the battery is only available for certain periods of time or 2) continuous, in which

case the battery can be charged after every pulse during the standby period following the discharge. When energy harvesting is not available, the battery provides the peak power as well as the standby power. In this study it is assumed that the energy harvesting device is continuously active so that the effects of recharge strategies over repeated pulse discharge-charge cycles can be investigated.

With the hybrid power system, the useful life of a WS is not limited by the amount of energy that is stored initially, and in theory, the system should be able to continue functioning indefinitely. In practice, however, the lifetime will be limited by the cycle life of the batteries. Proper charge and discharge strategies are needed in order to insure the battery life is extended. In addition, lithium batteries often suffer from capacity losses during cycling, which result in a less than 100% charge efficiency [52-54]. Battery charge efficiency is the ratio (expressed as a percentage) between the amount of charge removed from a battery during discharge and the amount of charge used during charging to restore the original capacity. Charge efficiency and charge time can be influenced considerably by the battery state of charge and charging strategy [18, 55]. Energy losses during pulse cycling may eventually lead to battery voltage degradation if they are not properly compensated during charging, and the WS node will then expire.

The average power from the energy harvesting device must be able to supply the standby power of the WS, and recharge the battery to compensate for the capacity delivered by the pulse discharge and the capacity losses during cycling. Information of the capacity losses during WS duty cycling is important for hybrid power system design. The average power needs to be precisely controlled so that it should meet the above recharge needs, and at the same time prevent the battery from overcharge. It is desirable to minimize the capacity losses during cycling, because they compromise the energy efficiency of the system by adding an additional

load, possibly causing an increase in the size of the energy harvesting device. In this study we investigate the performance characteristics of rechargeable lithium coin cells under possible discharge and charge conditions in hybrid power supplies, with a focus on the capacity losses during WS duty cycling. The objective of this chapter is to evaluate different charging strategies to find the most energy efficient charge conditions for hybrid power systems used to power WSs.

6.2 Experimental

Rechargeable ML1220 coin-type cells (from Panasonic) were used in this investigation. After the initial low rate discharge-charge cycle and prescreening tests, the cells that passed the screening tests were divided into two groups. In the first group, the batteries were charged to 3.1V (0%DOD) for cycling tests or self-discharge tests. In the second group, the batteries were discharged at 1mA to 80% of their rated capacity (13.6 mAh remaining of the 17 mAh possible). Batteries in the second group were thus at 20% DOD and the OCV of the cells was 2.59±10 mV.

Since this study was focused on recharge strategies for cells undergoing cycling characteristic of WSs, for all cases, each pulse discharge had a peak current of 10 mA and a length of 0.1 s (0.0016%DOD). For constant current charge, termination of charge was controlled by either charging time (CCt) or end point voltage (CCV). For CCt charging, we investigated two types of cycling, with or without a 2 s rest step between charge and discharge. For all other recharge strategy tests, the 2 s rest step was adopted. For constant voltage charge, termination of charge was controlled by current (when charging current dropped below 5 μA) or by capacity (when the charge capacity of a charging step equaled the capacity delivered during a discharge pulse). Procedures specific to particular tests are described below. The recharge strategy tests were summarized in Table 6.1.

Table 6.1 recharge strategy test summary

Charging method	Cell condition		Termination of charge	
Constant current (CCt)	0%DOD	20%DOD	Time (Charge=0.001C)	PC (no rest period)
				PRCR
Constant current (CCV)	0%DOD	20%DOD	Voltage (3.1V or 2.6V)	
Constant voltage (CV)	0%DOD	20%DOD	Current (<5μA)	Charge (=10mA·0.1s=0.001C)

6.3 Results and discussion

6.3.1 The impact of a rest period between charge and discharge

The first recharge strategy considered was constant current charging, and the termination was controlled by charging time, so that the overall coulombic charge capacity obtained during charging equaled to the charge delivered during the previous discharge pulse. Two types of discharge-charge cycles were tested, as listed in detail in Table 6.2. The first one was a simple pulse discharge-charge cycle (PC), and the second one had a 2s rest step between the pulse discharge and charge step (PRCR). Both types of cycling tests were performed on ML1220 cells at 0% DOD (OCV 3.09-3.10V) and at 20%DOD (OCV 2.59V±10mV). The voltage profiles during PC and PRCR cycling over 10,000 cycles are compared in Fig. 6.1 (0% DOD) and Fig. 6.2 (20%DOD).

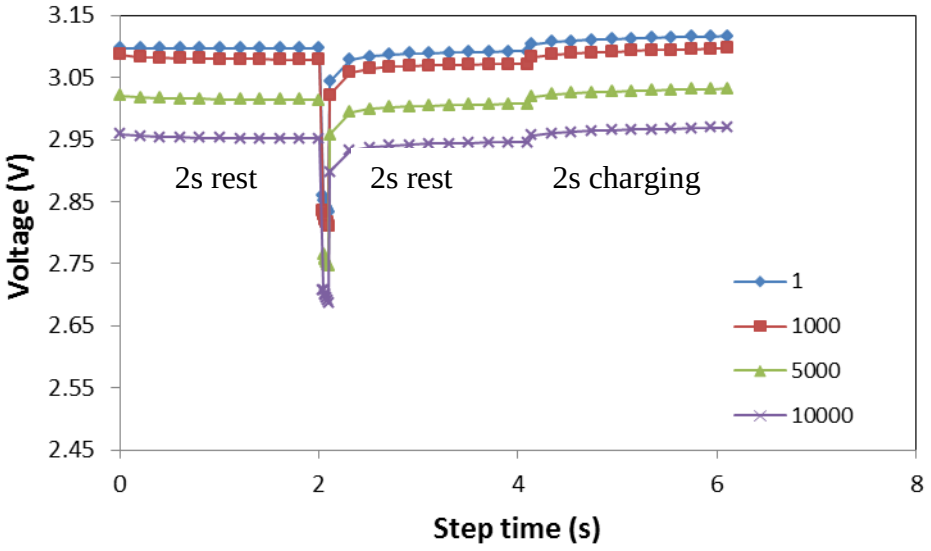

(a)

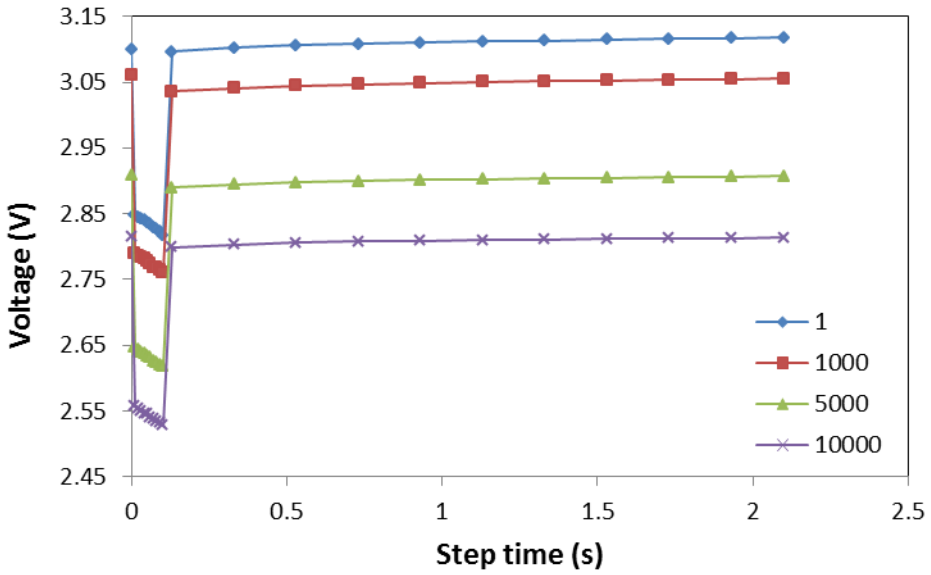

(b)

Figure 6.1 Voltage profiles for PRCR (a) and PC (b) discharge-charge cycling at fully charged state

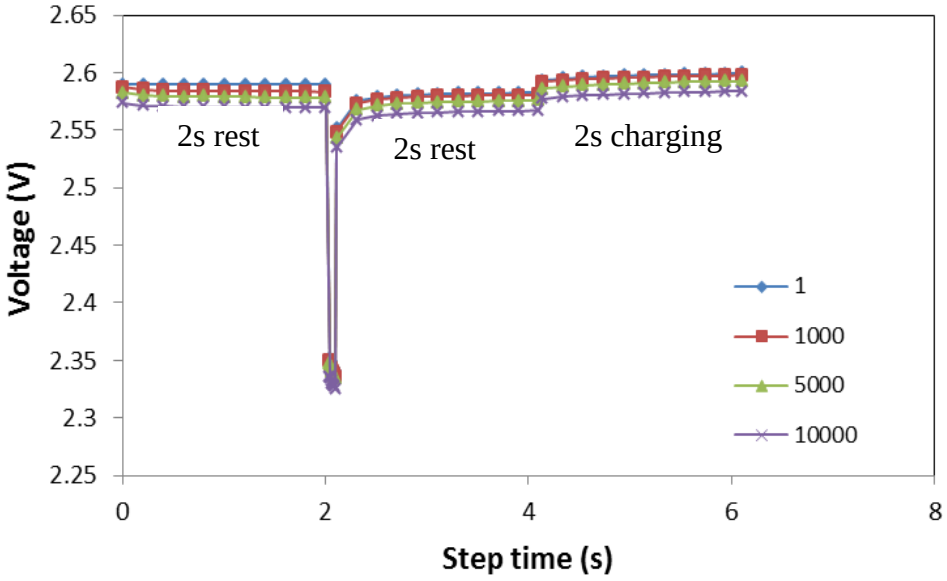

(a)

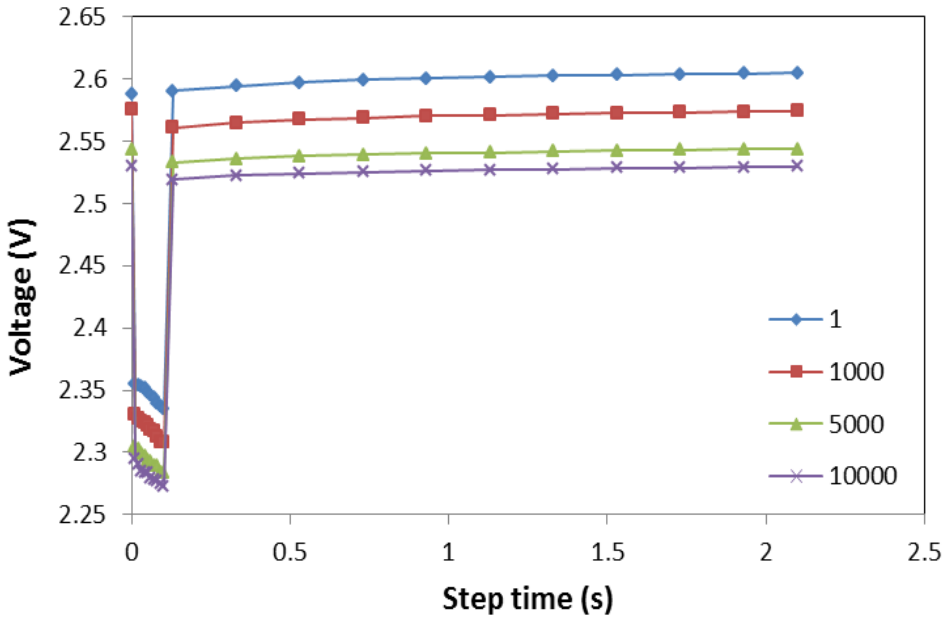

(b)

Figure 6.2 Voltage profiles for PRCR (a) and PC (b) discharge-charge cycling at 20% DOD for 10,000 cycles

We can see that, in general, the voltage decreased gradually during cycling. For cells cycled from the fully charged state, the voltage profile of the 10,000th cycle of the PC cycling was ~300mV lower than that of the first cycle; in contrast, this voltage loss was ~150mV at the end of 10,000 cycles for PRCR cycling. At 20% DOD, the voltage loss for PRCR cycling was ~10mV compared to ~70mV for PC cycling over 10,000 cycles. The voltage losses for both PC and PRCR cycling at 20%DOD were significantly less than that at 0%DOD.

Table 6.2 Description of PC and PRCR cycling tests

Cycle description	Cycle steps			
PC (Pulse Dis.+Charge)	Discharge		Charge	
	10mA, 0.1s		0.5mA, 2s	
PRCR (Pulse Dis. +Rest+Charge+Rest)	Discharge	Rest	Charge	Rest
	10mA, 0.1s	0mA, 2s	0.5mA 2s	0mA, 2s

After 10,000 pulse discharge-charge cycles, the cells entered a 12-hour rest step, during which the cell voltage was measured. The voltage profile during the 12-h rest is shown in Fig. 6.3. Following the rest period, the cells were charged to their initial voltages (the OCV before the cycling tests) with a constant voltage charging step until the charging current dropped below 5μA. The total capacity obtained from this charging step was evaluated as the capacity loss during the cycling test. The capacity loss results are summarized in Table 6.3 and 6.4.

In Fig. 6.3, there is an initial dip in the voltage relaxation profiles and then follows a long slow voltage recovery. Because the last step before the 12-h rest period was charging, the voltage drop seen at 0.01-50s was due to the voltage relaxation caused by the charging step right before the rest period. The magnitude of the initial voltage drop, evaluated as the voltage difference between the voltage of the first data point (at t=0.01s) and the minimum voltage reached during

this initial period, was ~15 mV for both PC and PRCR cycling at 20%DOD, and ~20 mV at 0% DOD. While the initial voltage relaxation for charging was similar, the long-term voltage recovery due to the high discharge pulses was quite different for the two types of cycling. For PRCR cycling, the relaxation curve was relatively flat, and the total voltage recovered, evaluated as the voltage difference between the voltage at the end point of the relaxation and the minimum voltage reached during the initial period, was ~15 mV, most of which was relaxed during the first few hours. For PC cycling, the total voltage recovered was ~30 mV, and the voltage relaxation took nearly 10 hours before it slowed down and became negligible.

The voltage relaxation profiles indicate that the high-rate pulse discharge has a much greater effect on the cell than the slower charging process. The concentration gradient in the solid material caused by the charging current could be relaxed within tens of seconds. The rest of voltage relaxation was dominated by the effects due to the discharge pulses. Longer relaxation times indicate that the concentration gradient penetrates deeper into the activate material particle, and the electrochemical reaction region may also penetrate deeper into the electrode. With a 2 s rest step between the discharge and charge, the concentration gradient caused by the (10 mA 0.1 s) pulse discharge was effectively reduced and hence the relaxation profile at the end of PRCR cycling was relatively flat.

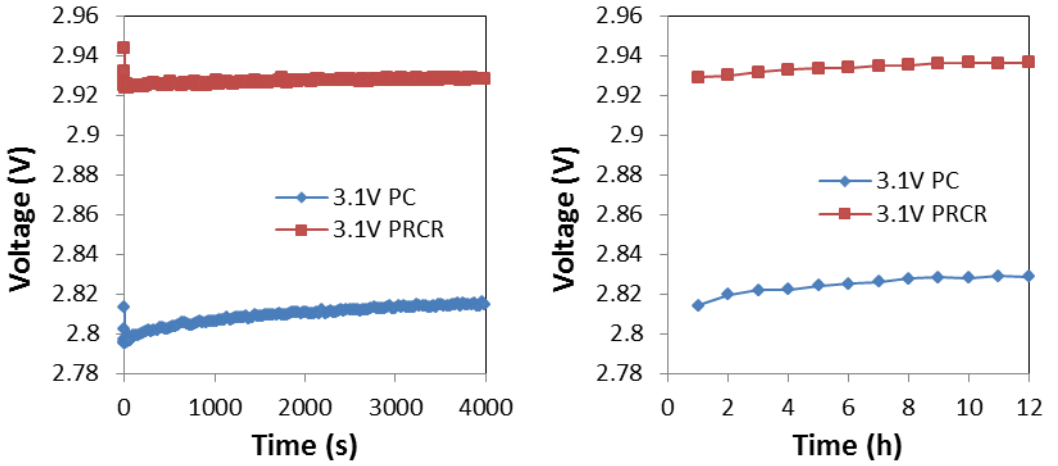

(a) (b)

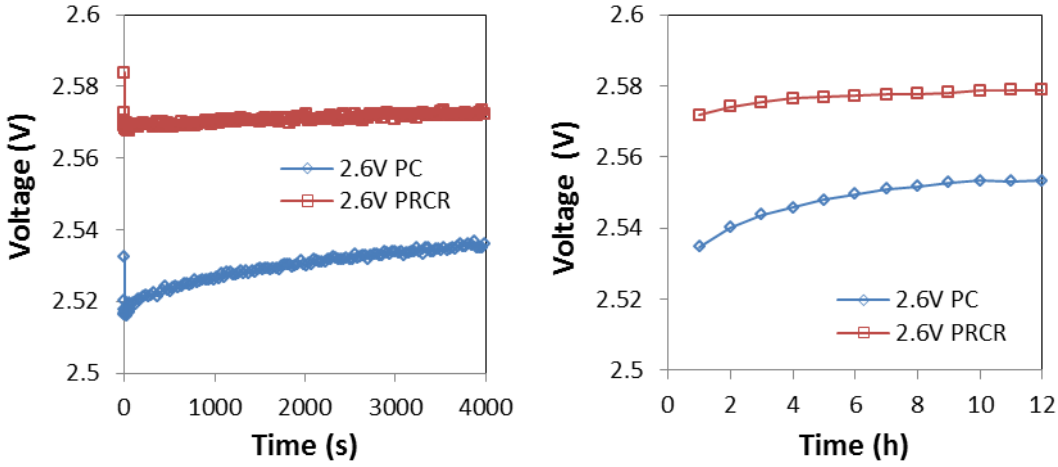

(c) (d)

Figure 6.3 Voltage relaxation at the end of 10,000 cycles of PC and PRCR tests at 0%DOD (a,b) and 20%DOD (c,d). Voltage relaxation during the first hour (a,c) and long term 1-12 hours (b,d).

Because the charging current and time were controlled so that the charge delivered during a discharge pulse and the subsequent charge were equal, ideally the battery should stay at the same state-of-charge during the cycling if all the charge goes into the desired Faradic reactions. In practice, lithium batteries suffer from capacity losses during cycling. The possible causes of

capacity losses include side reactions that lead to permanent cell degradation (electrolyte decomposition, SEI layer formation, etc.) and reversible reactions caused by the cell's local SOC or concentration gradient (e.g. spontaneous Li+ reinsertion due to instability of de-lithiated cathodes).

Table 6.3 Capacity loss result for cycling tests at fully charged state (~3.1 V)

Recharge current and time		0.5 mA 2 s	0.2 mA 5 s	0.1 mA 10 s
Capacity loss at the end of 10,000 cycles (±0.03 mAh)	PRCR (with 2s rest period)	0.27 mAh	0.29 mAh	0.28 mAh
	PC (no rest period)	0.78 mAh	0.75 mAh	0.79 mAh

Table 6.4 Capacity loss result for cycling tests at 20% DOD (~2.6V)

Cell condition		Fresh cells	Seasoned cells
Capacity loss at the end of 10,000 cycles (0.5 mA, 2 s charging)	PRCR (with 2s rest period)	0.03(±0.02) mAh	0.19(±0.06) mAh
	PC (no rest period)	0.12(±0.03) mAh	0.3 (±0.12) mAh

From Table 6.3, we can see that at 0%DOD, the capacity loss is not a strong function of charging current and time, but varies significantly by type of cycling. The capacity loss for PC cycling was nearly three times higher than that of PRCR cycling. At 20%DOD, the capacity losses for both types of cycling were much less than what were observed at 0%DOD. The capacity loss did not appear to be a strong function of charging current and time either. However, we found the capacity loss at 20% DOD increased when the cycling tests were repeated on the same cell. In Table 6.4, the fresh cells refer to cells that were just discharged to 20%DOD from 3.1 V and had not been through any cycling tests at this SOC. Seasoned cells refers to cells that had been through at least 40,000 cycles of PRCR or 10,000 cycles of PC tests.

The self-discharge characteristics of a cell very likely affect the capacity loss during cycling. Self-discharge is a phenomenon in batteries in which internal chemical reactions reduce the stored charge of the battery without any connection between the electrodes. The self-discharge rate was evaluated at 0% DOD and at 20%DOD on fresh cells and seasoned cells. The cells were first charged to 3.1 V or 2.6 V and kept at this voltage until the charging current dropped below 5 µA. The cells were then allowed rest for 48 hours at open circuit. During the rest time, the cell voltage dropped slightly due to self-discharge. After 48 hours the cells were charged back their original voltage with the same constant voltage charging procedure until the charging current dropped below 5 µA. The charge passed during the recharge process (mAh) represents the overall capacity loss due to self-discharge. The self-discharge rate normally decreases with time. Here we calculated the average self-discharge rate per day during the first 48 hours of rest. We found that the self-discharge rate was a strong function of cell state-of-charge and cell testing history (fresh or seasoned). The self-discharge rate at 3.1 V was much higher than measured for either the fresh or seasoned cells at 2.6 V. At 2.6 V, the self-discharge rate of the seasoned cells was an order of magnitude higher than that of the fresh cells.

Table 6.5 Results of self-discharge rate

Cell condition	3.1 V	2.6 V (fresh)	2.6 V (seasoned)
Self-discharge rate	0.038 mAh/day	0.00083 mAh/day	0.0091 mAh/day

The capacity loss for PRCR cycling was very likely due to the spontaneous Li+ reinsertion during or right after charging, which is also the main cause of self-discharge for these cells [18, 78, 79]. Note that for PRCR cycling, the voltage profiles were nearly uniformly distributed, (see Fig. 6.1(a) and 6.2 (a)), that is, the voltage losses varied almost linearly with

cycle number. The resulting capacity loss also varied linearly with cycle number. For example, the capacity loss at the end of 20,000 PRCR cycles at 3.1 V was ~0.56 mAh, almost double that observed at the end of 10,000 cycles (see Table 6.3).

The capacity loss for PC cycling was probably the result of several causes: 1) side reactions; 2) double layer capacitive effects; 3) spontaneous Li+ reinsertion. The exact cause of the additional capacity loss observed during PC cycling is not known. The two rest periods impact double layer charging/discharging and provide time for at least partial relaxation of concentration gradients. With no rest period between the discharge and charge step, the electric field in the double layer on the electrode surface would switch directions upon charge and discharge. Imbalance between the charge and discharge of the double layer due to composition changes, may contribute to an observed capacity loss. In addition, the double layer may affect the reaction kinetics when the surface charge or the electric field in the double layer changes.

A possible explanation for the observed behavior is that the concentration variations exaggerated by the absence of rest periods cause mechanical strain in the solid particles that leads to particle fracture and exposure of new interfacial surface to the electrolyte. With no time for relaxation of the concentration gradient caused by the high-rate discharge, the lithium concentration variation in both the solid and the liquid phase is larger during PC cycling than during PRCR cycling. During charging, the lithium diffusion flux near the surface of the solid particle transfers lithium to the surface where it reacts. Deeper in the solid particle, the residual concentration gradient caused by the discharge pulse drives lithium to diffuse into the center of the particle. Concentration variations can lead to stresses that fracture particles and expose new surface area. New surfaces will react with electrolyte in order to form SEI. This reaction consumes cyclable lithium. Evidence for this possible mechanism comes from Figs. 6.1(b) and

6.2 (b), in which the voltage losses did not vary linearly with cycle number for PC cycling. The voltage loss was more severe at the beginning of the cycling and decreased over time, which may indicate a concentration distribution evolution where the concentration variation flattens out with extended cycling and a quasi-steady state is established over time. Nevertheless, other possibilities exist and the mechanism responsible for capacity loss during pulse cycling still needs further investigation.

6.3.2 Constant current charging (CCV)

In this section, we describe results from experiments where the battery were charged at a constant current of 0.5 mA until the cell voltage reached a preset value of 3.1 V for 0%DOD cells or 2.6 V for 20%DOD cells (seasoned). The pulse discharge-charge cycling procedure was as follows: 10mA, 0.1s pulse discharge, 2 s rest, 0.5 mA charge until 3.1 V (or 2.6 V), 2 s rest. The voltage profiles during cycling are shown in Fig. 6.4. Because for CCV cycling the charging was controlled by the cell voltage, the resulted charging capacity was of great interest. The charge return factor, the ratio of the amount of charge during charging to the charge removed from a battery during a discharge capacity was evaluated over the 20,000 cycles and the result is shown in Fig. 6.5.

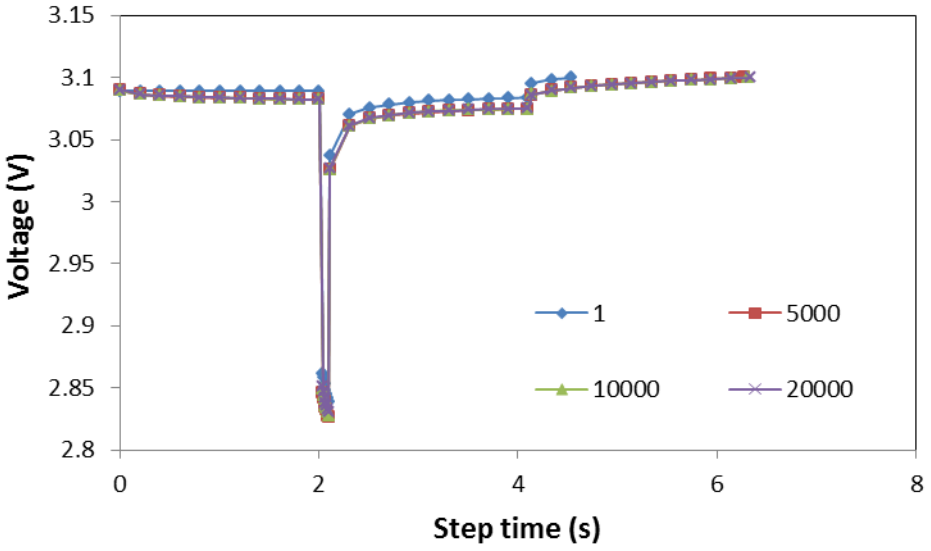

(a)

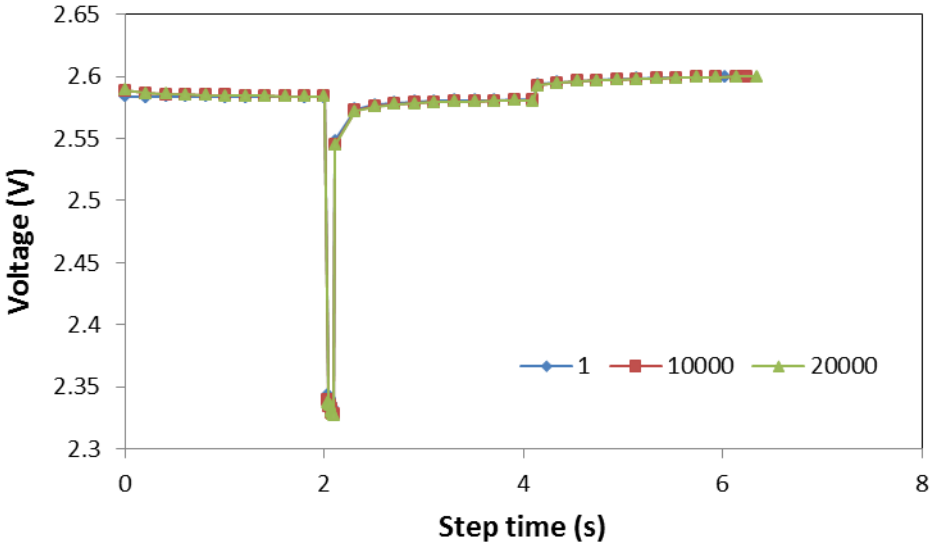

(b)

Figure 6.4 Voltage profiles for CCV discharge-charge cycling at 0% DOD (a) and 20% DOD (b) over 20,000 cycles

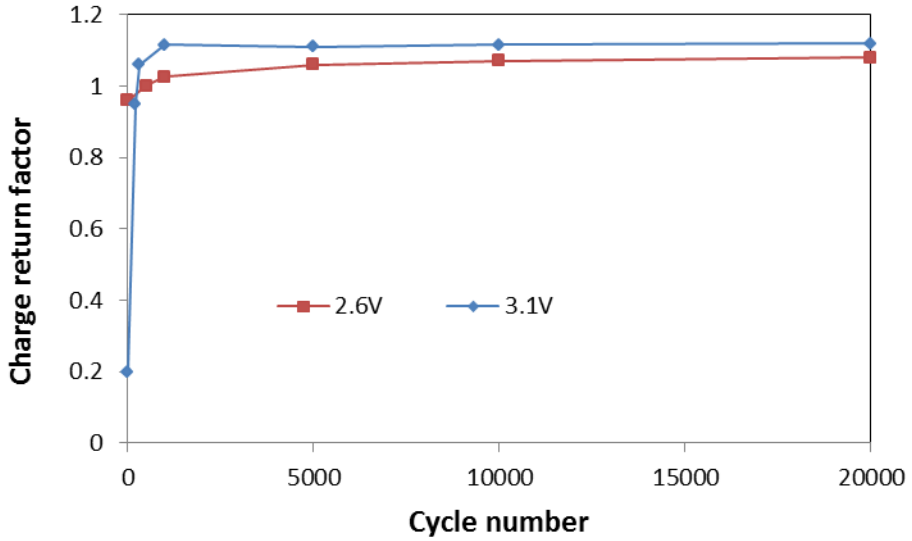

Figure 6.5 Charge return factor for CCV discharge-charge cycling at 0% DOD and 20% DOD over 20,000 cycles

From Fig.6.4 we can see that the voltage profiles varied little with cycle number, because this charging method allows keeping a constant voltage by compensating the voltage or capacity loss during charging. In Fig. 6.5 the charge return factors at both SOC increased with cycle number and reached a stable value during cycling. At 3.1 V, the charge capacity of the first few cycles was relatively small due to the relatively small difference between the preset cutoff voltage (3.1 V) and the actual cell voltage. The charging capacity increased rapidly as the polarization effects of the pulse discharge decreased the cells voltage in a few hundred cycles. At 5000^{th} cycle, the charging capacity was 106% of the discharge capacity at 20%DOD, and 112% at 0%DOD. At the end of 20,000 cycles, the charge return factors increased to 108% for cells at 20%DOD, and kept at 112% for 0%DOD cells. This indicates that in order to compensate capacity losses and avoid voltage drop during cycling, an extra charge of 6-8% and 12% is needed for cells cycling at 20%DOD and 0%DOD respectively. The results are consistent with

the observation made with CCt cycling in the previous section and confirms that cycling at 20%DOD is more energy-efficient than at 0%DOD.

6.3.3 Constant voltage charging (CV)

In constant voltage charging strategy, we kept the voltage at 3.1 V (or 2.6 V) until the charging current dropped below 5 μA or until the charge capacity of a charging step equaled the capacity delivered during a discharge pulse. The charging was terminated by the condition that comes first. We also set a current limitation of 1mA to protect the cell; that is in any condition, the charging current cannot exceed 1mA. Constant voltage charging is also called taper charging, since the charging current is associated with the voltage difference between the charging voltage and the actual cell voltage, and the charging current would decrease as the cell voltage increases during charging. The voltage profiles for CV discharge-charge cycling at 0% DOD and 20% DOD are shown in Fig. 6.6. The charging time (which affects the duty cycle factor) and the maximum charging current are shown in Fig. 6.7.

The cells were at 3.10 V before the cycling started at 0%DOD. The cells were ~7 mV lower than the 3.1 V charging voltage at the end of the 2 s rest period following the first discharge pulse, which enabled an initial charging current of ~0.1 mA. In this initial cycle, the total charging time was ~12 s. The cell voltage continued to decrease due to the polarization effects of the pulse discharge, and as the voltage difference (between the preset charging voltage of 3.1 V and the cell voltage) increased, the maximum charging current increased as well. At around 5000 cycles, the cell voltage was 50 mV lower than 3.1 V, which caused the maximum charging current to reach 1 mA. The current was not allowed to exceed 1 mA because of the preset current protection, and the maximum charging current were controlled at 1 mA after 5000 cycles. As the maximum charging current increased to 1mA, the charging time decreased to ~1 s,

where the capacity reached the value of 0.001 C, which is the condition for charge termination. At 0%DOD, the charging was always terminated by the limit of charge capacity passed because of the relatively high charging current.

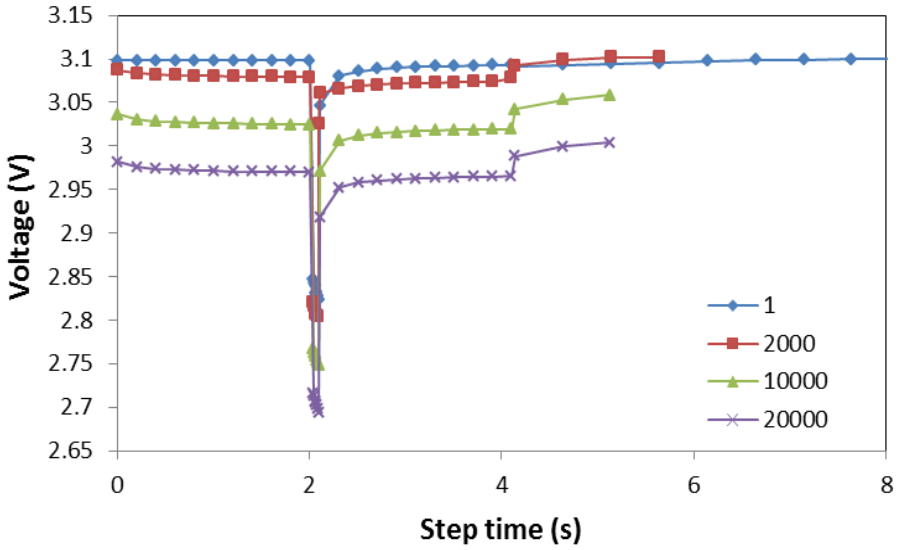

(a)

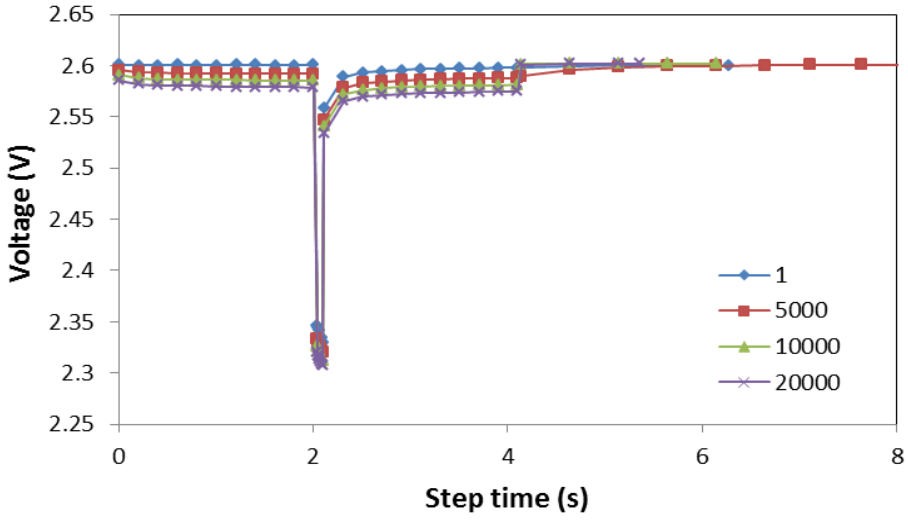

(b)

Figure 6.6 Voltage profiles for CV discharge-charge cycling at 0% DOD (a) and 20% DOD (b) over 20,000 cycles

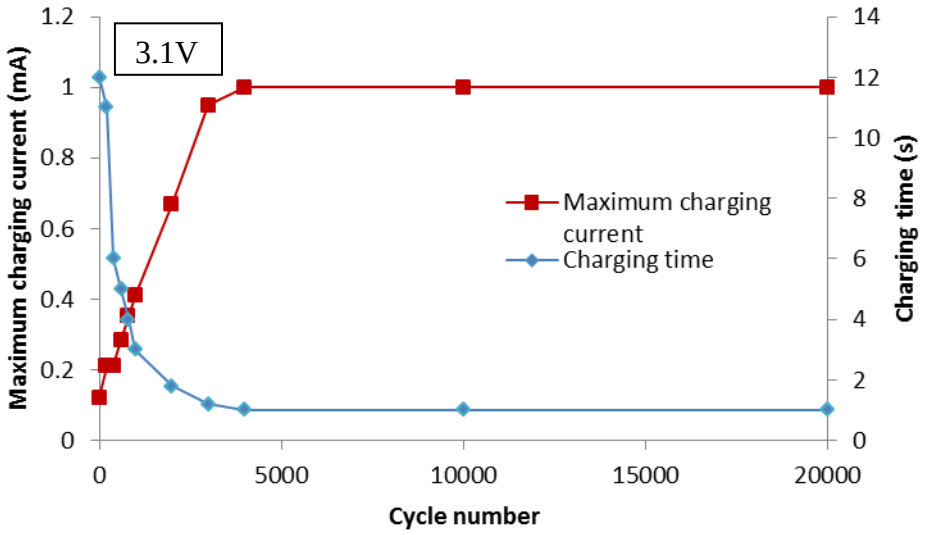

(a)

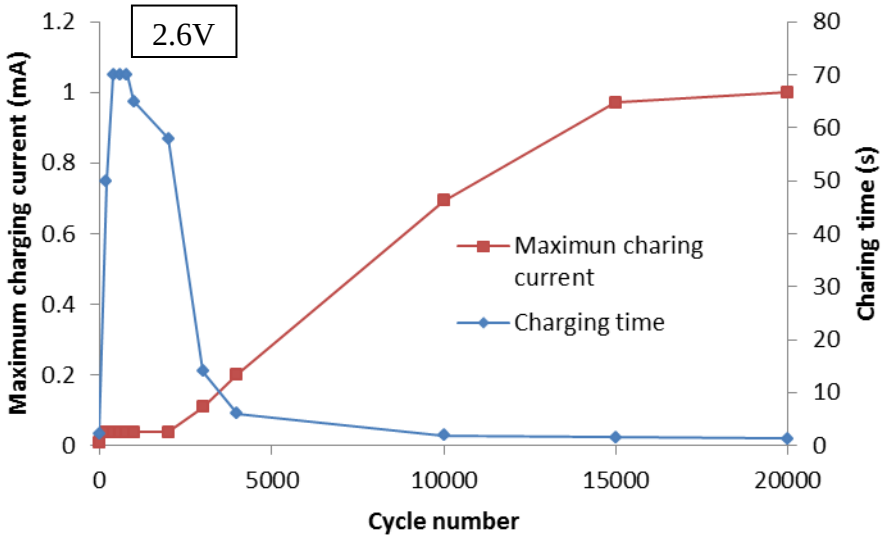

(b)

Figure 6.7 The maximum charging current and charging time during CV discharge-charge cycling at 0% DOD (a) and 20% DOD (b) over 20,000 cycles

At 20%DOD, the cells were at 2.60 V before the cycling started. The voltage recovery was faster and the cells were ~2 mV lower than the 2.6 V charging voltage at the end of the 2 s rest period following the first discharge pulse, which resulted in an initial charging current of ~7 μA. The charging current dropped below 5 μA in 2 s. The charging capacity was far below the capacity constraint in the first few hundreds of cycles, and the charge termination was control by charging current (when it dropped below 5 μA). The maximum charging current increased slowly and so did the charging time until a peak value of 70 s is reached, where the charging current was slightly higher than 5μA at the end of charging and the charge termination started to be controlled by charge capacity. The maximum charging current continued to increase with cycles, until the 1 mA limitation was reached around 15000 cycles. The maximum charging current and charging time did not change after 15000 cycles. Note that in CV charging, the voltage losses were observed because the charge return factor was always no greater than 1 due to the termination schemes preset.

6.4 Summary

An important aspect of the rechargeable lithium cells chosen for use in this study is their potential to be coupled with a power harvesting device to extend the operating lifetime of WSs by extracting ambient energy to charge the battery. Battery pulse discharge-recharge cycling as would occur in a hybrid power system was investigated. The recharge strategies, including constant current and constant voltage charging, were evaluated in terms of cell voltage, capacity losses and energy efficiency during cycling. Results from the initial cycling tests suggested the importance of a rest period between the discharge and charge step of a cycle. PRCR cycling with 2 s rest period could lower the capacity loss to 25% or less of that of PC cycling with no rest period over 10,000 cycles. Cycling the battery at 20%DOD rather than at 0%DOD reduced

the capacity loss by nearly 50% during cycling. Initial experimental investigation on recharge showed some very interesting trade-offs between the recharge current, recharge time and battery state-of-charge (SOC). More extensive studies are needed to identify the most effective and efficient recharge strategy, and to provide a fundamental understanding of the mechanism responsible for capacity loss during pulse cycling.

7 CONCLUSIONS AND RECOMMENDATIONS

Understanding the influence of WS operating conditions on battery performance and lifetime is critical to realizing battery-aware system designs in wireless sensing systems to truly maximize the energy that can be extracted from a given battery. In this study, we focused on small-sized lithium coin cells that are of interest for use in both existing and future WS systems. This dissertation combined theoretical analysis with experimental investigation of the behavior of these cells during sensor duty cycles in order to gain the desired understanding.

The transient behavior of commercial lithium coin cells during pulse discharge and subsequent relaxation was investigated with single-pulse experiments and EIS experiments. With EIS experiments, we identified the magnitude of the rapid voltage losses that occur upon initiation and termination of the pulse that are associated with ohmic and interfacial resistances. Solid phase diffusion in the cathode was found to be the major contributor to the "slow" transient voltage change that occurred during and after a pulse. A simple analytical model was developed to describe the time-dependent voltage and the corresponding non-uniform concentration distribution for the thick porous electrode. The analysis showed that the resulting penetration depth of the reaction, L/ν, was ~70 μm, much less than the electrode thickness of 1 mm. A fit of the analytical model to experimental data permitted an estimate of the solid phase diffusivity. Independent fitting of the pulse data and relaxation data both yielded a diffusivity of $D \sim 4\times10^{-11}$ cm^2/s, which agreed well with measured values in literature.

The voltage change with time, both during a pulse and following a pulse, was accurately described by the analytical expressions presented in this dissertation. Thus, this study provides insight into and a description of the factors that influence and control battery behavior during pulsed cycling. The quantitative description of the voltage change with time during the pulse and relaxation provides a convenient and powerful tool for predicting cell voltage for WS duty cycle pulse operation. It serves as a basis for understanding and optimizing battery performance for sensor duty cycles.

Systematic experimental studies were carried out under various pulse cycling conditions. The pulse cycling tests were designed so that the impact of each operating parameter (i.e. peak current I_p, standby current I_s, pulse length t_p, standby period t_s) was evaluated. Due to the small magnitude of the standby current, the influence of the standby current on the operating voltage and battery capacity was negligible, and thus the voltage analysis for relaxation at zero current can be used for relaxation at low currents ($\leq$50μA) without introducing significant error. The pulse current had a significant impact on the lower voltage and determined the maximum capacity that could possibly be extracted from a battery affected by the duty cycle factor. For each pulse length studied, the battery capacity increased as the standby time increased, until a maximum capacity was reached and further increase in the standby time did not increase the battery capacity any further. When pulse length increased, the minimum standby time needed for full (or near full) relaxation increased. The minimum standby time for full relaxation was found to correlate with ratio t_s/t_p^2. This is one of the key results of the study, which can be used to determine the highest duty cycle of WS operation to achieve the maximum capacity of a battery under certain pulse/standby currents.

In situations of incomplete relaxation, the upper voltage was the result of both a "background" concentration gradient and the relaxation of the concentration gradient caused by the pulse discharge right before a standby period. The "background" concentration gradient was associated with the average mass transfer rate of the lithium ion, which can be expressed by the time average current. At the same average current, the total capacities obtained for shorter pulses were higher than those of longer pulses. These results and the procedure illustrated thereby can be used to predict the battery capacity during sustained pulse discharge cycling for a broad range of duty cycle parameters in order to optimize the WS system. The procedures and considerations in selecting the operating parameters of WS (I_p, I_s, t_p, t_s) are summarized in Chapter 5.

An important aspect of the rechargeable lithium cells chosen for use in this study is their potential to be coupled with a power harvesting device to extend the operating lifetime of WSs by extracting ambient energy to charge the battery. Battery pulse discharge-recharge cycling as would occur in a hybrid power system was investigated, and the recharge strategies were evaluated in terms of capacity loss over cycling and energy efficiency. Results from the initial cycling tests suggested the importance of a rest period between the discharge and charge step of a cycle. PRCR cycling with 2s rest period could lower the capacity loss to 25% or less of that of PC cycling with no rest period over 10,000 cycles. Cycling the battery at 80% SOC rather than at 100% SOC (3.1 V) significantly reduced the capacity loss during cycling.

There are several opportunities for continued and future work related to this study.

1. The transient analysis and testing procedures developed in this study can be used for other energy type lithium cells where a non-uniform reaction distribution is expected as well. Primary lithium coin cells (e.g. CR and BR cells) that start to find applications in existing WS systems should benefit from this work directly with minor modifications.

2. Further investigation could include other existing coin cells that may be of great interest for WS applications. For example, zinc-air batteries, which are not suitable for continuous galvanostatic discharge at high rates due to the oxygen transport limitations, may be able to handle pulse currents much higher than the limiting current, and offer up to twice the energy density of lithium coin cells.
3. In a broader sense, a battery data base of commercial coin cells that includes the information of their pulse power capability and performance characteristic under sensor duty cycles would be very useful to WS system design engineers for cell selection. It would enable power solutions under specified constraints (e.g. power, volume) and bring more accurate results in terms of factors important to microsystems such as weight, size, power consumption, operating life, etc.
4. In this study, battery life optimization was studied for a single battery relevant to an individual sensor node. Energy efficiency optimization for an entire WS network may be quite different. The optimization of WS networks is an area that has received much attention recently and is in need of contributions from battery experts as well. For example, on a node level, a lower pulse current is favored in maximizing battery life. However, selection of pulse current is central to the trade-off between transmission power level and transmission range. A lower peak power and resulting shorter transmission range would likely require the use of more intermediate nodes in the network and may not be optimal with respect to the overall network energy consumption.
5. Initial experimental investigation on recharge showed some very interesting trade-offs between the recharge current, recharge time and battery state-of-charge (SOC). More extensive studies are needed to identify the most effective and efficient recharge strategy,

and to provide a fundamental understanding of the mechanism responsible for capacity loss during pulse cycling.

REFERENCES

1. S. C. Mukho K.M. Sivalingam and T.F. Znati, padhyay and H. Leung, Advances in wireless sensors and sensor networks, Springer-Verlag, Berlin, Heidelberg, (2010).

2. B. Warneke, M. Last, B. Liebowitz, K.S.J. Pister, Smart dust: communicating with a cubic-millimeter computer, Computer, 34 (2001) 44-51.

3. K.M. Sivalingam and T.F. Znati,Wireless sensor networks, Kluwer Academic, Hingham, (2004).

4. http://en.wikipedia.org/wiki/Wireless_sensor_network, retrieved February 11, 2011.

5. http://fiji.eecs.harvard.edu/Mercury: Mercury: A Wearable Sensor Network Platform for High-Fidelity Motion Analysis, retrieved February 1, 2011.

6. D. Diamond, S. Coyle, S. Scarmagnani, J. Hayes, Chem. Rev. 108 (2008) 652-679.

7. http://www.hpl.hp.com/research/intelligent_infrastructure/, CeNSE: Central nervous system of the earth, retrieved February 1, 2012.

8. Crossbow Technology Inc., MICAz wireless measurement system, http://www.xbow.com, June 2004.

9. J. Polastre, R. Szewczyk, D. Culler, Fourth International Symposium on IPSN, 2005, 364-369.

10. http://particle.teco.edu/upart/: uPart014x ilmt datasheet, retrieved February 1, 2012.

11. http://www.eecs.harvard.edu/~konrad/projects/shimmer/references/tmote-sky-datasheet.pdf, retrieved April 10, 2011.

12. V. Shnayder, M. Hempstead, B. Chen, G.W. Allen, M. Welsh, SenSys '04 Proceedings of the 2nd International Conference on Embedded Networked Sensor Systems, 2004, 188-200.

13. D. Tse and P. Viswanath, Fundamentals of Wireless Communication, Cambridge University Press, (2005).

14. http://www.physorg.com/news/2012-02-low-power-multi-standard-transceiver-sensor-networks.html, retrieved March 1, 2011.

15. C.F. Chiasserini, R.R. Rao, Proc. of Mobicom’99, Seattle, 1999, 88-95

16. R. Szewczyk, J. Polastre, A. Mainwaring, and D. Culler, Lessons From a Sensor Network Expedition, in European Workshop on Wireless Sensor Networks, Jan. 2004.

17. C. Park, K. Lahiri, A. Raghunathan, IEEE SECON 2005 Proceedings 430-440.

18. D. Linden, T.B. Reddy, Handbook of Batteries, third ed., McGraw-Hill, New York, 2001.

19. K. Lahiri, A. Raghunathan, S. Dey, and D. Panigrahi, Battery Drive System Design: A New Frontier in Low Power Design, in Proc. ASPDAC/Int. Conf. VLSI Design, 2002, 261–267.

20. R. Rao, S. Vrudhula, and D. Rakhmatov, Battery Models for Energy Aware System Design, IEEE Computer, 36 (2003) 1019–1030.

21. M. Doyle, T. F. Fuller, and J. S. Newman, Modeling of Galvanostatic Charge and Discharge of Lithium/Polymer/Insertion cell, J. Electrochem. Soc, 140 (1993) 1526–1533.

22. C. Chau, F. Qin, S. Sayed, M.H. Wahab, Y. Yang, IEEE Journal on Selected Areas in Communications 28 (2010) 1222-1232.

23. T. K. Dong, A. Kirchev, F. Mattera, J. Kowal, and Y. Bultel, Dynamic Modeling of Li-Ion Batteries Using an Equivalent Electrical Circuit, J. Electrochem. Soc., 158 (2011) A326-A336.

24. K.E. Thomas, R.M. Darling, J. Newman, Mathematical modeling of lithium batteries, Kluwer Academic/Plenum Publishers 2002.

25. http://www.panasonic.com/industrial/batteries-oem/oem/primary-coin-cylindrical/br-cr.aspx, retrieved February 1, 2012.

26. http://www.panasonic.com/industrial/batteries-oem/oem/rechargeable-coin/index.aspx, retrieved February 1, 2012.

27. http://en.wikipedia.org/wiki/Button_cell, retrieved February 1, 2012.

28. www.digikey.com, Coin cell price comparison, retrieved February 1, 2012.

29. J.W. Long, B. Dunn, D.R. Rolison, H.S. White, Three-dimensional battery architectures, Chemical Reviews, 104 (2004) 4463-4492.

30. http://www.microbattery.com/tech-maxell-lithium.htm, retrieved February 11, 2012.

31. J. Newman, K.E. Thomas-Alyea, Electrochemical Systems, Third ed., Wiley, Hoboken, 2004.

32. A. Jossen, Fundamentals of battery dymanics, J. Power Sources, 154 (2006) 530-538.

33. E. Barsoukov, J.R. Macdonald, Impedance spectroscopy, theory, experiment, and applications, Second ed., Wiley, 2005.

34. M. Doyle, J. Newman, Analysis of capacity-rate data for lithium batteries using simplified models of the discharge process, J. Applied Electrochemistry, 27 (1997) 846-856.

35. T. Fuller, M. Doyle, and J. Newman, Relaxation phenomena in lithium-ion-insertion cells, J. Electrochem. Soc., 141 (1994) 982-990.

36. M. Kanda, S. Yamada, T. Shirogami, Y. Sato and T. Takamura, Solid state Li/MnO_2 cells, J. Applied Electrochemistry, 12 (1982) 599-606.

37. T. Ohzuku, M. Kitagawa, and T. Hirai, Electrochemistry of manganese dioxide in lithium nonaqueous cell III. X-Ray Diffractional study on the reduction of spinel-related manganese dioxide, J. Electrochem. Soc., 137 (1990) 769-775.

38. T. Ohzuku, M. Kitagawa, and T. Hirai, Electrochemistry of manganese dioxide in lithium nonaqueous cell II. X-Ray diffractional and electrochemical characterization on deep discharge products of electrolytic manganese dioxide, J. Electrochem. Soc., 137 (1990) 40-46.

39. T. Nohma, T. Saito and N. Furukawa, Manganese oxides for a lithium secondary battery-composite dimensional manganese oxide (CDMO), J. Power Sources, 26 (1989) 389-396.

40. T. Nohma, Y. Yamamoto, K. Nishio, I. Nakane, and N. Furukawa, Lithium-containing manganese dioxide (composite dimensional manganese oxide: CDMO) as positive material for a lithium secondary battery, J. Power Sources, 32 (1990) 373-379.

41. T. Nohma, S. Yoshimura, K. Nishio, Y. Yamamoto, S. Fukuoka, M. Hara, S. Fukuoka, M. Hara, Development of coin-type lithium secondary batteries containing manganese dioxide/Li-Al, J. Power Sources, 58(1996) 205-207.

42. H. Watanabe, T. Nohma, I. Nakane, S. Yoshimura, K. Nishio, T. Saito, J. Power Sources 43-44 (1993) 217-221.

43. Specifications of Manganese Rechargeable Lithium Batteries: http://biz.maxell.com/products/industrial/battery/ml/index.html, retrieved March 10, 2012.

44. J.N. Harb, R.M. LaFollette, R.H. Selfridge, L.L. Howell, J. Power Sources 104 (2002) 46-51.

45. B.H. Calhoun, D.C. Daly, N.Verma, D.F. Finchelstein, D.D. Wentzloff, A. Wang, S. Cho, A.P. Chandrakasan, IEEE Transactions on Computers 54 (2005) 727-740.

46. S. Prakash, W.E. Mustain, P. Kohl, J. Power Sources, 189 (2009) 1184-1189.

47. K.A. Cook, A.M. Sastry, An algorithm for selection and design of hybrid power supplies for MEMS with a case study of a micro-gas chromatograph system, J. Power Sources, 140 (2005) 181-202.

48. K.A. Cook, F.Albano, P.E. Nevius, A.M. Sastry, POWER (power optimization for wireless energy requirements): A MATLAB based algorithm for design of hybrid energy systems, J. Power Sources, 159 (2006) 758-780.

49. J. Li, E. Murphy, J. Winnick, P.A. Kohl, J. Power Sources, 102 (2001) 294-301.

50. J. Li, E. Murphy, J. Winnick, P.A. Kohl, J. Power Sources, 102 (2001) 302-309.

51. www.intelligent-charging.com, retrieved April 21, 2012.

52. D. Belov & Mo-Hua Yang, Failure mechanism of Li-ion battery at overcharge conditions, J. Solid State Electrochem 12 (2008) 885–894.

53. S.H. Choia, J. Kima, Y.S. Yoon, Self-discharge analysis of LiCoO2 for lithium batteries, J. Power Sources 138 (2004) 283–287.

54. J.P. Christophersen, G.L. Hunt, C.D. Hoa, D. Howell, J. Power Sources 173 (2007) 998–1005.

55. G.Sarre, P. Blanchard, M. Broussely, J. Power Sources 127 (2004) 65–71.

56. I. Ong and J. Newman, J. Electrochem. Soc., 146 (1999) 4360-4365.

57. FreedomCAR BatteryTest Manual for Power-Assist Hybrid Electric Vehicles, DOE/ID-11069, Oct. 2003.

58. K. Smith, C.Wang, J. Power Sources 161 (2006) 628–639.

59. D. Bernardi, J. Go, J. Power Sources 196 (2011) 412–427.

60. T.F. Fuller, M. Doyle, J. Newman, J. Electrochem. Soc., 141 (1994) 1-10.

61. K.A. Cook, F. Albano, P.E. Nevius, A.M. Sastry, J. Power Sources, 159 (2006) 758-780.

62. K.A. Cook, A.M. Sastry, J. Power Sources, 140 (2005), 181-202.

63. D.E. Stephenson, S.C. Harris, N.A. Zacharias, D.J. Rowenhorst, D.R. Wheeler, Microstructure and transport properties of porous Li-ion electrodes, paper manuscript.

64. K.D. Wise, Sensors and Actuators A: Physical 136 (2007) 39–50.

65. A.J. Bard, L.R. Faulkner, Electrochemical Methods Fundamentals and Applications, Second ed., Wiley, Hamilton, 2001.

66. D. Dees, E. Gunen, D. Abraham, A. Jansen, J. Prakash, J. Electrochem. Soc. 152(2005) A1409-A1417.

67. W. Weppner, R.A. Huggins, J. Electrochem. Soc. 124 (1977) 1569-1578.

68. C.J. Wen, B.A. Boukamp, R.A. Huggins, J. Electrochem. Soc. 126 (1979) 2258-2266.

69. R.A. Moshtev, P. Zlatilova, B. Puresheva, V. Manev, A. Kozawa, J. Power Sources, 51 (1994) 409-423.

70. C.M. Julien a, B. Banov b, A. Momchilov b, K. Zaghib, J. Power Sources 159 (2006) 1365–1369.

71. H.J. Bang, S. Kim, J. Prakash, J. Power Sources 92 (2001) 45-49.

72. L. Valøena, J.N. Reimersa, J. Electrochem. Soc. 152 (2005) A882–A891.

73. C-W. Wang, A.M. Sastry, K.A. Striebel, and K. Zaghib, J. Electrochem. Soc.152 (2005) A1001-A1010.

74. T. Ohzuku, M. Kitagawa, T. Hirai, J. Electrochem. Soc. 137 (1990) 769-775.

75. R. Pollard, J. Newman, Electrochimica Acta 25 (1980) 315-321.

76. http://www.inframat.com/products/32B-0825.htm, retrieved February 21, 2012.

77. S. Basu, W.L. Worrell, Fast Ion Transport in Solids, Elsevier, Amsterdam (1979) 149-152.

78. J. Vetter, P. Nov´ak, M.R. Wagner, C. Veit, K.-C. M¨oller, et al. J. Power Sources 147 (2005) 269–281.

79. S.H. Choi, J. Kim, Y.S. Yoon, J. Power Sources 138 (2004) 283–287.